Faculty of Sciences

Department of Physics and Astronomy

Slow Sodium Inactivation and Scale-Invariant Excitability

by

Willem Wybo

Supervisors: Prof. Dr. Giugliano, Dr. Linaro, Prof. Dr. Ryckebusch

A dissertation presented in partial fulfilment of the requirements for the degree of Master in Physics and Astronomy

Year 2011–2012

Abstract

In neuroscience, a vast body of worked is aimed at crafting single neuron models, that reproduce the firing characteristics of neurons in vivo. Recently, there has been much interest in understanding the behaviour of these single neurons over long times scales, from hours to days.

Experiments have shown that, on such time scales, nerve cells exhibit dynamics that are not captured in any neuron model to date. In particular, the neuronal excitability exhibits scale-invariant statistics. In this work we propose a neuron model that exhibits this behaviour, by augmenting the canonical sodium channel scheme with a linear chain of degenerative, inactive states and by assuming that the number of ion channels in the nerve membrane fluctuates about its equilibrium value in a random manner. We show that this model indeed reproduces the observed excitability characteristics in a robust way, agreeing qualitatively with the experimental results.

Acknowledgements

Numerous are the people without which this thesis work would not be what it is today. First and foremost, I would like to thank Dr. Daniele Linaro, who was never short on information and was always keen to provide help and assistance with my abundant problems with regards to computers, simulations and data processing. Thanks to his meticulous proofreading, the quality of this text and my scientific English improved greatly. I would also like to thank prof. Michele Giugliano, who was always keen to advance my knowledge of neuroscience and who provided excellent guidance and many insightful discussions. The other members of the laboratory of theoretical neurobiology and neuroengineering also deserve my gratitude: Mike Wijnants, who provided abundant help when there were computer-related problems, Joao Couto, who never hesitated to answer my questions, and the others: Pascal Warnaar, Istvan Biro, Rocco Barone and Antonina Monaco, who provided a stimulating and exciting scientific environment to work in.

None of this work would have been possible without the continuous support of my family. They supported me throughout my studies and always provided me with the freedom to pursue my ideas and goals, no matter how crazy they may have seemed at first. They provided exactly the stable environment one needs to fully develop oneself and ultimately to succeed at his studies.

Furthermore I would like to thank prof. Jan Ryckebusch for his willingness to supervise this thesis work and for never hesitating to answer my questions. Finally I would like to thank my fellow physics students, with whom I passed five beautiful and interesting years.

Willem Wybo, June 2012.

Contents

Chapter 1

Introduction

In recent years, the field of computational neuroscience has grown tremendously through advances in technology and computer power, drawing in scientists from fields as diverse as physics, engineering and computer sciences [1]. The reasons for this influx are abundant: a fresh and dynamical field, where mathematical insight is paired up with intuition, that deals with topics such as information processing, learning and memory in networks of neurons. Such networks occur in all animals, ranging from very simple - the nematode worm Caenorhabditis Elegans has only 302 neurons [2], making it an ideal test subject - to very complex - the human brain is estimated to contain around 10^{11} neurons [3]. The ultimate goal, to understand how our brains learn, love, store memories, develop creative ideas and become conscious, may be quite ambitious given the staggering numbers, but is nevertheless enthralling and the road to its answer has been paved with interesting and useful discoveries. No wonder then, that so many young researchers are fascinated by this field and are drawn to it.

Thus the scene has been set, and herds of young scientists are ready and eager to translate networks of neurons into bits and bytes, throw in connectivity and learning rules and see which information they can code. Nevertheless, they need one more thing, as all their efforts are bound to fail without it: accurate neuron models. Developing such single-neuron models has been a vital part of neuroscience ever since Louis Lapicque proposed the first integrate and fire model [4], and is also the subject of this thesis work. In single-neuron modelling, the goal is often two-fold: at a fundamental level one wants to understand the biophysical processes that govern and change the behaviour of neurons, from time-scales of milliseconds up to a full lifetime - although even today this remains a mere dream, and, at a more applied level, to develop simplified, effective models that contain only a few variables that can account for the key properties of the nerve cell's dynamics, so that they

can be used efficiently in large-scale networks and so that one can determine which of the many neuronal properties really matter for information processing.

In general, scientists try to conceive mathematical models that aim to explain a range as wide as possible of experimentally observed phenomena, starting from principles that are as simple as possible. However, a model, is only good as long as it describes experimentally observed data, and that is precisely where a fundamental problem of neuroscience lies. Neuron models are often simplified mathematical abstractions, whereas nerve cells are tremendously complex objects, regulated and influenced by processes on time scales far beyond what is experimentally observable. Recently however, the boundary of what is possible has been pushed forward, as technologies have been developed that make it possible to extend the duration of experiments that record the activity of single neurons from time-scales of hours to time-scales of days. Such long-term recordings have been performed [6] and the dynamics they revealed were very rich and complex, and not at all captured by any previously developed neuron model. It is the subject of this thesis work to try and capture at least a good part of these dynamics in a neuron model, in such a way that it is possible to ask clear and well-defined biophysical questions about its causes.

To come to these questions, some fundamental concepts in neuronal modelling have to be discussed. This is the subject of the second chapter, where we will explain how neurons can be modelled by relatively simple models. We will define what we mean by neuronal excitability, and discuss the causes of this excitability. We also motivate our choice of models, which follows the framework introduced by Hodgkin and Huxley in their canonical paper [5]. We choose this framework because it is relatively simple and allows us to ask biophysically precise and well-defined questions about the causes of the complex dynamics described in [6].

In the third chapter, we will review results from [6] that are relevant for this work. We will give a brief introduction to the experimental set-up and protocol, and discuss the relevance of this protocol. It turned out that some relatively advanced statistical measures were needed to perform a full analysis of the data, so in this chapter we will also explain these measures.

The goal of the fourth chapter is to come to a deterministic neuron model that explains as many aspects of the dynamics reported in [6] as possible. We will start by showing that canonical neuron models don't describe these dynamics at all, which will motivate us to propose a model that implements a slow sodium inactivation. We also analyse and test this model thoroughly and compare the results against the experimental data.

Since neurons are inherently stochastic, and a great part of the observed dynamics results almost certainly from stochastic effects, we introduce the stochasticity of neurons in

the fifth chapter. Such stochasticity can come in many forms. Traditionally, neurons are modelled using Markov chains [7] and it is generally assumed that neuronal stochasticity results from this Markov noise. Thus we discuss algorithms to model such noise and motivate why we use them or why we don't. Nevertheless, whether such Markov noise is really present in neurons has been debated, and this noise may not contribute enough or may not have the right properties to explain the observed stochastic dynamics. Therefore we hypothesize that another form of noise may exist, with fundamentally different properties than the Markov noise. We explain these properties, motivate why it might be necessary to introduce such a form of noise and test this hypothesis thoroughly on different variations of our model.

Chapter 2

Conductance based neuron models

2.1 Nerve cells and action potentials

The interesting properties of neuronal systems arise through differences in ion concentrations between the inside and the outside of nerve cells. Most of the time, the ion concentrations are distributed so that the membrane potential, defined as the difference between the potential in the intracellular and the extracellular medium, is negative. For example, in pyramidal neurons of the mammalian cortex, it fluctuates around -65 mV. This is a dynamic equilibrium, kept in place by ion channels and ion pumps that selectively let ions pass through the nerve membrane. Ion pumps generally keep the ion concentrations steady, so that this equilibrium potential is maintained. If this was not the case, intracellular and extracellular potentials would eventually level out. However, these ion pumps do not contribute to the short time-scale properties of the neurons and hence they are seldom considered in neuronal modelling. Usually it is assumed implicitly that they keep the ion concentrations constant.

The ion channels are of far greater interest to the modeller. This is not at all obvious at first: they open and close in a seemingly random manner and passively let ions flow through when they are open, thus generating an ion flow that depends only on the concentration and on the potential gradients. They are interesting because of two key features they possess: first, they are very selective, which means that they allow only a single type of ions to flow through and secondly, the rates at which they open and close depend in a highly non-linear manner on the membrane potential.

These two key properties give rise to one of the fastest biological processes ever recorded, the action potential or spike. This process occurs when the electrical inputs a neuron receives increase its membrane potential to a sufficiently high value (generally -50 to -30

mV). Through the changes in the opening and closing rates of the ion channels, induced by their voltage dependence, a self-reinforcing process emerges that drives the membrane potential to rise very rapidly to a positive value (10 to 60 mV) and then to drop equally fast back to its resting potential.

Neurons use action potentials to communicate: hence, understanding the emergent behaviour of neural networks is impossible without understanding how and when these action potentials are generated. Because of this reason, a significant amount of research in neuroscience is aimed at replicating the neuronal firing characteristics in computer models.

Such models come in a wide variety of shapes and forms, ranging from models that are closely related to the actual biophysical picture, containing thousands of equations that explicitly model chains of chemical reactions, to very simplified models that retain only one or a few aspects of neuronal dynamics. To motivate our choice of models we first provide a brief discussion of the morphology of neurons.

2.2 Neuronal morphology

Nerve cells come in a wide variety of shapes and forms, adapted to their specific task, and while there are many variations and exceptions occur rather often, three main structures can be identified in general: the dendrites, the soma and the axon. The dendrites branch many times and form a very rich three-like structure that originates from the soma. This structure allows the nerve cells to receive inputs from the axons of many other neurons through synaptic connections, that can be as numerous as 100000 for some types of neurons, such as cerebellar Purkinje cells. These inputs then propagate through the dendrites and eventually arrive at the soma, the cell body, where they are processed and integrated. If enough of these inputs arrive in a given time-interval, so that the membrane potential is excited above the firing threshold, an action potential is likely to be produced. The axon then serves to transmit these action potentials to those neurons that have dendrites with synaptic connections to that axon. Numbers are staggering again, as on average there are 180 synaptic connections per mm to an axon and a single axon can reach lengths of 40 mm.

Action potentials as the ones we described, that are generated in the soma and propagate away from it through the axon, are called orthodromic spikes. In some situations however, particularly in experiments, action potentials are generated through some form of stimulation in the axon, and then propagate towards the soma. Such spikes are called antidromic action potentials.

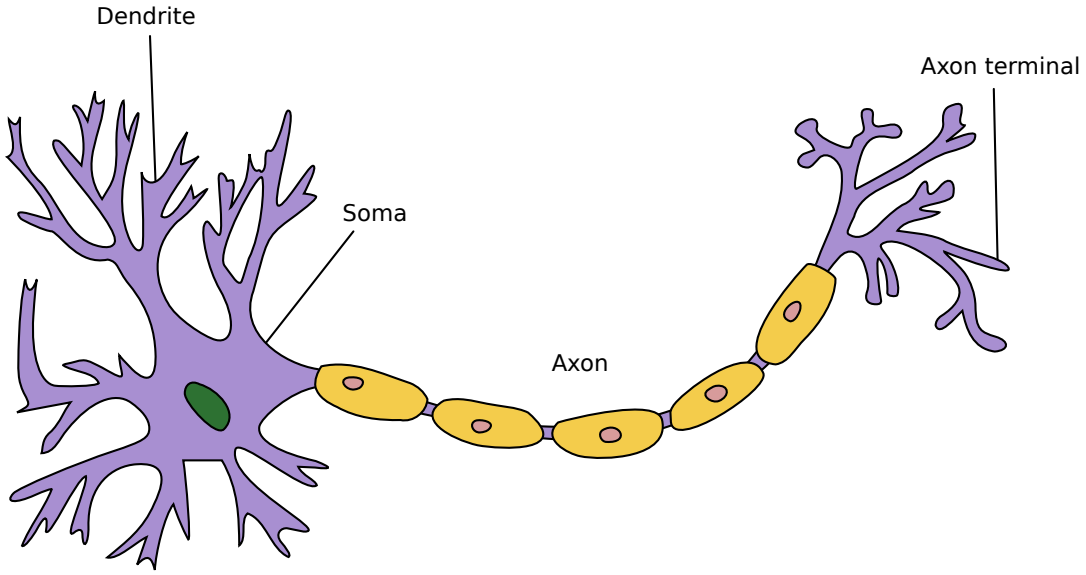

Figure 2.1: The structure of a typical neuron.

In both cases, the spikes are generated in a localized region of the neuron, either in the soma or in a specific part of the axon. Often, it is not unreasonable to assume that the membrane potential in such a localized region is uniform, so that spatial fluctuations can be discarded and that the potential can be described by a single variable V. Such models are called single-compartment models and we shall use them throughout the rest of this work, since this is a reasonable assumption in the experimental protocol we will discuss in the next chapter.

2.3 Trans-membrane currents

Ions flowing through ion channels result in a net trans-membrane current: at the single channel level, these currents are most often approximated by Ohm's law, as linear functions of the voltage. Non-linearities arise because the number of conducting channels changes in a non-linear way as a function of the voltage. If V denotes the membrane potential, the current I_i that arises through the flow of a type of ions through a specific type i of channels becomes

$$I_i = g_i(V)(V - E_i). \tag{2.1}$$

In this form the parameters E_i and g_i have a clear physical interpretation. E_i denotes the reversal potential for this type of ion channel: at this potential, inward and outward ionic flows are exactly balanced, and the net current is zero. Above this potential the ionic current is drawing the voltage down and below it the current is drawing the voltage up (whether the current is then inward or outward depends on the sign of the ionic charge). g_i denotes the total conductance of the population of ion channels being considered. It is proportional to the mean conductance of a single channel and to the amount of channels that are open and thus conducting. The single channel conductance is usually assumed to be fixed, whereas the number of open channels depends on the voltage.

2.3.1 Reversal potential

The reversal potential for a certain type of ion channels is the potential at which the net trans-membrane current through these channels becomes zero. Since ionic flows are dependent on both the membrane potential and the concentration gradients, the reversal potential will follow from an equation involving both, that can be derived using a simple thermodynamic argument.

Suppose the membrane potential V is negative: positive ions with charge q exiting the cell will have to overcome a potential barrier of height $-qV$. The amount of ions that can overcome this barrier is proportional to the integral of the Boltzmann distribution for values greater then $-qV$, and thus to $\exp(qV/kT)$. The flow of ions out of the cell is then proportional to this factor and the ion concentration inside c_{in}. Ions that enter the cell don't feel such a potential barrier, and hence the inward current is proportional only to the concentration outside the cell c_{out}. At the reversal potential $V = E$, these flows are exactly balanced, thus leading to the condition

$$c_{out} = c_{in} \exp(qE/kT). \tag{2.2}$$

Rewriting this leads to the Nernst equation

$$E = \frac{kT}{q} \ln\left(\frac{c_{out}}{c_{in}}\right). \tag{2.3}$$

Redoing this derivation for all possible combinations of signs of the membrane potential and the ion's charge leads to exactly the same result. Since the ion concentrations inside and outside the cell can be measured, these reversal potentials can be calculated. The most common types of ions used in conductance based models, sodium (Na^+) and potassium (K^+), have reversal potentials E_{Na} and E_K of more or less 55 mV and -75 mV respectively.

Knowing this, it can be anticipated that sodium currents will be responsible for the rapid rise in the membrane potential during the spike and potassium currents for the rapid drop.

2.3.2 Conductances and gating functions

The conductance g_i of a population of ion channels is formally just the factor of proportionality between the voltage and the trans-membrane current. Through a simple reasoning however, a relation can be established between this conductance and the physical variables that determine it. Suppose that for an open ion channel, a mean single channel conductance γ_i can be defined. If there are N_i^{open} channels in the open or conducting state, the conductance g_i is given by $\gamma_i N_i^{open}$. Generally it is more convenient to think in fractions of open channels. Calling this fraction $o_i = N_i^{open}/N_i$, where N_i is the total number of channels of the population, the conductance becomes

$$g_i = \overline{g}_i o_i \tag{2.4}$$

where $\overline{g}_i = \gamma_i N_i$ denotes the maximal conductance of the population of ion channels.

The fraction o_i of channels that are conducting is the variable that induces non-linear effects as the action potential. It is generally assumed that channels open and close because of chains of chemical reactions, whose rates depend non-linearly on the voltage. The simplest of such chains consists of two states, the said open state and a single closed state c_i, with a voltage-dependent rate $\alpha_i(V)$ to go from closed to open and a voltage-dependent rate $\beta_i(V)$ to go from open to closed, as in figure 2.2A. Figures 2.2B and 2.2C contain pictures of more complicated schemes.

Channels flicker randomly between these two states, and hence the neuronal system is inherently stochastic. How to model neurons in such a probabilistic way is the subject of chapter 5. For the moment we assume that there are enough ion channels, so that the evolution of the fraction o_i can be modelled by the evolution of its mean in a deterministic way. In such a framework, the fraction of channels that will go from c_i to o_i in a small time-interval $\mathrm{d}t$ is given by $\alpha_i(V)\mathrm{d}t\ c_i(t)$. The fraction of channels that will stay in o_i during this time-interval is given by $(1 - \beta_i \mathrm{d}t)\ o_i(t)$. The fraction of open channels at the time $t + \mathrm{d}t$ is then given by

$$o_i(t + \mathrm{d}t) = (1 - \beta_i \mathrm{d}t)\ o_i(t) + \alpha_i(V)\mathrm{d}t\ c_i(t). \tag{2.5}$$

Hence, the evolution of o_i is governed by the following linear equation:

$$\frac{\mathrm{d}o_i}{\mathrm{d}t} = -\beta_i(V)o_i(t) + \alpha_i(V)c_i(t). \tag{2.6}$$

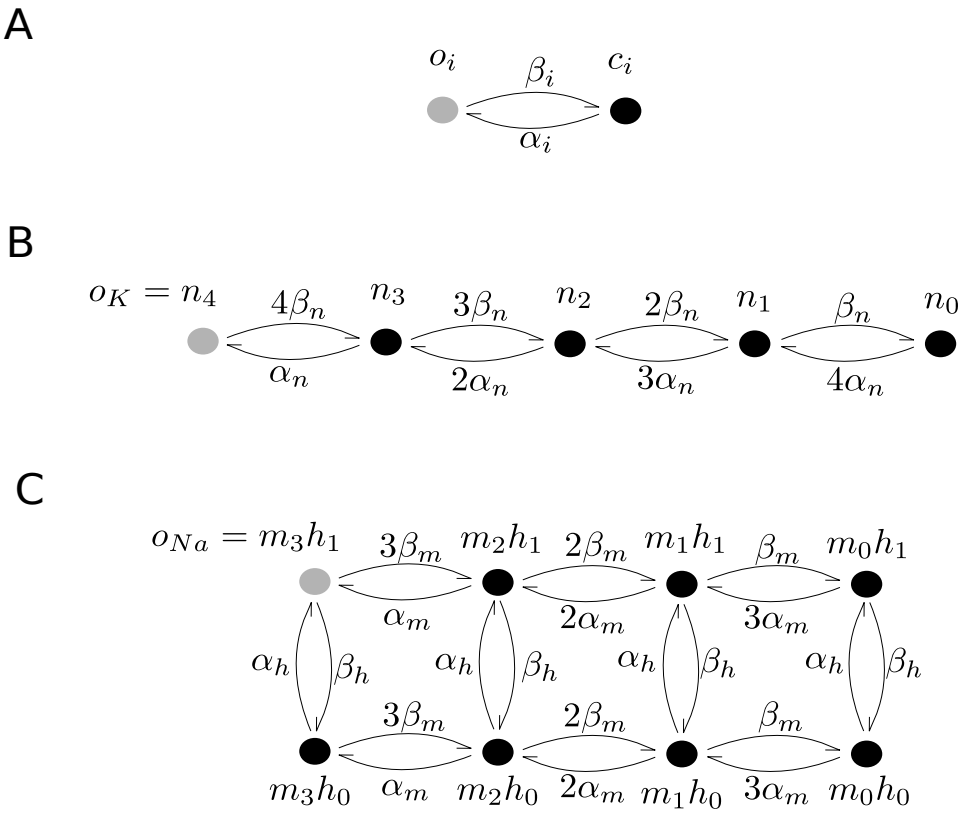

Figure 2.2: (**A**) The simplest possible kinetic scheme, consisting of one open and one closed state. (**B**) A more complicated kinetic scheme, commonly in use to model potassium currents. (**C**) A scheme that is commonly used to model sodium currents.

For the evolution of c_i, an analogous equation can be derived, leading to the linear system

$$\frac{\mathrm{d}}{\mathrm{d}t}\begin{pmatrix} o_i(t) \\ c_i(t) \end{pmatrix} = \begin{pmatrix} -\beta_i(V) & \alpha_i(V) \\ \beta_i(V) & -\alpha_i(V) \end{pmatrix}\begin{pmatrix} o_i(t) \\ c_i(t) \end{pmatrix}. \tag{2.7}$$

This system is redundant, as the colums of the transition matrix sum to zero. This is a general result when doing mean-field theory in kinetic schemes and it expresses the conservation of probability. Substituting $c_i = 1 - o_i$, it is clear that the system is also fully described by the following equation:

$$\frac{\mathrm{d}o_i}{\mathrm{d}t} = -\beta_i(V)o_i(t) + \alpha_i(V)(1 - o_i(t)). \tag{2.8}$$

Such an equation can be rewritten in a more intuitive form

$$\frac{\mathrm{d}o_i}{\mathrm{d}t} = \frac{1}{\tau_i}(o_i(t) - o_{\infty i}(V)), \tag{2.9}$$

where

$$\tau_i(V) = \frac{1}{\alpha_i(V) + \beta_i(V)} \tag{2.10}$$

$$o_{\infty i}(V) = \frac{\alpha_i(V)}{\alpha_i(V) + \beta_i(V)}. \tag{2.11}$$

In this form, the equation for o_i has a simple meaning: $o_{\infty i}(V)$ is the steady-state value of o_i and $\tau_i(V)$ is the characteristic time constant with which o_i evolves. In other words, fast variables (small $\tau_i(V)$) follow their asymptotic value closely, whereas slow variables (large $\tau_i(V)$) lag behind. Sometimes the kinetics are specified through the rates α and β and sometimes through the asymptotic variable and the relaxation times.

For the more complicated schemes, mean field expressions as (2.7) can also be derived. Suppose a scheme contains N states $\mathbf{x} = (x_1, \ldots, x_N)$. For the scheme in figure 2.2B we have $\mathbf{x} = (n_4, n_3, \ldots, n_0)$ and for figure 2.2C $\mathbf{x} = (m_3h_1, m_3h_0, \ldots, m_0h_0)$. The mean field approximation explained above for the two-state scheme now yields a transition matrix $\mathbb{W}$, leading to the linear system of equations

$$\frac{\mathrm{d}\mathbf{x}}{\mathrm{d}t} = \mathbb{W}\mathbf{x}. \tag{2.12}$$

Again, this matrix is redundant as the columns sum to zero, and one of the equations can be eliminated.

Kinetic schemes 2.2B and 2.2C have very particular forms and their states have very particular names. This is because these schemes can be mapped onto combination of multiple two-state schemes. The scheme in figure 2.2B, for instance, maps onto a model where all channel are assumed to consists of four identical subunits, that all have the same two-state scheme given by equation (2.8), and that the channel is only conducting or open if all four subunits are open. If we denote the fraction of open subunits as measured over all channels as n (the fraction of closed subunits is $1 - n$), then the fraction of open channels $o = n_4$ is given by n^4. It can be checked that the fraction of channels in the state n_3 of the kinetic scheme is then given by $n^3(1-n)$, the fraction of channels in state $n_2 = n^2(1-n)^2$, $n_1 = n(1-n)^3$ and $n_0 = (1-n)^4$. In the mean-field approximation, the dynamics given by equation (2.12) and by the equation

$$\frac{\mathrm{d}n}{\mathrm{d}t} = -\beta_n(V)n(t) + \alpha_n(V)(1 - n(t)) \tag{2.13}$$

are then strictly equivalent if the above mapping is applied. An analogous mapping can be achieved for scheme 2.2C, but now $o = m^3h$, where m and h are two different variables both following a different two-state mean-field equation.

$$\frac{\mathrm{d}m}{\mathrm{d}t} = -\beta_m(V)m(t) + \alpha_m(V)(1 - m(t)) \tag{2.14}$$

$$\frac{\mathrm{d}h}{\mathrm{d}t} = -\beta_h(V)h(t) + \alpha_h(V)(1 - h(t)) \tag{2.15}$$

This subunit picture was how the variations in the number of conducting channels were originally modelled. However, many kinetic schemes have been proposed that are impossible to map onto a subunit picture [9], [10]. Nevertheless these subunit interpretations provide convenient insight in how the action potential is generated, as it is easy to analyse the resulting differential equations. Such analysis is done in every textbook on neural modelling (see for instance [3]) and we will not repeat it here, as we are not interested in the specific subunit dynamics generating the spike.

2.4 Charge-balance equation

Since the cell membrane is mostly impermeable to charged ions, it acts as a capacitor, around which charge can build up. The ion channels in the nerve-membrane form a huge array of parallel conductors, as in figure 2.3. The rate of change of the membrane potential is simply given by the known relation from electronic circuits:

$$C_m\frac{\mathrm{d}V}{\mathrm{d}t} + \sum_i I_i = I_{\mathrm{ext}} \tag{2.16}$$

where the sum runs over all trans-membrane currents. Often, it is convenient to separate the trans-membrane currents due to ion channels explicitly from other currents, such as synaptic inputs or currents injected by the experimenter (I_{ext}). Substituting equation 2.1 in equation (2.16) yields

$$C_m\frac{\mathrm{d}V}{\mathrm{d}t} + \sum_i g_i A(V - E_i) = I_{\mathrm{ext}}. \tag{2.17}$$

Usually the capacitance per unit area is taken ($c_m = C_m/A$), and equation (2.17) scales with the cell's surface as

$$c_m\frac{\mathrm{d}V}{\mathrm{d}t} + \sum_i g_i(V - E_i) = I_{\mathrm{ext}}/A \tag{2.18}$$

Virtually all neural models have this equation in common: they differ in how the trans-membrane currents are modelled. In the following we discuss two particular examples of such models that will be relevant for later discussions in this work.

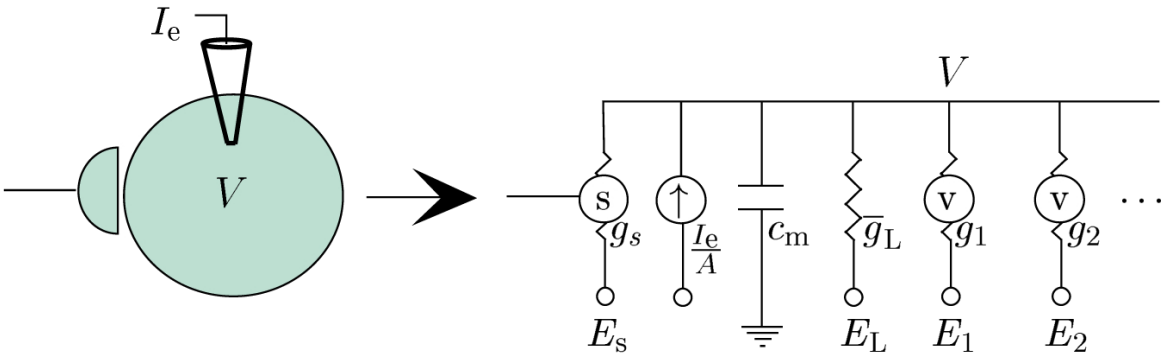

Figure 2.3: The equivalent circuit of a nerve cell, with capacitance c_m, two voltage gated ionic currents (g_1,g_2), a leakage current (g_l), synaptic inputs (g_s) and an external electrode current (I_e). Taken from [3].

2.4.1 Hodgkin-Huxley model

The Hodgkin-Huxley model [5] was the first conductance based model, derived in 1952 by Hodgkin and Huxley from measurements of the membrane potential in the squid giant axon. In their model, they included a population of ion channels selective for sodium ions and a population selective for potassium ions. Figure 2.4A shows a spike generated by this model. Notice how the fraction of open sodium channels rises at the spike initiation and how the fraction of open potassium channels rises when the voltage drops again.

The sodium trans-membrane current is then modelled according to the scheme of figure 2.2C, with rate functions

$$\alpha_m(V) = -0.1\frac{V+40}{\exp(-0.1(V+40))-1} \tag{2.19}$$

$$\beta_m(V) = 4\exp(-(V+65)/18) \tag{2.20}$$

$$\alpha_h(V) = 0.07\exp(-(V+65)/20) \tag{2.21}$$

$$\beta_h(V) = \frac{1}{\exp(-0.1(V+35))+1}, \tag{2.22}$$

$$\tag{2.23}$$

a maximal conductance given by $\overline{g}_{\mathrm{Na}} = 120\ \mathrm{mS/cm^2}$ and a reversal potential $E_{\mathrm{Na}} = 50$ mV.

The potassium current is modelled according to the kinetic scheme of figure 2.2B, with

rate functions

$$\alpha_n(V) = -0.01\frac{V+55}{\exp(-0.1(V+55))-1} \tag{2.24}$$

$$\beta_n(V) = 0.125\exp(-(V+65)/80) \tag{2.25}$$

$$\tag{2.26}$$

a maximal conductance $overline g_{\mathrm{K}} = 36\ \mathrm{mS/cm^2}$ and a reversal potential $E_{\mathrm{K}} = 50$ mV. The leakage current is specified by $g_l = 0.3\ \mathrm{mS/cm^2}$ and $E_l = -54.3$ mV.

2.4.2 Connor-Stevens model

The Connor-Stevens model [8] is a modified form of the Hodgkin-Huxley model. It contains the sodium, potassium and leakage currents of the normal Hodgkin-Huxley model, but with slightly modified parameters, and an extra potassium current (commonly referred to as the A-current). This potassium current is not responsible for drawing the voltage down after the action potential and introducing an refractory period, but balancing the rise of the voltage due to the sodium current. Thus these potassium channels are mostly open at the spike initiation. This causes interesting dynamical effects that will turn out to be particularly useful in this work. We discuss them in the next paragraph. In figure 2.4B we show a spike generated by this model. Notice how there is a fraction of open potassium channels (those of the a-current) at the spike-initiation.

The kinetic scheme of this current is also given by figure 2.2B, but commonly the variables denoted by m are replaced by a and the variables denoted by h are replaced by b. The kinetics are only specified by the asymptotic values a_∞, b_∞ and relaxation times τ_a, τ_b, given by

$$a_\infty(V) = \left[\frac{0.0761\exp(0.0314(V+94.22))}{1+\exp(0.0346(V+1.17))}\right]^{1/3} \tag{2.27}$$

$$\tau_a(V) = 0.3632 + \frac{1.158}{1+\exp(0.0497(V+55.96))} \tag{2.28}$$

$$b_\infty(V) = \left[\frac{1}{1+\exp(0.0688(V+53.3))}\right]^4 \tag{2.29}$$

$$\tau_b(V) = 1.24 + \frac{2.678}{1+\exp(0.0624(V+50))}, \tag{2.30}$$

$$\tag{2.31}$$

but these functions can be transformed back straightforwardly to reaction rates by (2.10). The maximal conductance is $\overline{g}_{\mathrm{a}} = 47.7\ \mathrm{mS/cm^2}$ and the reversal potential $E_a = -75$ mV.

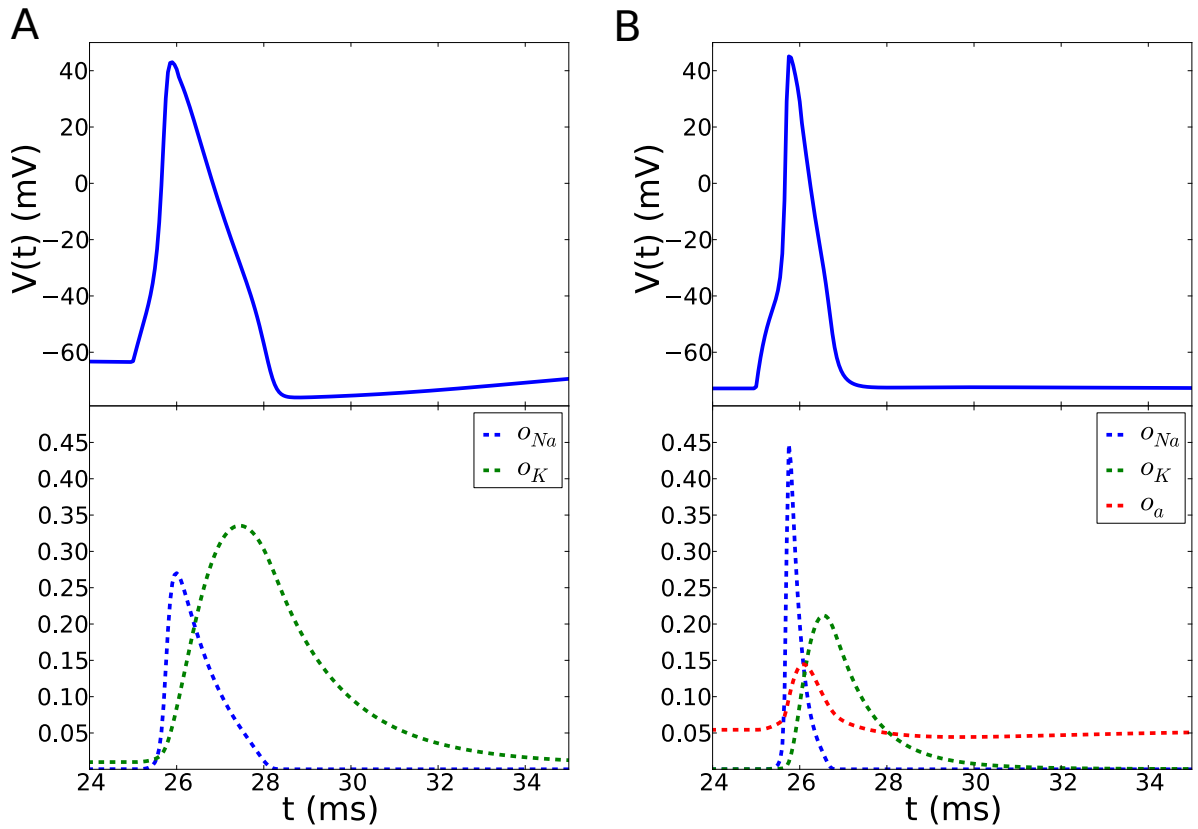

Figure 2.4: (**A**) A spike in the Hodgkin-Huxley model. (**B**) A spike in the Connor-Stevens model. Both spikes are plotted with the respective fractions of open channels of their currents.

The normal potassium current is then given by the maximal conductance $\overline{g}_{\mathrm{K}} = 20\ \mathrm{mS/cm}^2$, reversal potential $E_{\mathrm{K}} = -72\ \mathrm{mV}$ and reaction rates

$$\alpha_n(V) = -0.02\frac{V + 45.7}{\exp(-0.1(V + 45.7)) - 1} \tag{2.32}$$

$$\beta_n(V) = 0.25\exp(-(V + 55.7)/80) \tag{2.33}$$

$$\tag{2.34}$$

whereas the sodium current is specified by the maximal conductance $\overline{g}_{\mathrm{Na}} = 120\mathrm{mS/cm}^2$,

the reversal potential $E_{\mathrm{Na}} = 55$ mV and reaction rates

$$\alpha_m(V) = -0.38\frac{V + 29.7}{\exp(-0.1(V + 29.7)) - 1} \tag{2.35}$$

$$\beta_m(V) = 15.2\exp(-(V + 54.7)/18) \tag{2.36}$$

$$\alpha_h(V) = 0.266\exp(-(V + 48)/20) \tag{2.37}$$

$$\beta_h(V) = \frac{3.8}{\exp(-0.1(V + 18)) + 1} \tag{2.38}$$

$$\tag{2.39}$$

Finally the leakage current is specified by $g_l = 3\,\mathrm{mS/cm}^2$ and $E_l = -17\,\mathrm{mV}$. Note that for convenience we took $E_l = -54.3\,\mathrm{mV}$ throughout our simulations, as this does not change the qualitative behaviour of the model.

2.5 Phase space and spike failures

In this section we expose some of the dynamic properties that differ between the models. A stimulation protocol that is often applied in experiments, consists in injecting a constant current into the neuron: in the charge-balance equation, this translates to

$$I_{ext}(t) = I_0. \tag{2.40}$$

Upon simulating such a protocol, the neuron may spike at a high rate, at a low rate or not at all, depending on the amplitude I_0. In the Hodgkin-Huxley model, the mean spike-rate rises discontinuously from zero when I_0 is increased. Neurons for which this happens are labelled as 'type II' neurons [11],[3]. In the Connor-Stevens model, the spike-rate will rise continuously from zero when I_0 is above a threshold. Such neurons are labelled as 'type I' neurons. Thus the spike rate can be arbitrarily low in the Connor-Stevens model. This happens because at spike initiation, the sodium current and the A-current balance each other, causing a possibly very slow rise in the voltage. Such a slow rise is impossible in the Hodgkin-Huxley model.

Another interesting consequence of including such an a-current, that will turn out to be particularly interesting for this thesis, is that the response characteristics when the neuron is injected with a short, strong current pulse are fundamentally different for different values of $\overline{g}_{\mathrm{Na}}$. If $\overline{g}_{\mathrm{Na}}$ is decreased, the deviation from the equilibrium potential (i.e. the amplitude of the spike) decreases continuously in the Hodgkin-Huxley model. In the Connor-Stevens model, this deviation decreases discontinuously. This is relevant, because it is in fact

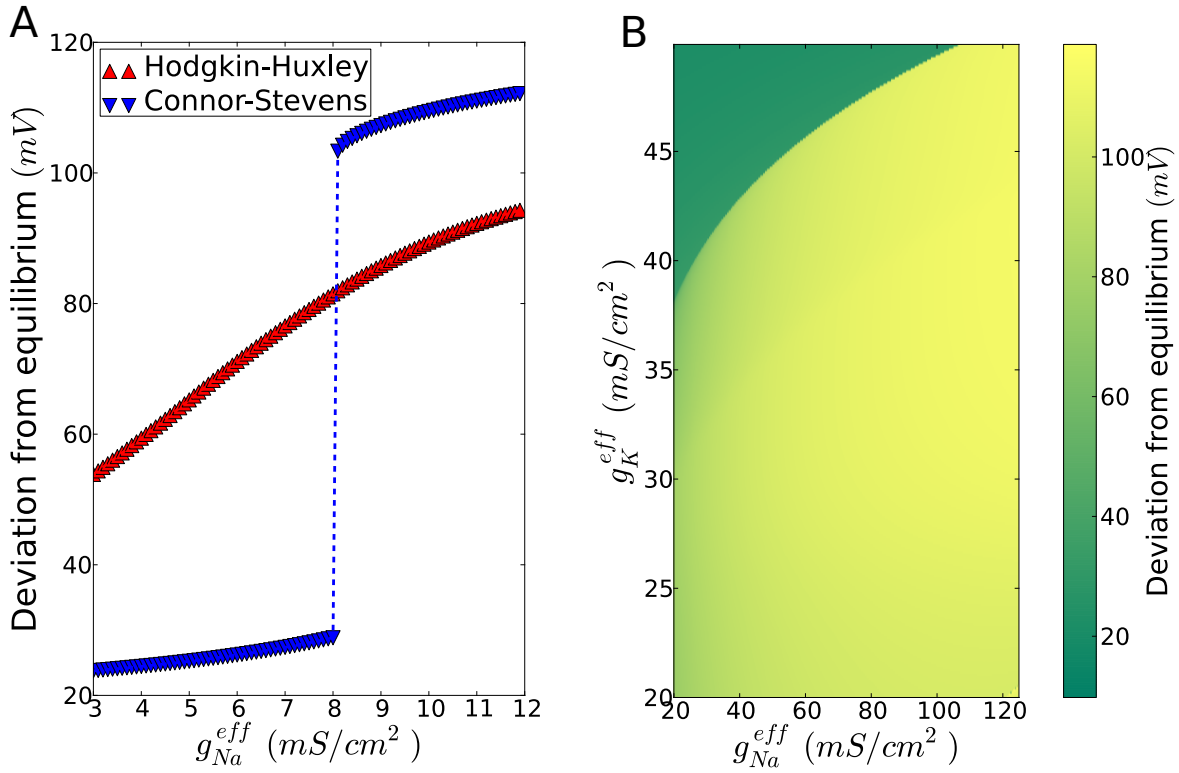

Figure 2.5: (**A**) Deviation from the equilibrium potential after a stimulation for varying maximal conductances. (**B**) Deviation from equilibrium for the Connor-Stevens model for different values of both the maximal conductance of the sodium current and the maximal conductance of the potassium current

known that the maximal conductances may vary, as channels in the cell membrane can become inactive for some time or can be removed from the membrane altogether. We show this effect in figure 2.5A. In figure 2.5B we scan the whole phase space of maximal conductances of the currents in the Connor-Stevens model relevant at spike initiation. As neurons effectively move around in this phase space under repeated activity, interesting effects may arise from this discontinuous boundary.

Chapter 3

Spike-failures and scale-invariant excitability

3.1 Experimental protocol and set-up

As discussed in the introduction, the ultimate goal in computational neuroscience is to understand the emergent properties of biologically realistic neural networks, in terms of information processing, information storage and learning. However, if one looks directly at networks of neurons in brain tissue, it is in general very difficult to determine which behaviour emerges as a network property and which behaviour is inherent to the single neurons. Experiments are often performed on isolated neurons, stimulated with electrical currents or charges in which one measures the evolution of the membrane potential to determine when the neuron spiked. To apply such a stimulation, two protocols exist: either a pipette is inserted in the cell membrane, and through that pipette currents are recorded or injected, or an electrode is held in the vicinity of the cell, and a charge is applied so that the neuron is stimulated from the outside. The second protocol has the advantage that the membrane is left intact, so that the cells under examination can survive much longer ($\sim$ days) than cells whose membrane is penetrated ($\sim$ hours).

Many temporal patterns of stimulation have been used, from random currents to highly precise periodic pulses. All of these protocols are aimed at uncovering key aspects of the neuronal dynamics, such as the activation or inactivation of certain types of ion channels or the study of neuronal excitability. Recently, experiments using the periodic pulse-protocol with extracellular stimulation have been performed by Gal et al. [6]. These experiments revealed long lasting excitability changes and non-stationarities in the neuronal response characteristics that are not captured in any neuron model to date, as we show in the next

chapter.

The measurements were performed on cultured neurons, isolated from the network they are embedded in by using synaptic blockers. An array of electrodes (micro-electrode array or MEA) is present in the substrates on which the neurons are grown and through one of these electrodes electric pulses were applied. In this experimental set-up, spikes are elicited antidromically by stimulating with an electrode, and responses are recorded with a second electrode. This set-up is depicted in figure 3.1, where the electrode closest to the coloured neuron's axon (1) could for instance deliver the pulses, and the electrode closest to the soma (2) could record the action potential. Since the spikes were recorded non-invasively (the cell-membrane was not penetrated), measurements as these could last up to a few days.

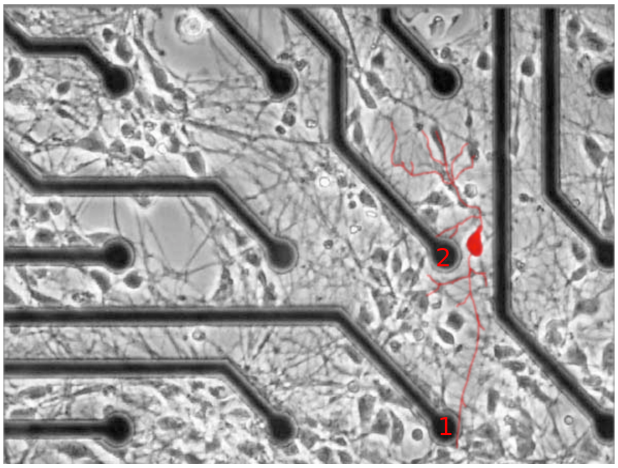

Figure 3.1: The experimental set-up. The electrodes of the MEA are clearly visible in between the nerve cells. A neuron is coloured red for illustrative purposes.

3.2 Transient phases and intermittency

Upon injecting a short, strong current pulse as described above, one reasonably expects the neuron to fire an action potential every time. If done with sufficiently long intervals in between, this is indeed what happens: at low frequencies of stimulation ($\sim 1\,\mathrm{Hz}$), the response is always one-to-one. However, if the frequency of the stimulation is increased (~ 10 to $50\,\mathrm{Hz}$), it seems that the neuron does not have sufficient time to recover: slowly the latency, defined as the delay between stimulation and action potential, starts to increase. Interestingly, there seems to be a critical latency and if reached, the spike response is no longer one-to-one. Not every stimulation elicits a spike. If the stimulation rate is then

decreased to its original value, the spike-response again settles in a one-to-one regime and the latency slowly returns to its original value. These effects are shown in figure 3.2. We will adopt the nomenclature of [6] and refer to the regimes with increasing or decreasing latency and one-to-one response as transient phases and to the regime where the response is not one-to-one as the intermittent phase.

3.2.1 Experimental probes

Several measures can be defined to characterize the response patterns defined above: most straightforwardly, we can look at plots of the latency versus time. On such plots, transient phases will be visible as slowly increasing latencies and during the intermittent phase these plots will look chaotic (figure 3.3A). The durations of the transient phases, especially the first transient of increasing latency, can be studied for different stimulation frequencies (figure 3.3B). Any model that aims to describe these experiments, should reproduce these durations for at least a wide range of frequencies. These durations should also diverge for the very low simulation rates (intermittency is never reached). Another interesting measure -albeit a bit a tricky one, as will be discussed in paragraph 3.3- is the equilibrium spike rate. Since the response is not one-to-one, this rate will be lower than the simulation rate. Interestingly enough, this equilibrium spike rate seems to be largely independent of the stimulation rate (figure 3.3C). It may also be noted that the latencies during the intermittent phase are always higher than during the stable phase. Finally, the failures during the intermittent phase don't always seem to occur in a purely random manner. Often, sequences of spike are followed by sequences of failures (figures 3.3E and 3.3F)

3.3 Scale-invariant excitability

In the previous paragraph we discussed observed effects that last over long time scales ($\sim$ 10 s to $\sim$ 100 s) compared to the time scales on which the general conductance based models operate ($\sim$ 1 ms to $\sim$ 100 ms). However, during the intermittent phase, even longer time-scales seem to be present in the neuronal excitability: upon measuring the spike rate for behaviourally relevant durations of hours and days, it was observed that this rate varied on many time scales. Long periods of activity were followed by long periods of inactivity. These periods seemed to be embedded in even longer periods of overall activity or inactivity. This process repeated itself for all durations that could be measured ($\sim$ 20 to $\sim$ 50 hours), thus pointing to scale-invariance. A convenient visualisation of this process can be achieved by creating a binary array with ones when a stimulation was followed by

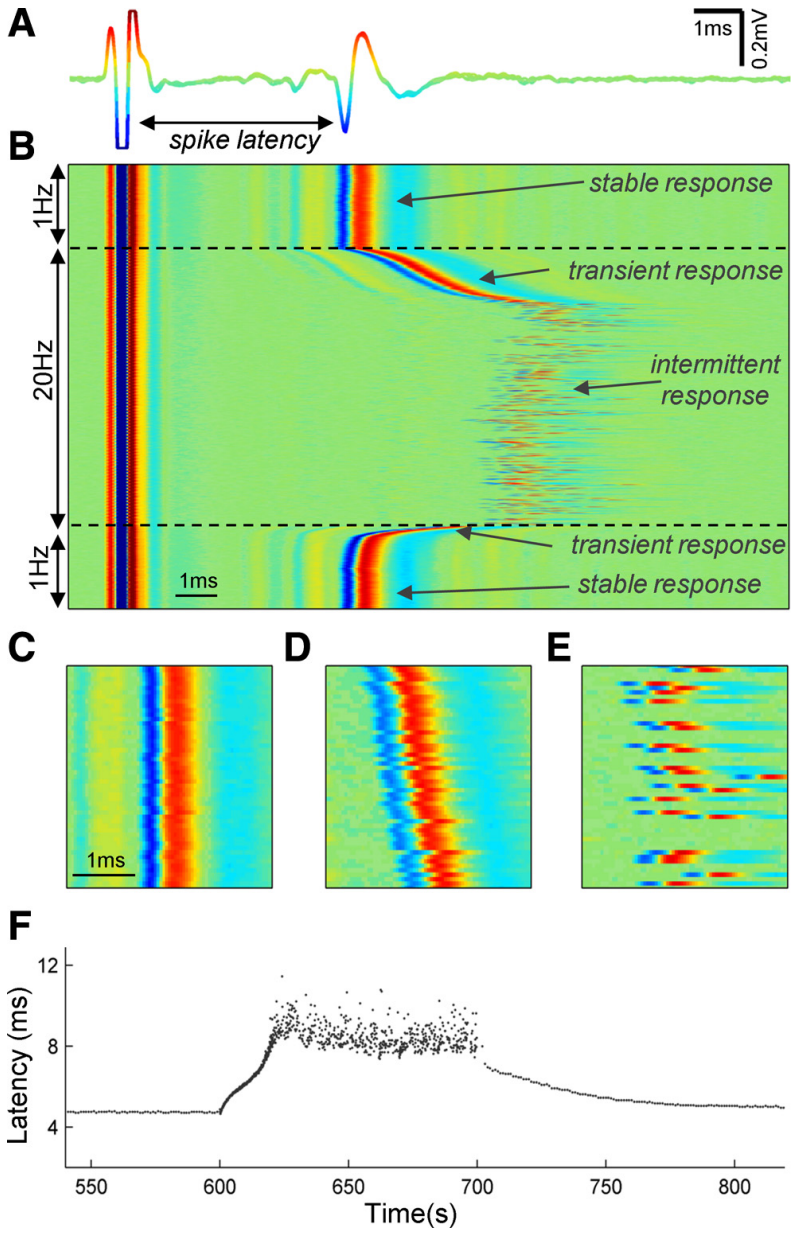

Figure 3.2: (**A**) Voltage trace as recorded by the an electrode of the MEA, stimulation and response are visible. (**B**) The same neuron, stimulated for 600 s at 1 Hz, then for 100 s at 20 Hz and then again for 600 s at 1 Hz. (**C**),(**D**) and (**E**) are zooms of the response patterns. (**F**) is the spike latency versus the time. Taken from [6]

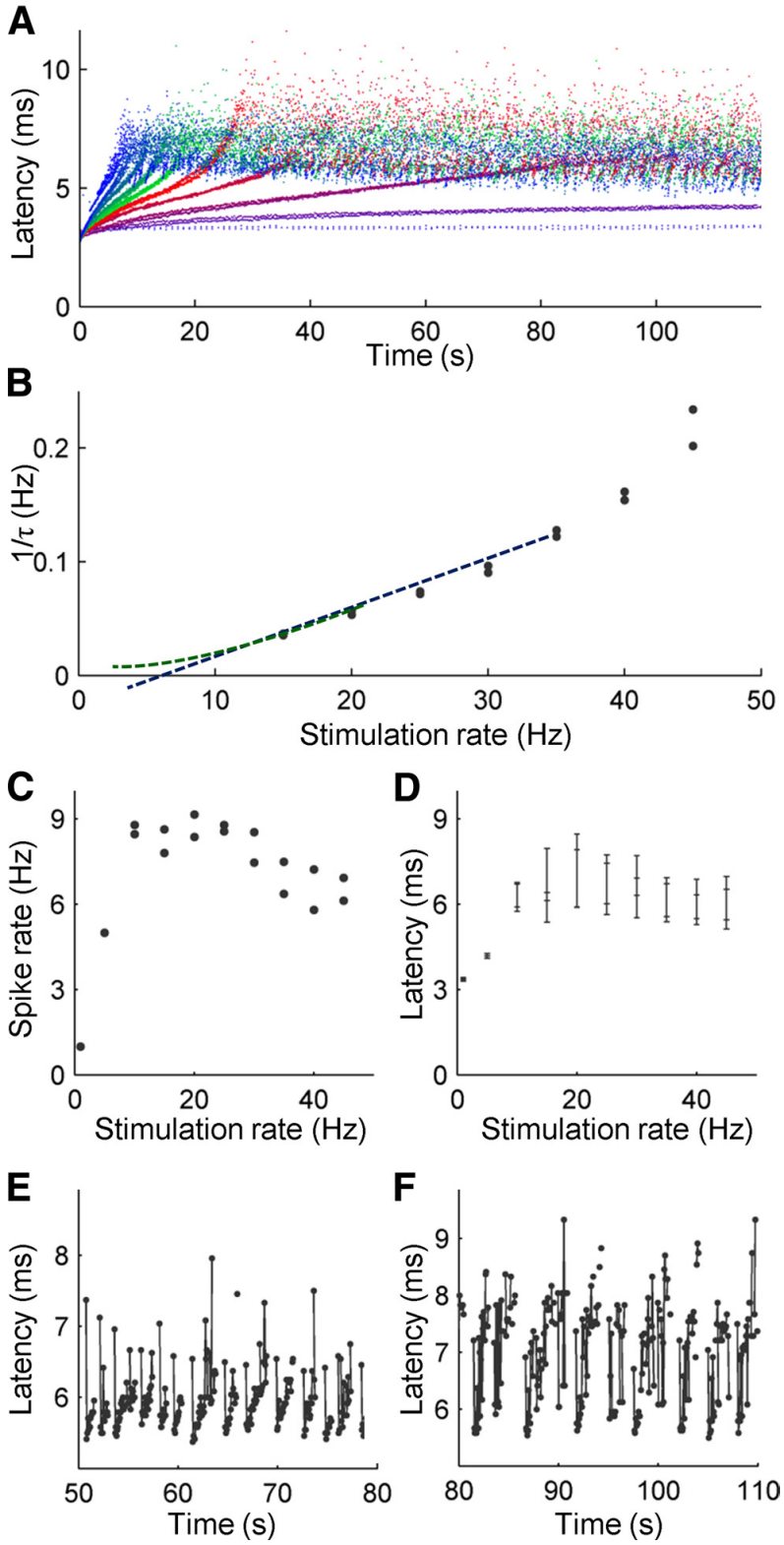

Figure 3.3: Measurements for stimulation rates of 1, 5, 10, 15, 20, 25, 30, 35, 40 and 45 Hz. Stimulations were delivered in block of 120 s. (**A**) Latencies as a function of time. (**B**) $1/\tau$, where τ is the half-time it takes to reach intermittency from the start of the stimulation. (**C**) Steady state spike rates, defined as the mean spike rate during the last 30 s of each block. (**D**) Minimal and maximal latencies. (**E**), (**F**) Visualizations of the response patterns, where successive spikes are connected with lines. (Taken from [6])

a spike and zeros when the stimulation failed to elicit a spike. In figure 3.4A such an array is shown, sliced in sequences that are put on top of each other. Figure 3.4B shows the spike-rate of one neuron, binned using bin widths of 5 minutes. Figure 3.4C shows that the spike-shapes were stable during the experiments.

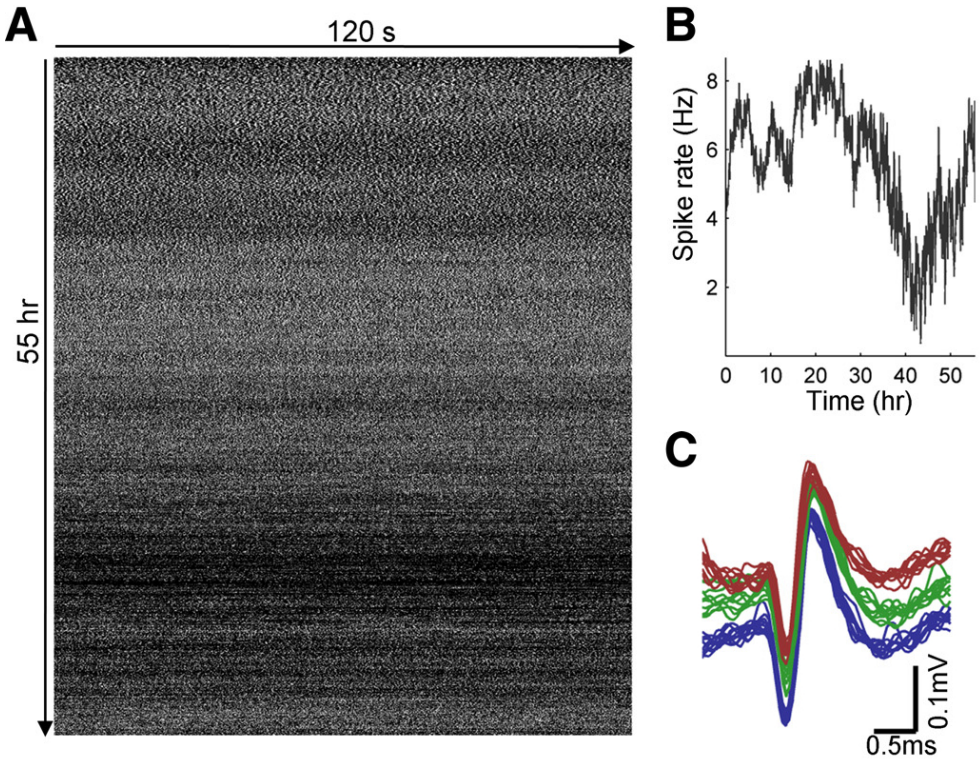

Figure 3.4: (**A**) Binary array, black: failure, white: a spike. (**B**) Spike rate of a neuron binned with five-minute intervals. (**C**) Spike shape throughout the experiments. Adapted from [6].

3.3.1 Measures to reveal scale-invariance

Visual inspection is clearly not sufficient to quantify scale-invariance: as a consequence, various measures were developed to reveal the presence of scaling in time-series. In this section we discuss some of them. Figure 3.5 contains these measures for the experimental data.

The most straightforward way to uncover scale-invariance, is to look at the time series at different resolutions (figure 3.5A): upon binning the spike-rate in increasingly larger bins, the fluctuations around the mean should not decay.

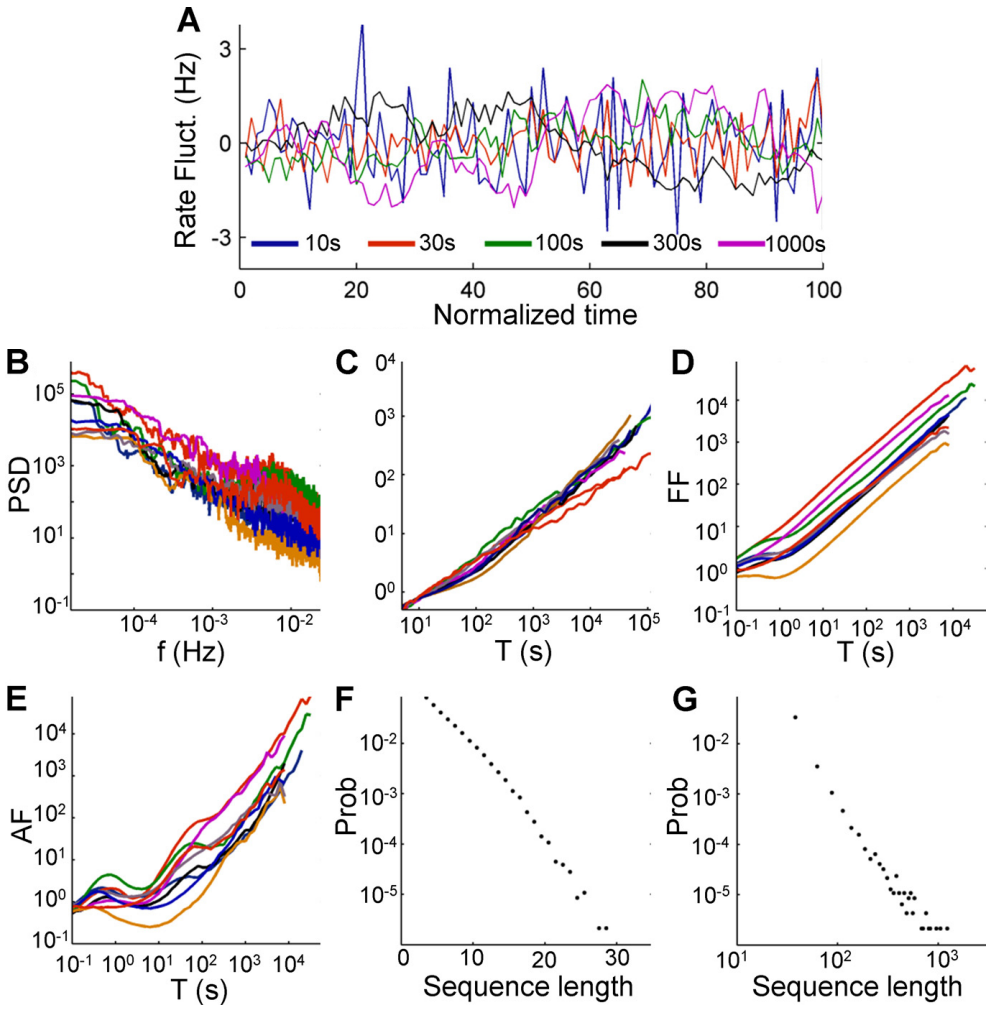

Figure 3.5: (**A**) Rate fluctuation around the mean. (**B**) Periodogram spectral density, (**C**) detrended fluctuation analysis, (**D**) the Fano factor and (**E**) the Allen factor for five different neurons. (**F**) and (**G**) show the distributions of respectively the sequences of consecutive spikes and the sequences of consecutive failures. Sequences of spikes follow an exponential distribution whereas sequences of no spikes follow a power law distribution. Adapted from [6].

The measures of the Fano factor and of the Allen factor [13], shown in figures 3.5E and 3.5F, provide a more quantitative description of this idea, by computing the ratio of the variance and mean of the time series, for different bin widths. If we denote the number of spikes in a bin of length T, starting at time t, by $N(t, t+T)$, then the Fano factor is defined as

$$\mathrm{FF}(T) = \frac{\mathrm{E}(N(t,t+T)^2) - \mathrm{E}(N(t,t+T))^2}{\mathrm{E}(N(t,t+T))} = \frac{V(T)}{N(T)} \tag{3.1}$$

where $V(T)$ denotes the variance and $N(T)$ the mean of the time-series defined by binning in intervals of length T. In our case the time series will be a binary array with ones when there was a spike after a stimulation and zeros if there was no spike after the stimulation. Suppose now that the spikes were generated in an uncorrelated fashion with a certain probability p, and that every stimulation corresponds to a trial to generate a spike: then, the probability of having N spikes in a time-interval of duration T is described by a binomial distribution. If there are $M(T)$ stimulations that time-interval T, the mean number of spikes is given by $N(t) = M(T)p$ and the variance is $V(T) = M(T)p(1-p)$. Hence the Fano factor $V(T)/N(T)$ of such a spike train is independent of the bin size. If scaling is present in the time-series, it can be shown that the Fano factor will rise linearly on a double logarithmic (log-log) plot, with a fractal exponent between zero and one [13]. Related to the Fano factor is the Allen Factor, defined as

$$\mathrm{AF}(T) = \frac{\mathrm{E}[(N(t,t+2T) - N(t,t+T))^2]}{2\mathrm{E}(N(t,t+T))} = 2\mathrm{FF}(T) - \mathrm{FF}(2T) \tag{3.2}$$

Following the same reasoning, the Allen factor is independent of the bin size for a purely random spike train and rises linearly on a loglog plot with increasing bin size if scaling is present.

Figure 3.5C contains the periodogram spectral density. Let R_t be a time series of N data points, in our case the spike rate binned over small intervals. The periodogram of R_t is then defined as:

$$\mathrm{PSD}(\omega) = \frac{1}{N}\left|\sum_{t=1}^{N} R_t e^{-i\omega t}\right|^2 \tag{3.3}$$

If the time series contains only a limited number of frequencies, for instance trough a combination of sines and cosines, the PSD would show sharp peaks around those frequencies. If the time series is scale invariant, no peaks should be present and the periodogram should exhibit $1/\omega$-type behaviour over a wide range of frequencies.

An additional method to uncover scale-invariance is to look at the detrended fluctuations [12]. This eliminates the possibility of erroneously confusing scale-invariance with non-stationariness in the time series, by subtracting the overall trends. Suppose again that R_t is a time series of spike rates: first, R_t is integrated

$$I_t = \sum_{t'=1}^{t} (R_{t'} - \mathrm{E}(R)), \tag{3.4}$$

then the integrated time series is divided in boxes of size n and within those boxes a least-squares line is fit to the data, representing the trend in that box. Let N denote the number of such boxes and I_k^n the result of such a fit in the box to which k belongs. The detrended fluctuations of the time series are then defined as

$$\mathrm{DF}(n) = \sqrt{\frac{1}{M} \sum_{k=1}^{M} (I_k - I_k^n)^2} \tag{3.5}$$

It can be shown that scaling is present if the detrended fluctuations exhibit power law behaviour with an exponent between 1/2 and 1. For purely random spike rates the detrended fluctuations rise with an exponent of 1/2 [12].

Chapter 4

Slow sodium inactivation and long effective time-scales

4.1 Results with classic models

The results described in the previous chapter are unaccounted for by classic models. In simulations, the experimental protocol is mimicked by approximating the voltage pulses delivered extracellularly by the injection of current pulses. $I_{ext}(t)$ from equation (2.18) has the following functional form in this protocol:

$$I_{ext}(t) = \begin{cases} I_0 & \text{if } nT < t < nT + \Delta t \\ 0 & \text{otherwise} \end{cases} \tag{4.1}$$

with $\Delta t = 1\,\text{ms}$. In figures 4.1A and 4.1B we show the equivalent of figure 3.2B for respectively the HH-model and the CS-model. It is to be seen that in neither of these models the intermittent phase is ever reached. There aren't even any traces of a possible transient phase at the experimentally used frequencies (< 50 Hz). This is to be expected, as all the time-scales in these models are of the order of the length of a single spike, i.e. a few milliseconds, whereas the periods of stimulation at these frequencies are of the order or 50 milliseconds. Inevitably, such effects point to presence of variables that retain memory of the previous neuronal activity for a time that is much longer than the relaxation times present in traditional models as the Hodgkin-Huxley or the Connor-Stevens model.

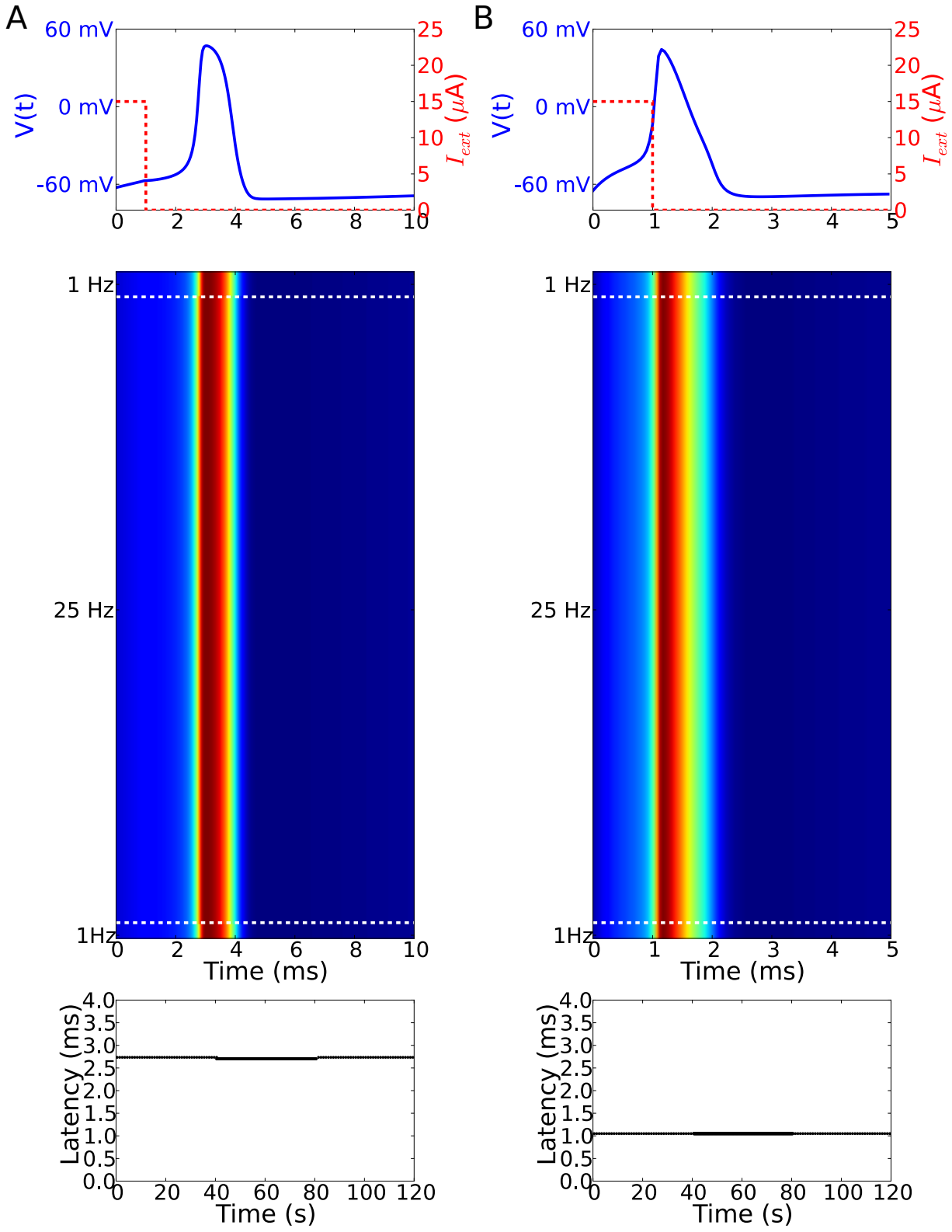

Figure 4.1: Plots of the voltage for (**A**) the HH-model and (**B**) the CS-model. Stimulations were delivered in three block of 40 seconds at rates of 1 Hz, 25 Hz and again 1 Hz. The voltage traces for the first few milliseconds after each stimulation are coloured and put on top of each other.

4.2 Modelling slow sodium inactivation

In the following we introduce a model for a slow, spike-dependent sodium inactivation, inspired by [17]. Such a slow inactivation has been measured experimentally [14] and it is known that inactivating ion channels of the sodium type causes an increase in the spike latency. We add a linear chain of inactive states to the kinetic scheme in figure 2.2C. Channels can enter into this chain from the open state $o_{\mathrm{Na}} = m_3h_1$ according to a voltage-dependent rate $\alpha(V)$ and they return to the state m_0h_0 by means of a slow, voltage-independent rate β. The rates in between the states of the chain are also given by β. We have chosen this configuration because the spike shape is practically unchanged and the inactivation is purely spike-dependent. Figure 4.2 shows this scheme.

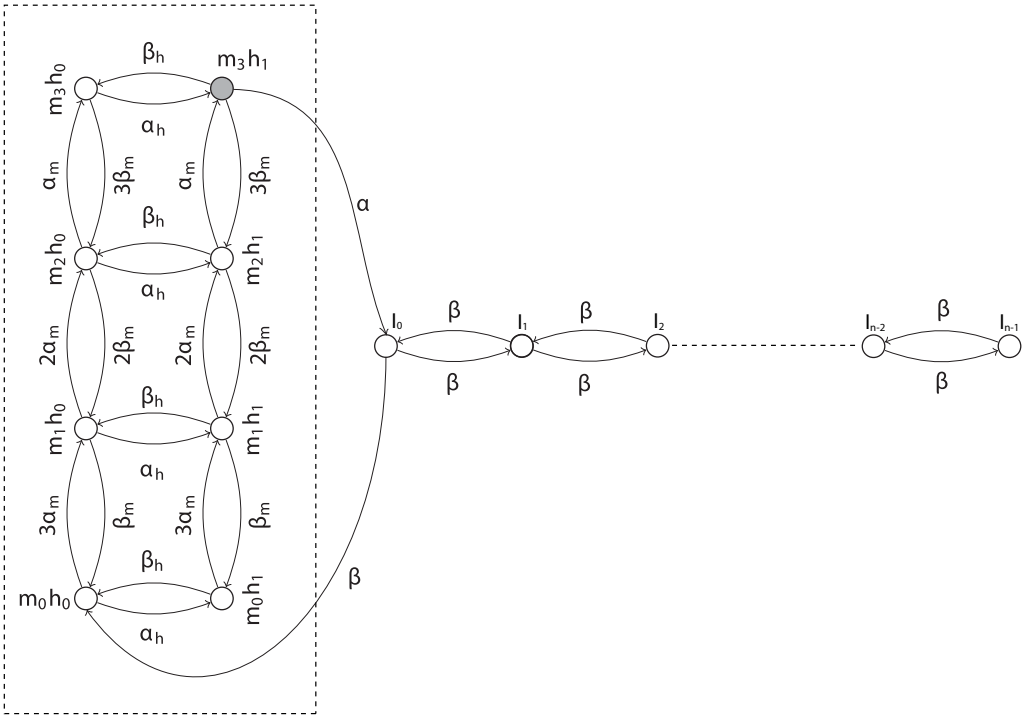

Figure 4.2: The classic kinetic scheme for sodium channels extended with a linear chain of inactive states. All rates except β are voltage-dependent.

Given this scheme, we define a variable a by

$$a(t) = m_0h_0(t) + m_1h_0(t) + \ldots + m_3h_1(t). \tag{4.2}$$

This variable represents the fraction of channels that is not affected by this slow inactivation and hence contributes to the spike. The idea is that there is a clear separation of time scales

between the evolution of a and the typical duration of the spike, so that during a spike a can be considered a constant. Hence a will effectively modify the maximal conductance $\overline{g}_{Na}$ to a lower value $\overline{g}_{\text{eff}} = \overline{g}_{Na}a$.

As follows from figure 2.5, it is better to use the Connor-Steven model than the Hodgkin-Huxley model: in the former there is a clear boundary between spikes and failures at a specific value of $\overline{g}_{\text{eff}}$, and thus of a, something that is not at all present in the Hodgkin-Huxley model, where defining such a boundary would be an arbitrary choice. Figure 4.3 shows the spike shape and the increase in latency for different values of a. We will denote this boundary by a_{thr}. Note that the precise value of a_{thr} is a function of the charge in the injected current pulse.

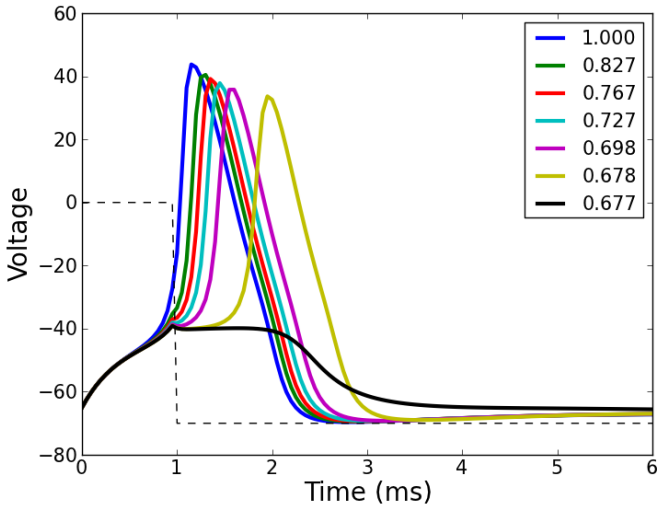

Figure 4.3: Spike shapes for different values of a in the Connor-Stevens model. As a decreases, the latency increases until a reaches a critical values, below which the event can no longer be classified as a spike.

Every time a spike is generated in this model, a fraction of channels inactivates due to the rate $\alpha(V)$ and returns only very slowly due to the slow rate β. Thus, under repeated stimulation, a steadily decreases (figure 4.4A) and, as a consequences, the latency increases. This is the transient phase that is observed experimentally. If the stimulation rate is high enough, so that a does not reach a dynamic equilibrium where $a(t) > a_{\text{thr}}$ every time a stimulation is delivered, a will eventually reach the firing threshold a_{thr}. At that point, failures start to occur and the neuron enters the intermittent response phase, where spikes are only fired if $a(t) > a_{\text{thr}}$ at the time of stimulation (shown in figure 4.4B). We depict the evolution of the voltage and latencies in figure 4.5, for a simulation of 300 s, where

the stimulation rate was 1 Hz for the first and last 100 s, and was 25 Hz between 100 s and 200 s.

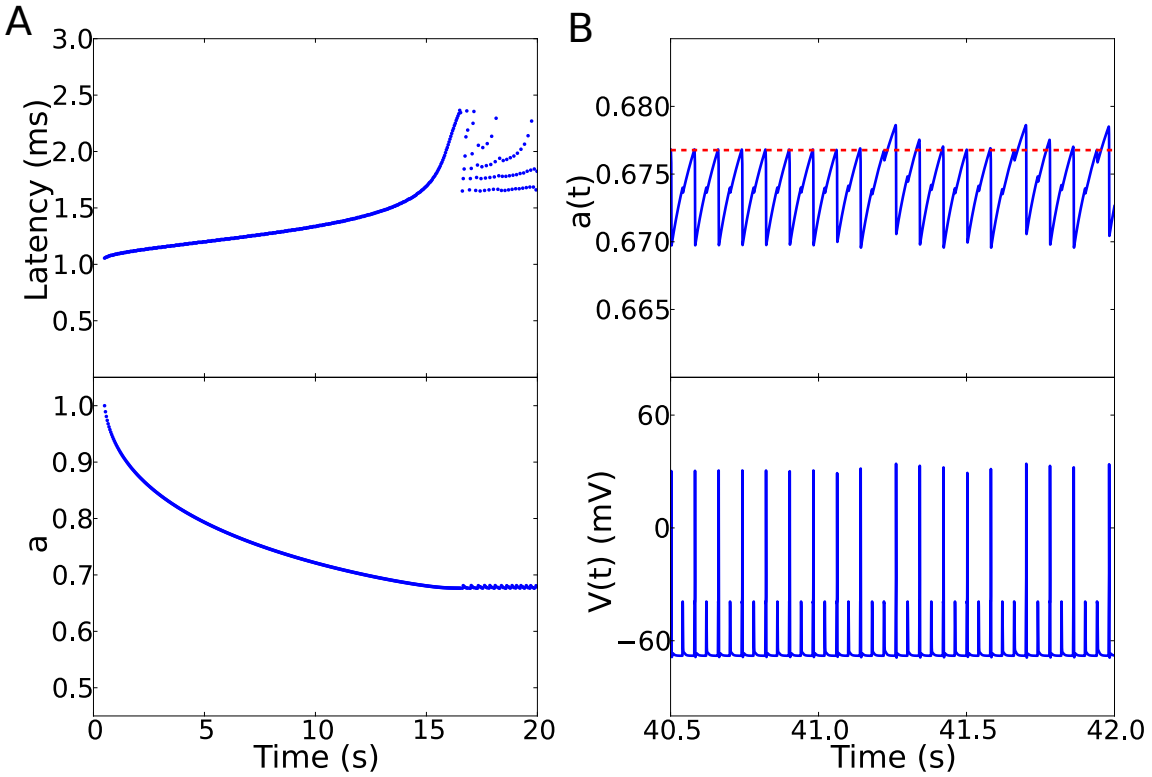

Figure 4.4: (**A**) Evolution of the latency and a during the transient phase and start of the intermittent phase. (**B**) Evolution of a and the membrane potential during the intermittent phase. The stimulation rate was 25 Hz, $\alpha(V)$ was kept constant at $0.1\,\mathrm{ms}^{-1}$ and $\beta = 0.01\,\mathrm{ms}^{-1}$.

As shown in [16] during the course of this works, there exists another, related way of generating the observed transient and intermittent phases. Returning to the subunit picture for sodium channels with a scheme as in figure 2.2C, it is to be seen these channels usually have a fast-inactivating variable h, specified by the rates $\alpha_h(V)$ and $\beta_h(V)$, that is responsible for shutting of the rapid rise in open sodium channels at the spike-initiation, and thus for halting the rapid rise of the voltage. This is represented as $o_{\mathrm{Na}} = m^3h$, where the rate equation of h is of the form (2.14). The relaxation time of this variable is of the order of $\sim$ 1 to 10 ms and, as discussed, it can not relate excitability changes over $\sim$ 50 ms, the typical time scale between the spikes in the experiments of [6]. Therefore one can introduce a slow inactivating variable s (see for instance [15]), that has a much larger

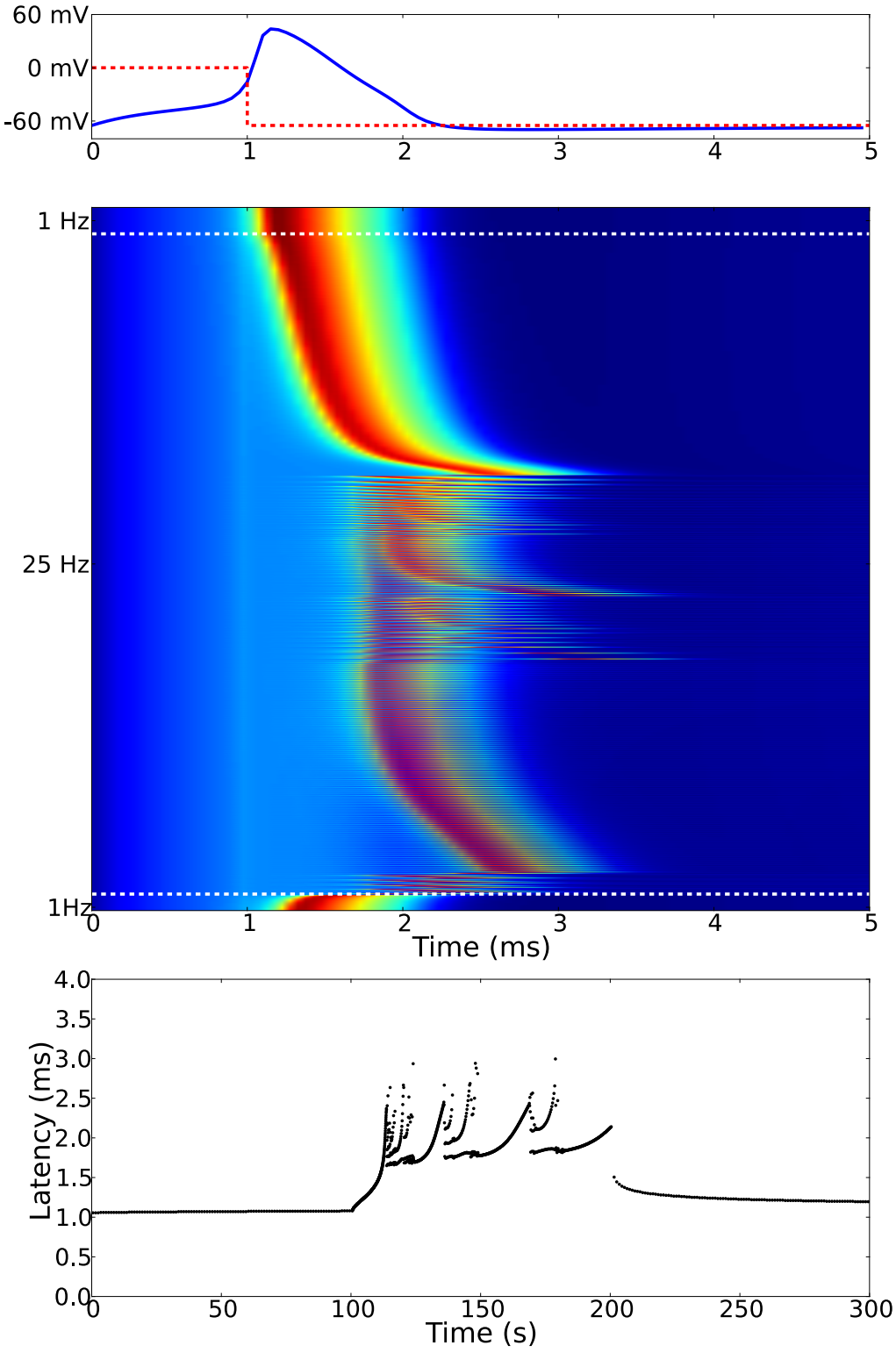

Figure 4.5: A visualisation of the response patterns when stimulations were delivered in three intervals of equal length, at respective rates of 1 Hz, 25 Hz and again 1 Hz and when $\alpha(V)$ was kept constant at $0.1\,\mathrm{ms}^{-1}$ and $\beta = 0.01\,\mathrm{ms}^{-1}$.

relaxation time, so that $o_{\mathrm{Na}} = m^3hs$, whose rates $\alpha_s(V)$ and $\beta_s(V)$ are so that s drops a little bit during every spike and returns slowly to $s = 1$ at the equilibrium potential. Such models have the disadvantage that only a single slow time scale is present in the excitability, whereas the experiments indicate that there is a multiplicity of time scales.

Note that such a variable s is the exact equivalent of a. By applying the mapping from a subunit picture to a kinetic scheme, it can be shown that s is indeed the sum over all states that are not affected by the slow inactivation. Hence our model is a more general case of the HHS-model discussed in [16], that yields the same results if the length of the chain N is one.

4.3 Integro-differential representation

As explained in the previous paragraph, the variable a represents an important quantity of the system: it determines, in the pulse-stimulation protocol, if the neuron will spike or not. From figure 4.2 and equation (4.2) we see that its evolution is controlled by

$$\frac{\mathrm{d}a}{\mathrm{d}t}(t) = -\alpha(V)o(t) + \beta i_0(t) \tag{4.3}$$

where $o(t) = m_3h_1(t)$, the open state and where $i_0(t)$ is the fraction of channels in the first state of the linear chain $\mathbf{i} = (i_0, i_1, \ldots, i_N)$. We can use the voltage-independence of the transition rates in the chain to write (4.3) as an integro-differential equation that summarizes the total effect of the chain in one memory kernel $f(t)$. This approach will aid us in understanding the system and will hopefully lead to fitting procedures to infer the internal time scale $1/\beta$ from experiments. The equation reads

$$\frac{\mathrm{d}a}{\mathrm{d}t}(t) = -\alpha(V)o(t) + \beta \int_{-\infty}^{t} \alpha(V)o(\xi)f(\beta \cdot (t-\xi))\mathrm{d}\xi \tag{4.4}$$

and we will derive it in the following section.

4.3.1 Memory kernel

To find this kernel, we first need to look at a discrete diffusion problem (see for instance [23]) with $N + 1$ states $i_0, i_1, ..., i_N$, where there is a reflecting boundary at i_N and an adsorbing boundary at i_0

$$i_* \underset{\beta}{\leftarrow} i_0 \underset{\beta}{\overset{\beta}{\rightleftharpoons}} i_1 \underset{\beta}{\overset{\beta}{\rightleftharpoons}} \cdots \underset{\beta}{\overset{\beta}{\rightleftharpoons}} i_N \tag{4.5}$$

Note that the probability mass in the chain $\mathbf{i} = (i_0, i_1, \ldots, i_N)$ is not conserved: when a random walker arrives at i_0, it has a probability of exiting the chain without a chance of returning. We can refer to this by saying the random walker has entered a 'limbo-state' i_*. The probability of being in limbo is $1 - \sum_{n=0}^{N} i_n(t)$. We are interested in the probability $f(t)$ for a random walker to enter this state in the interval $[t, t + \mathrm{d}t]$, starting from the initial condition

$$i_n(t = 0) = \delta_{0n} \text{ for } n = 0, \ldots, n. \tag{4.6}$$

The dynamics of this system are fully described by the following linear system of linear differential equations:

$$\frac{\mathrm{d}i_0}{\mathrm{d}t}(t) = -2\beta i_0(t) + \beta i_1(t) \tag{4.7}$$

$$\frac{\mathrm{d}i_n}{\mathrm{d}t}(t) = \beta i_{i-1}(t) - 2\beta i_n(t) + \beta i_{i+1}(t) \qquad n = 1, ..., N-1 \tag{4.8}$$

$$\frac{\mathrm{d}i_N}{\mathrm{d}t}(t) = \beta i_{N-1}(t) - \beta i_N(t), \tag{4.9}$$

which can be written in compact form as

$$\frac{\mathrm{d}\mathbf{i}}{\mathrm{d}t}(t) = \beta \mathbb{W}\mathbf{i}(t) \tag{4.10}$$

with

$$\mathbb{W} = \begin{pmatrix} -2 & 1 & 0 & 0 & \cdots & 0 & 0 \\ 1 & -2 & 1 & 0 & & 0 & 0 \\ 0 & 1 & -2 & 1 & & 0 & 0 \\ \vdots & & & & \ddots & & \\ 0 & 0 & 0 & 0 & & -2 & 1 \\ 0 & 0 & 0 & 0 & \cdots & 1 & -1 \end{pmatrix}. \tag{4.11}$$

By normalizing time according to $\tau = \beta t$, equation (4.10) can be expressed as

$$\frac{\mathrm{d}\mathbf{i}}{\mathrm{d}\tau}(\tau) = \mathbb{W}\mathbf{i}(\tau). \tag{4.12}$$

Such a system can be expanded in normal modes $\phi_{\lambda_i} e^{-\lambda_i \tau}$, where λ_i is the i-th eigenvalue of $\mathbb{W}$ and ϕ_{λ_i} the corresponding eigenvector: any solution for a given initial condition at time $t = 0$ can be written as a linear superposition of exponentials. Once we know this, we can calculate the probability mass that will have entered the limbo-state i_* after a time τ, as this is simply $1 - \sum_{n=0}^{N} i_n(\tau)$. The probability mass that will enter this state in the

time interval $[\tau, \tau + \mathrm{d}\tau]$ will then be given by $f(\tau)\mathrm{d}\tau = \frac{\mathrm{d}i_*}{\mathrm{d}\tau}(\tau)\mathrm{d}\tau$. This can be re-expressed as

$$f(\tau) = -\sum_{n=0}^{N} \frac{\mathrm{d}i_n}{\mathrm{d}\tau}(\tau) = i_0(\tau) = \sum_{n=0}^{N} c_\lambda \phi_{0\lambda} e^{-\lambda\tau}, \tag{4.13}$$

where we used equations (4.7)-(4.9) for the second equality.
Now suppose that in every time-interval $[\xi, \xi + \mathrm{d}\xi]$ a probability mass $p_n(\xi) = \delta_{0n} p_{\text{injected}}(\xi)$ is injected at i_0. We can denote the fraction of this mass that will be in the state i_0 at a later time τ by $i_{0\xi}(\tau)$. For this fraction we will have:

$$i_{0\xi}(\tau) = p_{\text{injected}}(\xi) f(\tau - \xi). \tag{4.14}$$

The total amount of probability mass in i_0 is then a linear superposition of all these contributions:

$$i_0(\tau) = \int_{-\infty}^{\tau} i_{0\xi}(\tau)\mathrm{d}\xi = \int_{-\infty}^{\tau} p_{\text{injected}}(\xi) f(\tau - \xi)\mathrm{d}\xi \tag{4.15}$$

We now identify the limbo state i_* with a. In this case $p_{\text{injected}}(\xi) = \alpha(V)o(\xi)$, since this is precisely the fraction of channels that will enter the inactive chain in a time-interval $[\xi, \xi + \mathrm{d}\xi]$. Hence equation (4.15) becomes

$$i_0(\tau) = \int_{-\infty}^{\tau} \alpha(V) o(\xi) f(\tau - \xi)\mathrm{d}\xi. \tag{4.16}$$

Equation (4.4) is then found by substituting this expression in (4.3) and replacing τ by βt.

4.3.2 Effective power law

The memory kernel function found in the previous paragraph turns out to exhibit power law behaviour ($f(\tau) = q\tau^{-m}$) in the range $1 < \tau < 10^4$. Indeed, from figure 4.6a it is clear that we can fit a line to $\log(f(\tau)) \sim -m\log(\tau) + \log(q)$. From a least-square fitting procedure for $N = 100$ the parameters m and q where found to be

$$m = 1.50 \tag{4.17}$$

$$\log(q) = 0.28. \tag{4.18}$$

Hence we can write:

$$f(\tau) \simeq \begin{cases} \sum_{n=0}^{N} c_\lambda \phi_{0\lambda} e^{-\lambda\tau} & \text{if } \tau < 1 \\ q\tau^{-m} & \text{if } 1 < \tau < 10^4. \end{cases} \tag{4.19}$$

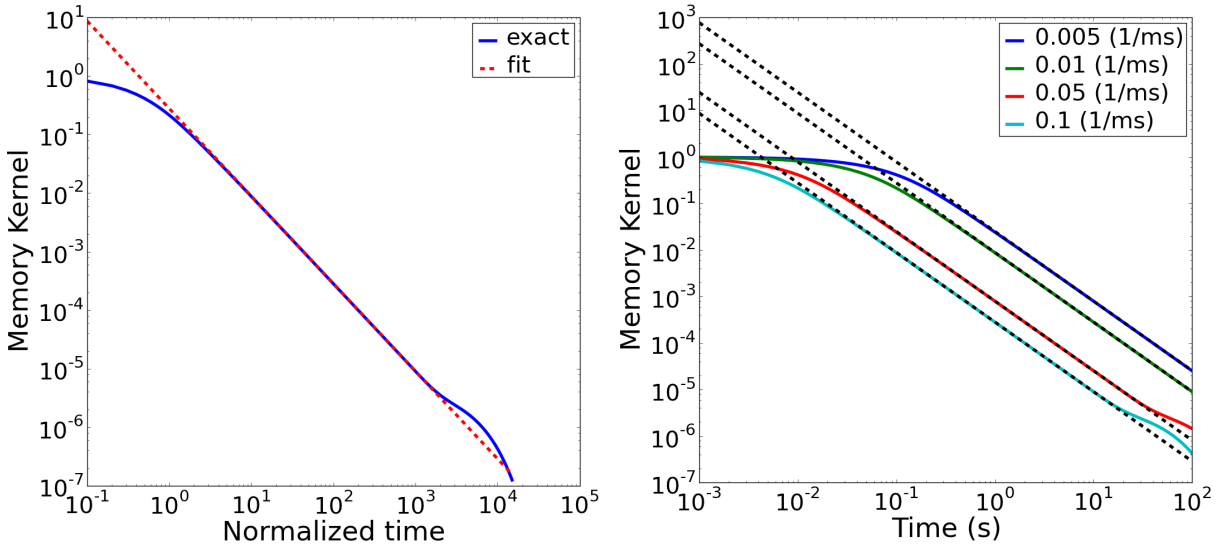

(a) (b)

Figure 4.6: (a) The memory kernel in normalized time, (b) memory kernels for different values of beta, together with their fits according to (4.20)

Going to the physical time $t = \tau/\beta$, this becomes

$$f(\beta t) \simeq \begin{cases} \sum_{n=0}^{N} \phi_{0\lambda} e^{-\lambda\beta t} & \text{if } t < 1/\beta \\ q\beta^{-m} t^{-m} & \text{if } 1/\beta < t < 10^4/\beta. \end{cases} \tag{4.20}$$

This is an interesting result, as it tells us that during the power law regime the only dependence on the rate β is contained in a multiplicative factor. Thus we can imagine that within certain approximations equation (4.4) can be written as

$$\frac{\mathrm{d}a}{\mathrm{d}t}(t) \simeq -\alpha(V)o(t) + q\beta^{1-m} \int_{-\infty}^{t} \alpha(V)o(\xi)(t-\xi)^{-m}\mathrm{d}\xi, \tag{4.21}$$

a form that has potential to result in a fitting procedure for β.

4.4 Results

We compare the results of our model to the experimental results of figure 3.3, taking for a start a step-function inactivation rate $\alpha(V)$, so that at every spike a small fraction of

channels inactivates. We chose

$$\alpha(V) = \begin{cases} 0 \text{ ms}^{-1} & \text{if } V < -20 \text{ mV} \\ 0.15 \text{ ms}^{-1} & \text{if } V > -20 \text{ mV}, \end{cases} \tag{4.22}$$

a chain-length of $N = 100$ and $\beta = 0.01\,\text{ms}^{-1}$. We conduct simulations of 600 s and plot similar quantities as the ones in figure 3.3. The duration of the transient phase is calculated by taking the time from the start of the simulation until the first failure (figure 4.7B). We shall adopt the nomenclature of [6] and call this duration τ. We calculate the steady state spike-rate (figure 4.7C) by averaging the spike-rate over the last 150 s of each simulation. The latency interval is simply defined by the minimal and maximal latency measured during the intermittent phase (figure 4.7D). We also show the response patterns at different times during the simulation (figure 4.7E and 4.7F).

It is to be seen that the qualitative behaviour of the latencies versus time is already quite good (figure 4.7A). The slightly curved shape one gets by plotting the reciprocal of the duration of the transient phase as a function of the stimulation rate also agrees quite well with the experiments (figure 4.7B). While the steady-state spike-rate (figure 4.7C) is quantitatively different, the qualitative result that this spike-rate is more or less independent of the stimulation rate is also reproduced. The minimal and maximal latencies during the intermittent phase are always higher than in the stable response phase (figure 4.7D), but their quantitative values do not agree with the experiments. This is not so surprising, as these values depend sensitively on the precise types of trans-membrane currents, and small differences in these currents may cause big differences in the latencies. Moreover, in the experiments, action potentials travel through the axon before they can be recorded, which may cause them to be delayed even further. It is also to be seen that the response patterns in our model are different from the bursting response patterns measured experimentally. It was suggested that this may be caused by different, slowly inactivating or slowly activating potassium currents [16], but an accurate study of the effects of such currents is out of the scope of this work.

4.4.1 Entry rate functions

In this section we compare different rate functions to enter the inactive chain. We check the behaviour for the step function (4.22), a constant inactivation rate $\alpha(V) = 0.01$ ms^{-1}, an exponential

$$\alpha(V) = 0.04 \exp(0.025(V + 25)) \text{ ms}^{-1}, \tag{4.23}$$

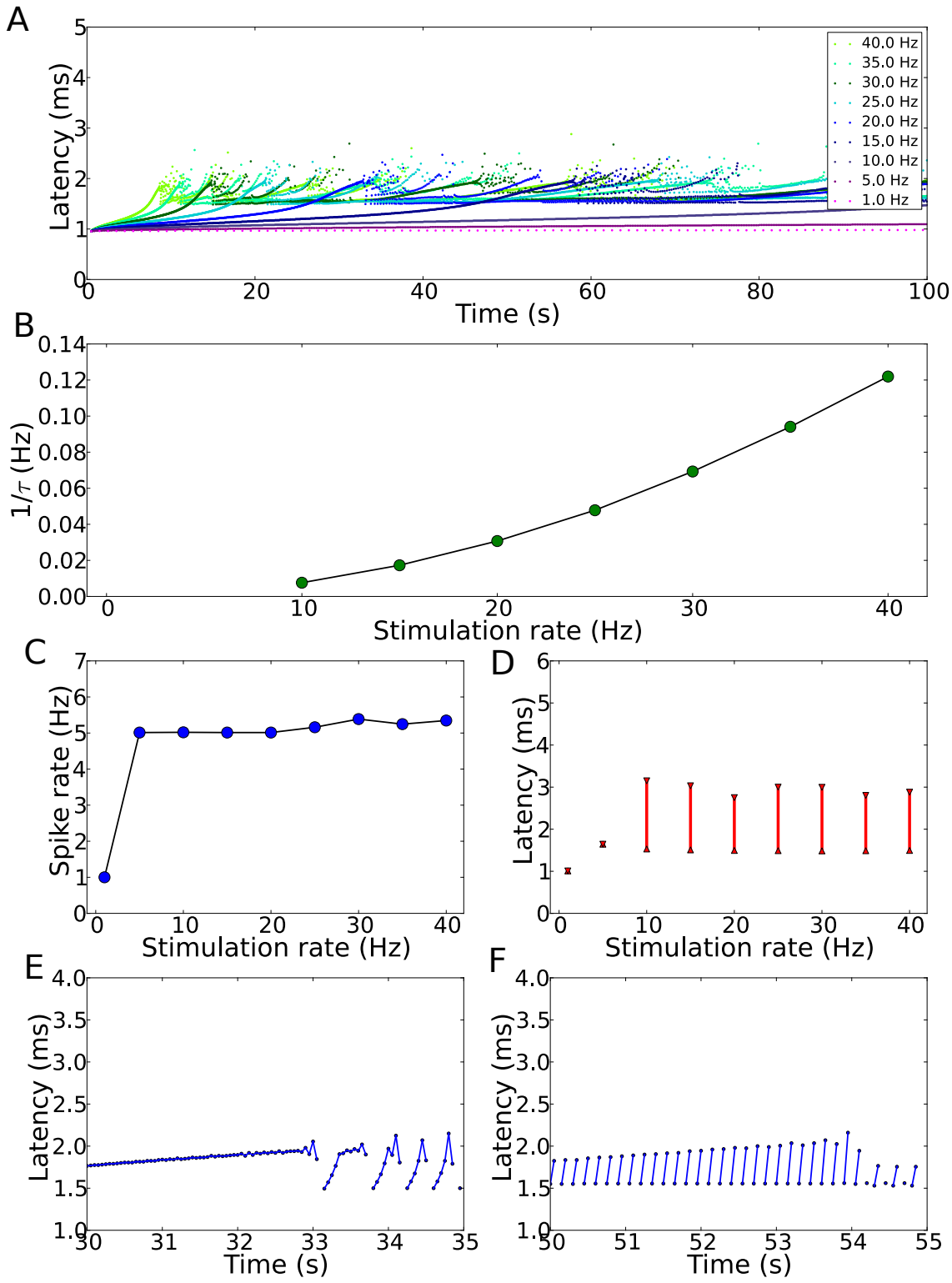

Figure 4.7: Simulations of the periodic stimulation protocol, conducted over 600 s for stimulation rates of $1, 5, 10, 15, 20, 25, 30, 35$ and 40 Hz. (**A**) Latencies as a function of time during the first 100 s of the simulation. (**B**) Reciprocals of the duration τ of the transient phase as a function of the stimulation rate. (**C**) Steady-state spike rates measured over the interval 450 to 600 s. (**D**) minimal and maximal latencies. (**E**)-(**F**) Response patterns at different points in the simulation. In (**E**) the transient phase breaks down and in (**F**) the neuron goes from a regime with two spikes after every failure to a regime with either one or two spikes after every failure.

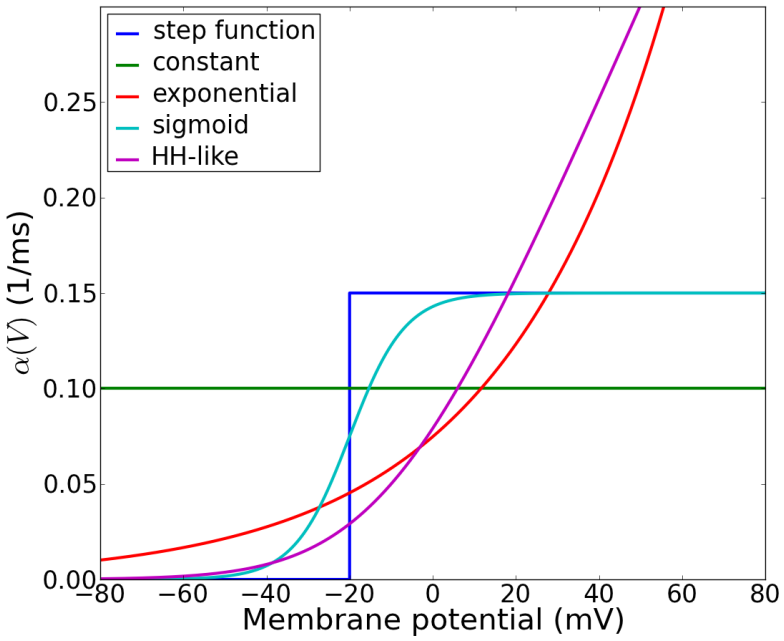

Figure 4.8: Different entry rate function plotted in function of the membrane potential.

a sigmoid

$$\alpha(V) = \frac{0.15}{\exp(-0.15(V+20))+1}\ \mathrm{ms}^{-1}, \tag{4.24}$$

and a Hodgkin-Huxley like rate function

$$\alpha(V) = \frac{-0.005(V+10)}{\exp(-0.1(V+10))-1}\ \mathrm{ms}^{-1}. \tag{4.25}$$

Equation (4.24) is the continuous approximation of step-function inactivation rate, thus we expect similar results for these two inactivation rates. Equations (4.23) and (4.25) feature the more traditional forms used in Hodgkin-Huxley formalisms. These functions are plotted in figure 4.8. We have chosen these functions so that the fraction of channels that inactivates during the spike is largely similar. As can be seen, the inactivation rates (4.23) and (4.25) emphasize the height of the spike more than the rates (4.22) and (4.24): for the former more channels will inactivate if a strong spike occurs than for the latter. As a consequence, a will drop faster at the start of the simulation for (4.23) and (4.25) than for (4.22) and (4.24), resulting in a different shape of the latency as a function of time.

Figure 4.9 shows the behaviour of the latencies as a function of time during during simulations according to the same protocol as described above. Figure 4.9A shows the

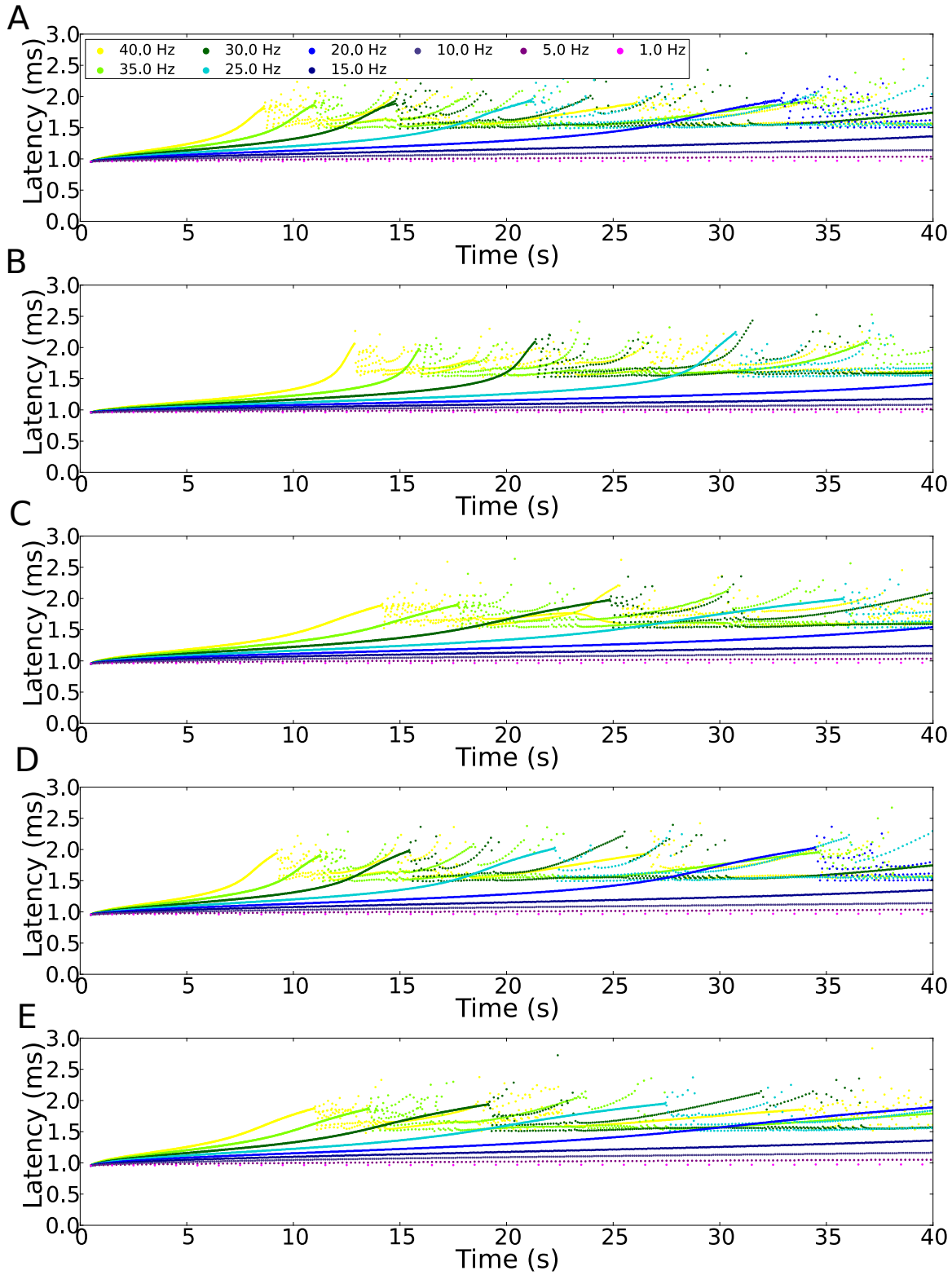

Figure 4.9: Latencies as a function of time during the first 40 s of stimulation at rates of $1, 5, 10, 15, 20, 25, 30, 35$ and 40 Hz. (**A**) A step-function inactivation rate, (**B**) a constant rate, (**C**) an exponential rate, (**D**) a sigmoid rate and (**E**) a HH-like rate.

step-function inactivation rate, figure 4.9B the constant rate, figure 4.9C the exponential rate, figure 4.9D the sigmoidal rate and figure 4.9E the HH-like rate. Minor differences exist in the way the latency rises during the transient phases: the inactivation rates (4.23) and (4.25) that emphasize the amplitude of the spike indeed yield a slightly different shape than the rates (4.22) and (4.24), that is more concave in the second part of the transient phase. In general, qualitatively similar functions indeed give qualitatively similar results (compare panels A and D and panels C and E of figure 4.9).

In figure 4.10A we show the reciprocals of the durations of the transient phases, recorded as explained earlier. It is to be seen that there is little difference and all of these rate-function can fit the experiments reasonably well. The steady state spike rates however can not, as can be seen in figure 4.10B. Only the step-function and sigmoid inactivation rate are compatible with stead state rates that are independent of the stimulation rate. This motivates us, from the point of view of simplicity, to use the step-function inactivation rate for the remainder of this work.

4.4.2 Chain length

The second question we ask ourselves is how the experimental probes described above change with the length of the chain. To analyse this we conducted 600 s-long simulations according to the same protocol as described above, with the step function inactivation rate, where we varied the number of states N in the inactive chain. We took $N = 1, 5, 10, 50, 100$. When rescaling N, it is apparent that the value of β needs to be rescaled too. A model neuron with $N = 100$ and $\beta = 0.01\text{ms}^{-1}$ might have no trouble reaching intermittency, whereas for a model neuron with $N = 1$ the latency during high-frequency stimulation might not even change appreciably at this value of β. We therefore conducted simulations for each N where β ranged between 0.1ms^{-1} and 0.00001ms^{-1}, if those values were relevant for the given N. In figure 4.11 we show the latencies as a function of time for chain lengths of $N = 1, 5, 10, 50$ and 100 and $\beta = 0.0001, 0.001, 0.001, 0.01$ and $0.01\,\text{ms}^{-1}$ respectively. It can be seen that the longer chain lengths do a better job at explaining the wide variety of time scales present in the experiments.

In figure 4.12 we show results for the reciprocals of the durations τ of the transient phases and for the steady-state spike rates. For a chainlength of $N = 1$ (figure 4.12A), we conducted simulations with β ranging from 0.01 to $0.00001\,\text{ms}^{-1}$. For $\beta = 0.01\,\text{ms}^{-1}$ the model neuron never reaches intermittency. Intermittency was reached for the lower values of β. Nevertheless the shape of the $1/\tau$-curve as a function of the stimulation rate is always quantitatively off by an order of magnitude. The qualitative shape is also that of a

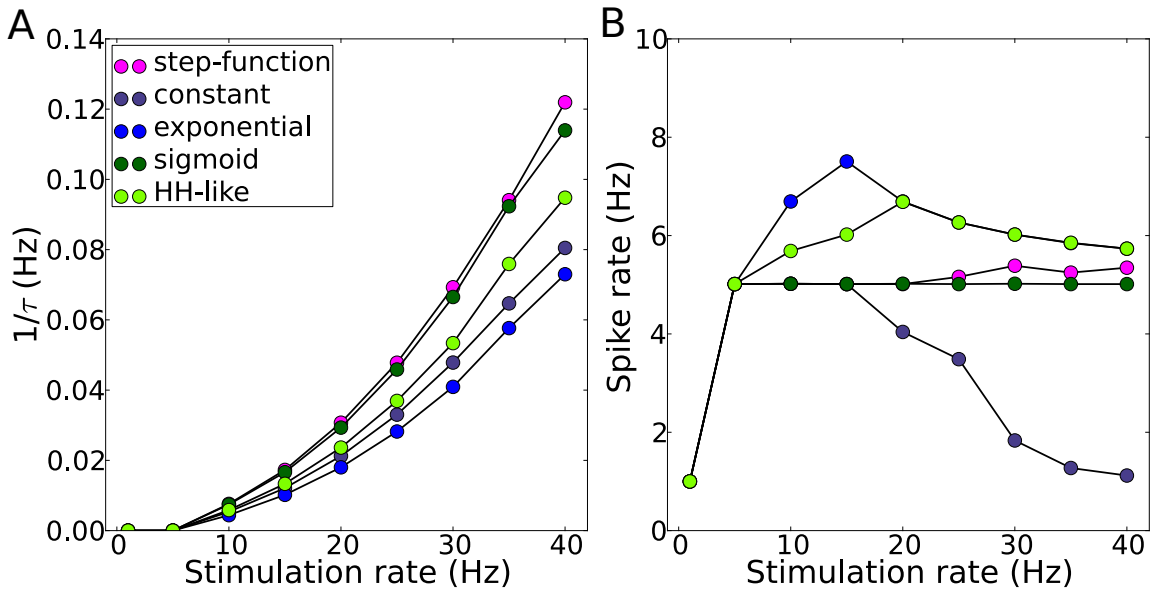

Figure 4.10: (**A**) Reciprocals of the durations of the transient phases and (**B**) steady-state spike rates for the different entry rate functions. Simulated for 600 s with stimulation rates of 1, 5, 10, 15, 20, 25, 30, 35 and 40 Hz.

straight line, instead of a curved line. Adjusting the value of β, steady-state spike-rates can be tuned to fit the experiments. For $N = 5$ and $N = 10$, we conducted simulations with $\beta = 0.01, 0.001, 0.0005$ and $0.0001\,\mathrm{ms}^{-1}$ (figures 4.12B and 4.12C). Again, at $\beta = 0.01\,\mathrm{ms}^{-1}$ the intermittent phase was never reached. The plots of $1/\tau$ still fail to reproduce the experimentally recorded curved lines for the higher frequencies. Nevertheless, for $N = 10$ and $\beta = 0.001\,\mathrm{ms}^{-1}$, hints of the right shape are visible. The values of the reciprocals are still off by an order of magnitude. It is also to be seen that the steady-state spike-rates depend sensitively on the choice of β and on the length of the chain (comparing figures 4.12B and 4.12C). For $N = 50$ and $N = 100$ we performed simulations for $\beta = 0.1, 0.01$ and $0.001\,\mathrm{ms}^{-1}$ (figures 4.12D and 4.12E). We did not use lower values of β because already at $\beta = 0.001\,\mathrm{ms}^{-1}$ the steady-state values of the spike-rate are much lower than in the experiments. As can be seen, from $N = 50$ onwards the plots of the reciprocals $1/\tau$ versus the stimulation rate start to exhibit the right shape. Nevertheless the correct order of magnitude is only obtained for $\beta = 0.001\,\mathrm{ms}^{-1}$. The steady-state spike-rate is shown to depend again sensitively on the length of the chain. Spike rates that agree quantitatively with the experiments are thus expected in the range $N = 50$ to $N = 100$.

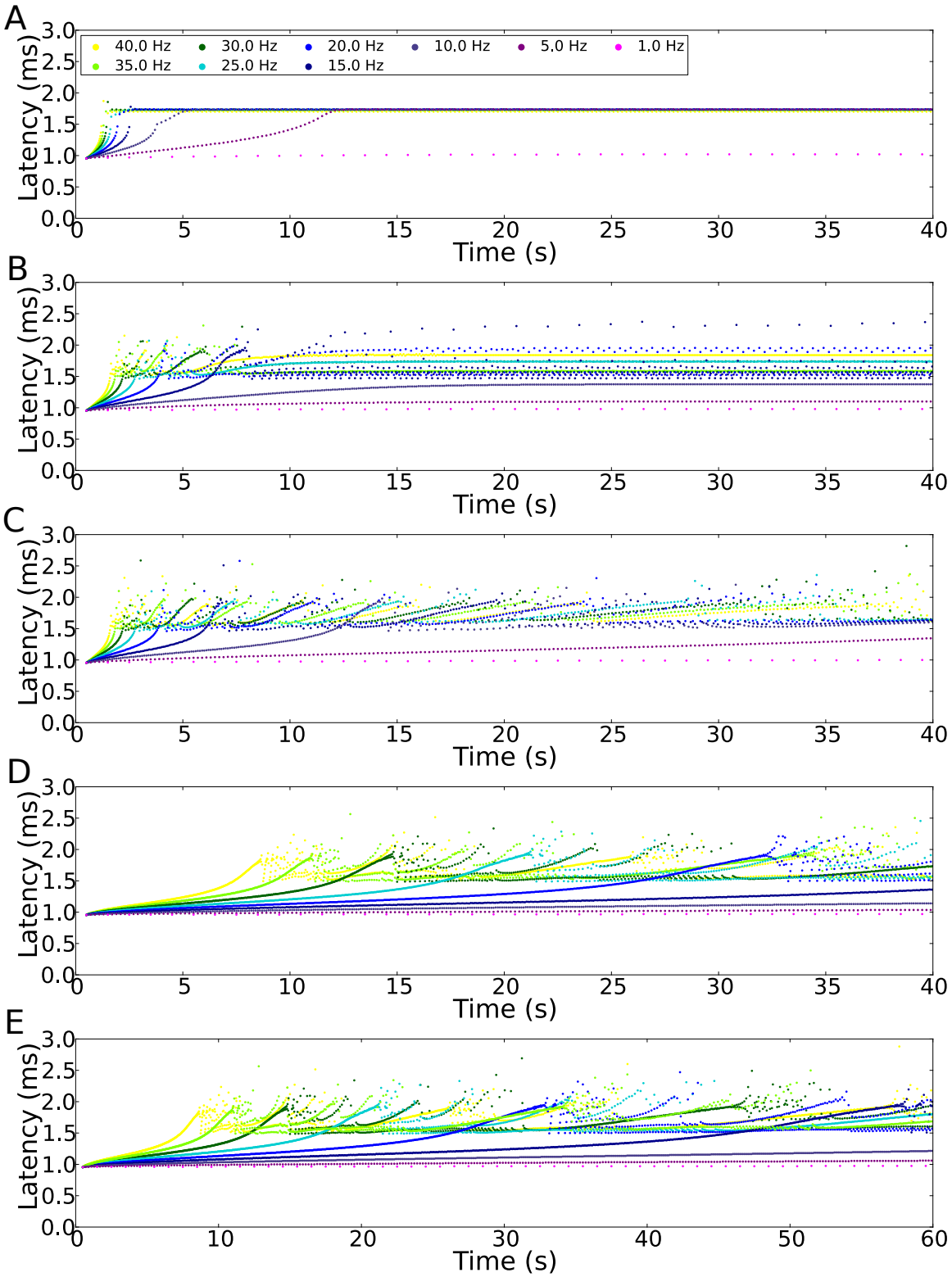

Figure 4.11: Latencies as a function of time during the first 40s of stimulation, at rates of $1, 5, 10, 15, 20, 25, 30, 35$ and 40Hz. (**A**) For a chain length of $N = 1$ and rate $\beta = 0.0001\text{ms}^{-1}$, (**B**) a chain length of $N = 5$ and rate $\beta = 0.001\text{ms}^{-1}$, (**C**) a chain length of $N = 10$ and rate $\beta = 0.001\text{ms}^{-1}$ (**D**) a chain length of $N = 50$ and rate $\beta = 0.01\text{ms}^{-1}$ and (**E**) a chain length of $N = 100$ and rate $\beta = 0.01\text{ms}^{-1}$.

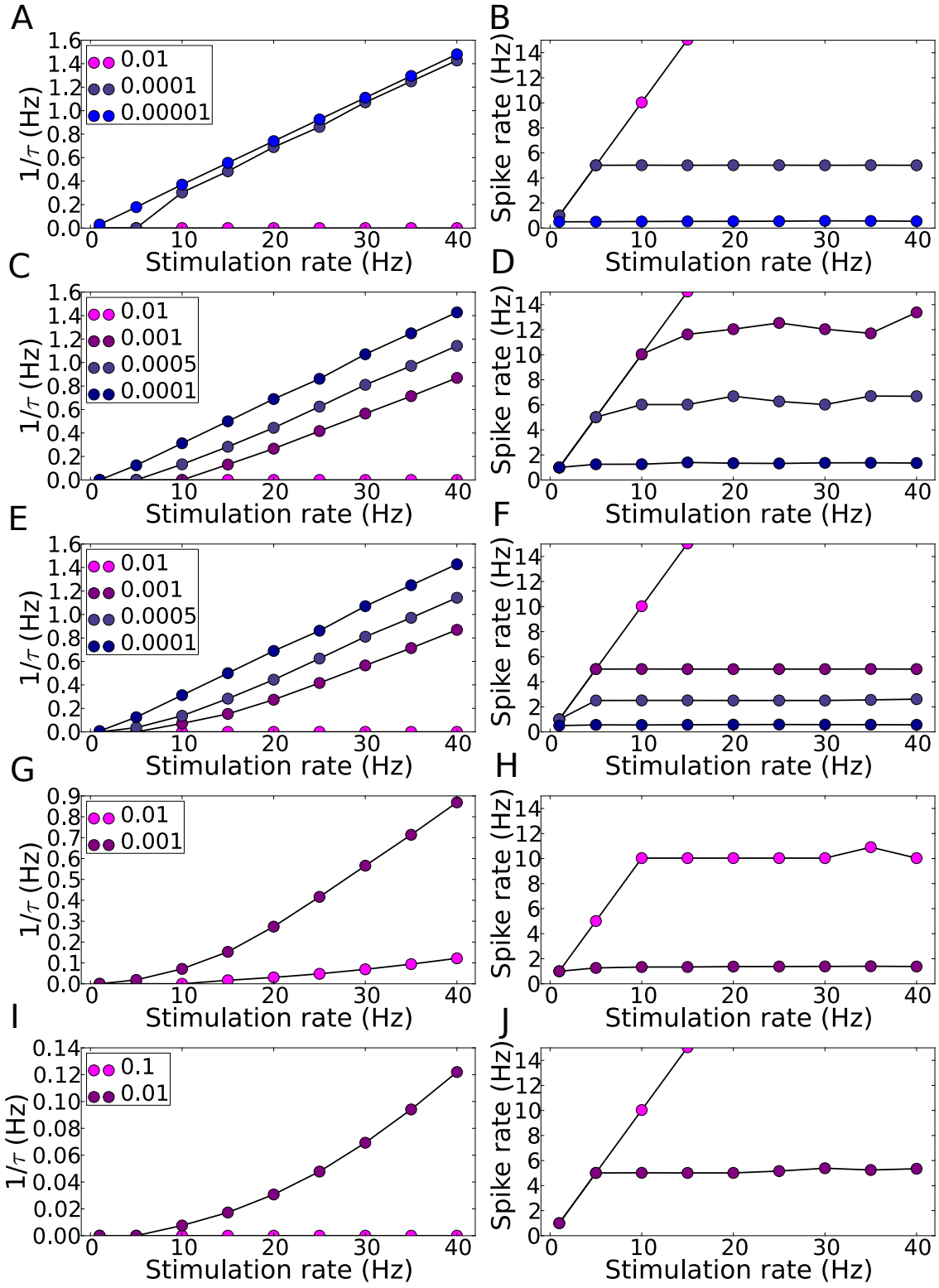

Figure 4.12: Reciprocals of the durations of the transient phases (column 1) and the steady-state spike-rates (column 2) for stimulation rates $1, 5, 10, 15, 20, 25, 30, 35$ and $40\,\mathrm{Hz}$. The values of β are indicated in the legends. Chain lengths of (**A**),(**B**) $N = 1$, (**C**),(**D**) $N = 5$, (**E**),(**F**) $N = 10$, (**G**),(**H**) $N = 50$ and (**I**),(**J**) $N = 100$.

4.4.3 Entry rate amplitude

In the previous paragraph we concluded that the reciprocals of the durations of the transient phases τ were an order of magnitude to large for the shorter chain lengths $N = 1, 5$ and 10. These magnitudes can be changed however by changing the fraction of channels that inactivates at every spike. Therefore we rescale the step-function inactivation rate by an amplitude factor h_α:

$$\alpha(V) = \begin{cases} 0 \text{ ms}^{-1} & \text{if } V < -20 \text{ mV} \\ 0.15 h_\alpha \text{ ms}^{-1} & \text{if } V > -20 \text{ mV}. \end{cases} \tag{4.26}$$

For each chain length N we thus have two relevant parameters: h_α controls the amount of channels that inactivate at every spike and β controls the speed of their return to the active state. We now want to know whether it is possible for each chain length N to obtain values for the reciprocals of the transient times $1/\tau$ and for the steady state spike rates f_{eq} that agree quantitatively with the experimental results. Since for none of the reasonable parameter values the model reached intermittency at 1 Hz, so that $1/\tau = 0$ at that stimulation rate, and since $1/\tau$ rises monotonically as a function of the stimulation rate, we argue that if we obtain the correct value of $1/\tau$ at a stimulation rate of 40 Hz, $1/\tau$ will also lie within the correct range for all other values of the stimulation rate in between 1 and 40 Hz. Thus we scan the relevant parameter space (h_α, β) and look where both $1/\tau$ and f_{eq} have the observed values, that is $1/\tau \simeq 0.16$ Hz and $f_{\text{eq}} \simeq 8$ Hz.

The results of these simulations for $N = 1, 5, 10, 50$ and 100 are shown respectively in rows A,B,C,D and E of figure 4.13. We plotted the full surface of $1/\tau$ and of f_{eq} as a function of h_α and β, and we also indicated where these surfaces intersected with the planes $1/\tau = 0.16$ Hz and $f_{\text{eq}} \simeq 8$ Hz. In the third panel of every row we plotted these lines in the parameter space. The combinations for which these lines intersect or lie close together give values for both $1/\tau$ and f_{eq} that agree quantitatively with the experiments. As can be seen, for any chain length N this model is tunable to produce observables that lie close to the experimental values. With increasing chain lengths however, the surfaces become much smoother and these lines move closer together, meaning that there is a much larger parameter set that fits the experiments. This observation and the curved shapes in the $1/\tau$ plots of figure 4.12 for the larger chain lengths N, lead us to prefer them over the shorter chain lengths.

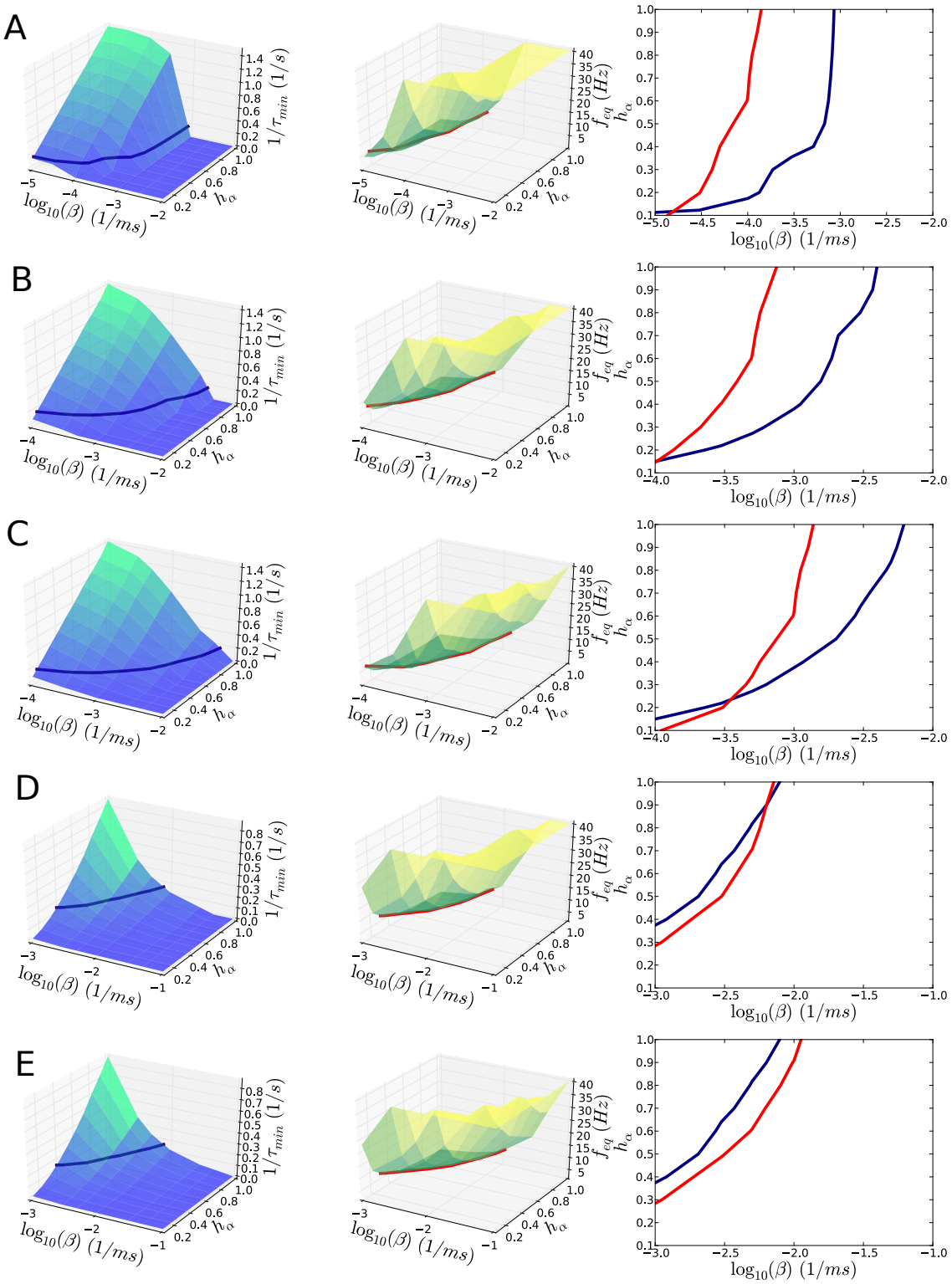

Figure 4.13: Surfaces of reciprocals of the durations of the transient phase $1/\tau$ (first column) and of the steady state spike rates f_{eq} (second column) as a function of h_α and β and at a stimulation rate of 40 Hz. The fat lines indicate the experimentally observed values (blue: $1/\tau$ and red: f_{eq}). These lines are plotted again in the third column. Figures (**A**), (**B**), (**C**), (**D**) and (**E**) show chain lengths of respectively $1, 5, 10, 50$ and 100.

Chapter 5

Stochastic neuron models and scale-invariant excitability

5.1 Noisy algorithms

In the previous chapter we introduced a deterministic neuron model that exhibits slow dynamics that last over time-scales of seconds to minutes. We found that this model could already account for a great deal of the experimentally observed effects. Nevertheless it always evolved to some steady state, where the spike rate was found to be regular. Hence no scale-invariant statistics could be measured.

In chapter 2 however, we noted that the ion channels in the nerve membrane flickered randomly between open and closed states, with overall kinetic rates that are given by the schemes in figure 2.2B for the potassium channels and figure 2.2C for the sodium and A-channels. Many algorithms have been proposed to model the noise that emerges from this random behaviour, either in a microscopic way, by modelling the individual transitions of ion channels through Markov chain Monte Carlo methods (MCMC) ([18], [7]), or in an effective way, by approximating this noise by Langevin dynamics (for instance [19],[20],[21],[22]). Thus, these algorithms can be divided in two categories: the first category explicitly models the microscopic state of the system whereas in the second category continuous approximations are used. In the microscopic case the number of channels in all states of the kinetic scheme is tracked, and transitions between different configurations of the system are discrete. If the scheme contains M states, we define the vector $\mathbf{X} = (X_1, \ldots, X_M)$ whose i-th component X_i denotes the number of channels in state i of the scheme and refer to $\mathbf{X}$ as the microscopic configuration of the system. The second category of algorithms defines a continuous vector $\mathbf{x} = (x_1, \ldots, x_M) = (\frac{X_1}{N}, \ldots, \frac{X_M}{N})$ and

then tries to approximate the noise resulting from the microscopic algorithms by using continuous stochastic processes. We shall refer to $\mathbf{x}$ as the macroscopic configuration of the system.

The Markovian assumption implies that ion channels that evolve through a kinetic scheme have no memory of their previous states. This can be formalized as (see for instance [23]):

$$\dot{P}(\mathbf{X}, t) = \int [W(\mathbf{X}|\mathbf{X}')P(\mathbf{X}', t) - W(\mathbf{X}'|\mathbf{X})P(\mathbf{X}, t)]\mathrm{d}\mathbf{X}', \tag{5.1}$$

where $W(\mathbf{X}|\mathbf{X}')$ denotes the probability to go from state $\mathbf{X}'$ to state $\mathbf{X}$. Thus the probability $P(\mathbf{X}, t + \mathrm{d}t)$ to have a certain vector $\mathbf{X}$ at time $t + \mathrm{d}t$ is only dependent on the probability $P(\mathbf{X}, t)$ to have a certain vector $\mathbf{X}$ at time t. Equation (5.1) is referred to as the master equation.

5.1.1 Microscopic MCMC

Of course, we are not interested in the full evolution of $P(\mathbf{X}, t)$, but only in the evolution of realisations $\mathbf{X}(t)$. It is possible to take advantage of the fact that $\mathbf{X}(t)$ is memoryless to develop simulation algorithms: one such example is given by Gillespie's algorithm [18], in which the time-interval until the next change in the system is drawn from an exponential distribution. Thus the time-step in this algorithm is not constant, which makes it tricky to implement in the NEURON simulating environment. Therefore, we used a simpler algorithm that implements the Markov assumption by stating that the probability for a channel to move in a small time-interval $[t, t + \mathrm{d}t]$ is only dependent on the current state of the channel.

The canonical form of this algorithm is as follows: suppose that a state X_i has K transition rates ρ_j, with $j = 1, \ldots, K$, that go from state X_i to another state in the scheme, and that the simulation time step is $\mathrm{d}t$. The probability that a channel will move in that time-step to another state is then distributed according to an exponential distribution

$$P_{i\to \text{ any } j} \propto 1 - \exp\left(-\sum_j \rho_j \mathrm{d}t\right) \tag{5.2}$$

and trivially

$$P_{\text{no move}} \propto \exp\left(-\sum_j \rho_j \mathrm{d}t\right) \tag{5.3}$$

Thus for every channel in X_i a uniformly distributed random number r_1 between 0 and 1 is drawn. If $r_1 > P_{i\to \text{ any } j}$ the channel doesn't change state and if $r_1 < P_{i\to \text{ any } j}$ the channel moves. If the channel moves, a second uniformly distributed random number r_2 is drawn to decide to which state the channel moves. If

$$\frac{\sum_{k=1}^{j-1}\rho_k \mathrm{d}t}{\sum_{k=1}^{K}\rho_k \mathrm{d}t} < r_2 < \frac{\sum_{k=1}^{j}\rho_k \mathrm{d}t}{\sum_{k=1}^{K}\rho_k \mathrm{d}t}, \tag{5.4}$$

the channels moves to state j. At every time step, this algorithm runs over all channels in every state X_i and decides whether and to where they will move. After this time-step, first the fraction of open channels, then the voltage and finally the voltage-dependent kinetic rates are updated. Then the whole process starts anew.

In the case of a small time step $\mathrm{d}t$, so that $\rho_j \mathrm{d}t \ll 1$ for all j, this algorithm simplifies considerably. Equations (5.5) and (5.6) then linearise to

$$P_{i\to \text{ any } j} \propto \sum_{j=1}^{K} \rho_j \mathrm{d}t \tag{5.5}$$

and

$$P_{\text{no move}} \propto 1 - \sum_{j=1}^{K} \rho_j \mathrm{d}t. \tag{5.6}$$

Since the probability to choose to which X_j a channel moves is directly proportional to $\rho_j \mathrm{d}t$, we may draw only one random number r, do nothing if $r > \sum_{j=1}^{K}\rho_j \mathrm{d}t$ and move the channel to state j if $\sum_{k=1}^{j-1}\rho_k \mathrm{d}t < r < \sum_{k=1}^{j}\rho_k \mathrm{d}t$, as depicted in figure 5.1. We use the MCMC algorithm in this form throughout all our stochastic simulations.

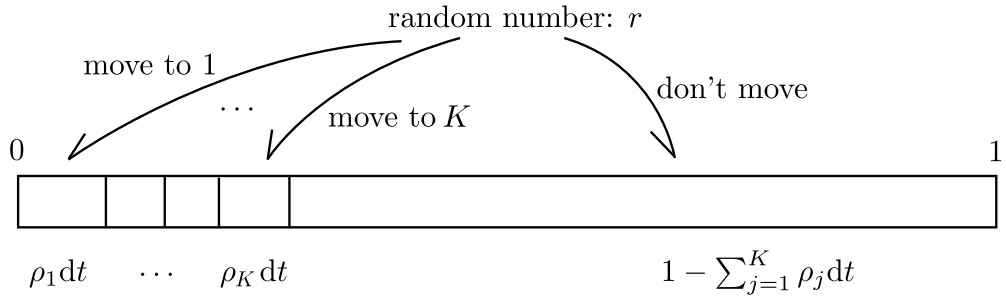

Figure 5.1: Schematic representation of the MCMC algorithm.

Note that in this form the algorithm simply draws random numbers from a multinomial distribution. The numbers of channels $N_1, \ldots, N_K$ that move from X_i to $X_1, \ldots, X_K$ in

the time-interval $[t, t + \mathrm{d}t]$, are then distributed as

$$p(N_1, \ldots, N_k) \propto (\rho_1 \mathrm{d}t)^{N_1} \ldots (\rho_K \mathrm{d}t)^{N_K} (1 - \sum_{k=1}^{K} \rho_k \mathrm{d}t)^{1-\sum_{k=1}^{K} N_k} \tag{5.7}$$

with a mean

$$\mu = (N\rho_1 \mathrm{d}t, \ldots, N\rho_K \mathrm{d}t) \tag{5.8}$$

and a covariance matrix

$$\mathrm{cov} = \begin{pmatrix} N\rho_1 \mathrm{d}t(1 - \rho_1 \mathrm{d}t) & -N\rho_1 \mathrm{d}t\rho_2 \mathrm{d}t & \cdots & -N\rho_1 \mathrm{d}t\rho_K \mathrm{d}t \\ -N\rho_2 \mathrm{d}t\rho_1 \mathrm{d}t & N\rho_2 \mathrm{d}t(1 - \rho_2 \mathrm{d}t) & \cdots & -N\rho_2 \mathrm{d}t\rho_K \mathrm{d}t \\ \vdots & \vdots & \ddots & \vdots \\ -N\rho_K \mathrm{d}t\rho_1 \mathrm{d}t & -N\rho_K \mathrm{d}t\rho_2 \mathrm{d}t & \cdots & N\rho_K \mathrm{d}t(1 - \rho_K \mathrm{d}t) \end{pmatrix} \tag{5.9}$$

5.1.2 System-size expansion

As noted in chapter 2, taking the deterministic limit ($N \to \infty$) of the master equation (5.1) results in the following linear system of equations

$$\frac{\mathrm{d}\mathbf{x}}{\mathrm{d}t} = \mathbb{W}\mathbf{x}. \tag{5.10}$$

Using a technique previously developed in physics and brought to neuroscience by [19], known as the system-size expansion [23], it is possible to extend equation (5.10) to add the fluctuations

$$\frac{\mathrm{d}\mathbf{x}}{\mathrm{d}t} = \mathbb{W}\mathbf{x} + \mathbb{L}\xi. \tag{5.11}$$

Here $\xi = (\xi_1, \ldots, \xi_M)$ is a vector of normally distributed random numbers and $\mathbb{L}$ is the matrix square root of the diffusion matrix $\mathbb{D}$.

Equation (5.11) is the Langevin equation that can be derived from the Fokker-Planck equation associated with the master equation (5.1). This Fokker-Planck equation makes use of the diffusion matrix $\mathbb{D}$, defined by

$$(\mathbb{D}(\mathbf{x}))_{kl} = \frac{1}{N^2} \int r_k r_l \Omega(\mathbf{x}, \mathbf{r}) \mathrm{d}\mathbf{r} \tag{5.12}$$

where $\Omega(\mathbf{x}, \mathbf{r}) = W(\mathbf{X}, \mathbf{r})$, with $W(\mathbf{X}, \mathbf{r}) = W(\mathbf{X}|\mathbf{X}')$ and $\mathbf{r} = \mathbf{X} - \mathbf{X}'$. At every time-step in the algorithm, this diffusion matrix is recalculated and its matrix square root is computed. Because of this second step, the algorithm is quite inefficient.

Nevertheless this algorithm was shown to perform well, approximating accurately a number of statistical measures of the microscopic algorithm [20], [21]. However, the auto-correlation functions

$$\Phi_{x_i}(\Delta, t) = \mathrm{E}(x_i(t+\Delta)x_i(t)) - \mathrm{E}(x_i(t))^2 \tag{5.13}$$

obtained by this algorithm were never compared with the autocorrelation functions of the microscopic MCMC-algorithm. Quite often, the autocorrelations obtained by Langevin algorithms are decaying much faster than the ones obtained by the microscopic algorithm [24]. Since we want to model the effects of long effective time-scales, we can not take the risk of introducing errors in the autocorrelations. Therefore we do not use this algorithm. We nevertheless show in appendix A how to compute the diffusion matrix for the linear inactive chain we use.

5.1.3 Effective noise using the auto-correlation function

It was shown that the autocorrelation function (5.13) can be used for some kinetic schemes to model the channel noise in a very efficient manner [22]. By realizing that only the open state in a given kinetic scheme is needed in the charge-balance equation, it can hypothesised that adding the channel noise only to this state in the charge balance equation, and evolving the kinetic scheme deterministically, will yield the same results.

Suppose that a population of channels produces the following current

$$I = \overline{g} o(V)(V - E) \tag{5.14}$$

and that o is the k-th state in a kinetic scheme specified by the vector $\mathbf{x}$ with M components (thus $o = x_k$). Suppose furthermore that the evolution of this scheme is specified by the transition matrix $\mathbb{W}$. The approximation of [22] is then to add a phenomenological combination of stochastic processes ξ_j $(j = 1, \ldots, M)$ to equation (5.14) in the following way

$$I = \overline{g} \left(o(V) + \sum_j \xi_j \right) (V - E)\,, \tag{5.15}$$

so that this sum has exactly the same autocorrelation function $\Phi_{x_k=o}$ as the one obtained by the microscopic algorithms.

This autocorrelation function can be computed analytically [22], [25] and reads for Markov chains in their equilibrium state

$$\Phi_{x_k=o}(\Delta) = \frac{1}{N} o_\infty \left[\mathbf{c} \exp(-\mathbb{W}|\Delta|)\mathbf{c}^T - o_\infty \right] \tag{5.16}$$

where o_∞ is the equilibrium value of o and $\mathbf{c} = (0, \ldots, 0, 1, 0, \ldots, 0)$ is a vector so that $o = \mathbf{cx}$. It is to be seen that this expression reduces to a combination of exponentials

$$\Phi_{x_k=o}(\Delta) = \sum_j \sigma_j e^{-\lambda_j t}, \tag{5.17}$$

where the λ_j's are the eigenvalues of $\mathbb{W}$. It can be shown that a linear combination (as in equation (5.15)) of Ornstein-Uhlenbeck processes

$$\frac{\mathrm{d}\xi_j}{\mathrm{d}t}(t) = \frac{1}{\lambda_j}\left(-\xi_j(t) + \sigma_j\sqrt{\frac{2}{\lambda_j}}\nu_j(t)\right), \tag{5.18}$$

where the $\nu_j(t)$'s are Gaussian delta-correlated processes with zero mean, has the same autocorrelation function as the Markov scheme.

Thus the effective noise approximation of [22] consists of recalculating the autocorrelation function (5.16) at every time-step, advancing the OU processes (5.18), advancing the vector $\mathbf{x}$ deterministically, according to (5.10), advancing the voltage according to the charge-balance equation and finally updating the voltage-dependent transition rates.

This approximation is very efficient if the kinetic schemes in use can be mapped onto two-state subunit schemes, because then expression (5.16) for the autocorrelation function simplifies considerably. This is impossible for the scheme 4.2, and thus this approximation becomes much more complicated. Moreover, this algorithm was only shown to work for those cases where the channels distribution $\mathbf{x}$ is not to far from the equilibrium channel distribution $\mathbf{x}_\infty$ of the kinetic scheme. Because of the slow relaxation times this is never the case for the sodium-scheme in figure 4.2 under repeated spiking, so using this algorithm might again introduce errors in the results. Therefore we refrain from using it in this work.

5.2 Insertion and removal of ion channels

In the previous paragraph we have discussed the traditional form of channel noise, resulting from the intrinsic stochasticity of the chemical reactions that channels in the cell membrane undergo. In some cases, and in particular in kinetic schemes as 4.2, channel noise might contribute to the observed long correlations in the excitability.

During the course of this work however, we noted that another form of channel noise might contribute to this effect. A clue is provided in [26], where a model by Gerstein and Mandelbrot is discussed. As they note, if an event happens every time a variable is above a certain threshold, and because of this event the variable jumps below this threshold, where it performs a (bounded) random walk, the resulting distribution of inter-event intervals

is a power law. Since we have shown that in the deterministic version of our model the variable a jumps below the firing threshold a_{thr} every time a spike happens during the intermittent phase (figure 4.4), we hypothesize that if in some way a performed a random walk, we would find the experimentally observed properties of the excitability.

This noise is however fundamentally different from the noise that results from a Markov scheme. We now provide an intuitive argument for this (where we basically rederive the system-size approximation for a two-state scheme).

Consider a two-state scheme, as in figure 2.2, and suppose that this scheme contains N channels. According to the kinetic rates α and β (where we dropped the index i), the numbers of channels at equilibrium in each state N^o_∞ and N^c_∞ follow from

$$N^o_\infty \beta \mathrm{d}t = N^c_\infty \alpha \mathrm{d}t \quad \text{and} \quad N^o_\infty + N^c_\infty = N. \tag{5.19}$$

Since in paragraph 5.1.1 we discussed that deciding how many channels will move from one state to another is equivalent to drawing from a multinomial distribution (in this case a binomial distribution, since there are only 2 possibilities: moving to the other state or staying in the present state). Thus, at equilibrium, the expected number of channels that will move in a small time-interval $[t, t+\mathrm{d}t]$ from o to c is given by $\mu(N_{o\to c}) = N^o_\infty \beta \mathrm{d}t$ and the variance on this number is $\mathrm{var}(N_{o\to c}) = N^o_\infty \beta \mathrm{d}t(1-\beta \mathrm{d}t)$. For the transition from c to o we have $\mu(N_{c\to o}) = N^c_\infty \alpha \mathrm{d}t$ and the variance on this number is $\mathrm{var}(N_{c\to o}) = N^c_\infty \alpha \mathrm{d}t(1-\alpha \mathrm{d}t)$. If now there is a deviation ϵ from the equilibrium channel numbers $N^o_\infty \to N^o_\infty + \epsilon$ and $N^c_\infty \to N^c_\infty - \epsilon$, we have

$$\mu(N_{o\to c}) = (N^o_\infty + \epsilon)\beta \mathrm{d}t \qquad \text{and} \quad \mathrm{var}(N_{o\to c}) = (N^o_\infty + \epsilon)\beta \mathrm{d}t(1-\beta \mathrm{d}t) \tag{5.20}$$

$$\mu(N_{c\to a}) = (N^c_\infty - \epsilon)\alpha \mathrm{d}t \qquad \text{and} \quad \mathrm{var}(N_{c\to o}) = (N^c_\infty - \epsilon)\alpha \mathrm{d}t(1-\alpha \mathrm{d}t). \tag{5.21}$$

Going to the continuous limit ($N \to \infty$), both of these binomial distributions become Gaussians and we have:

$$P(N_{o\to c}) \quad \sim \mathcal{N}\left((N^o_\infty + \epsilon)\beta \mathrm{d}t, (N^o_\infty + \epsilon)\beta \mathrm{d}t(1-\beta \mathrm{d}t)\right) \tag{5.22}$$

$$P(N_{c\to o}) \quad \sim \mathcal{N}\left((N^c_\infty - \epsilon)\alpha \mathrm{d}t, (N^c_\infty - \epsilon)\alpha \mathrm{d}t(1-\alpha \mathrm{d}t)\right). \tag{5.23}$$

Since we are interested in the probability that the amount of channels in o changes by a number ΔN in the time-interval $[t, t+\mathrm{d}t]$, we combine (5.22) and (5.23)

$$P(\Delta N) = P(N_{c\to o}) - P(N_{o\to c}) \sim \mathcal{N}(\mu, \sigma^2), \quad \text{with} \tag{5.24}$$

$$\mu = (N^o_\infty \beta - N^c_\infty \alpha)\mathrm{d}t - \epsilon(\alpha+\beta)\mathrm{d}t \quad \text{and} \tag{5.25}$$

$$\sigma^2 = (N^o_\infty \beta \mathrm{d}t(1-\beta \mathrm{d}t) + N^c_\infty \alpha \mathrm{d}t(1-\alpha \mathrm{d}t))\mathrm{d}t + \epsilon(\beta \mathrm{d}t(1-\beta \mathrm{d}t) + \alpha \mathrm{d}t(1-\alpha \mathrm{d}t)). \tag{5.26}$$

Since $\mathrm{d}t$ is small, we ignore all terms of order $\mathrm{d}t^2$. Using the balance condition (5.19), we find

$$P(\Delta N) \sim \mathcal{N}(-\epsilon(\alpha+\beta)\mathrm{d}t, 2N_\infty^o\beta\mathrm{d}t + \epsilon(\alpha+\beta)\mathrm{d}t). \tag{5.27}$$

Going to the continuous variables, this gives

$$P(\Delta o) = P\left(\frac{\Delta N}{N}\right) \sim \exp\left(\frac{N^2(\Delta o + \frac{\epsilon}{N}(\alpha+\beta)\mathrm{d}t)^2}{4N_\infty^o\beta\mathrm{d}t + \epsilon(\alpha+\beta)\mathrm{d}t}\right). \tag{5.28}$$

Thus we find

$$P(\Delta o) \sim \mathcal{N}\left(\frac{-\epsilon}{N}(\alpha+\beta)\mathrm{d}t, 2\frac{o_\infty}{N}\beta\mathrm{d}t\right), \tag{5.29}$$

where $o_\infty = N_\infty^o/N$ and where we ignored the term in the variance proportional to ϵ/N^2, since $\epsilon \ll N_\infty^o$ under all normal circumstances. Identifying ϵ/N with $o - o_\infty$, we find indeed that (5.29) defines an Ornstein-Uhlenbeck process for o

$$\frac{\mathrm{d}o}{\mathrm{d}t}(t) = (\alpha+\beta)(o(t) - o_\infty) + \sqrt{\frac{2}{N}o_\infty\beta}\nu(t), \tag{5.30}$$

where $\nu(t)$ is a delta-correlated zero-mean Gaussian noise process. We see that the ratio of drift over variance (μ/σ^2, where μ and σ^2 follow from equation (5.29)) rises approximately linearly in ϵ. Such a relation gives rise to an Ornstein-Uhlenbeck process, that has no self-similar properties. Moreover, it was our experience that such processes, derived from Markov schemes, always stay fairly close to their equilibrium values. Of course, we could extend this kinetic scheme to include many time-scales, so that by the approximation explained in 5.1.3 many Ornstein-Uhlenbeck processes need to be introduced. It was however our experience that finding a scheme that produces these processes with just the right parameters (determined from (5.16)) is very tricky. Moreover, we did not find any situation where noise resulting from such schemes caused the channel numbers to deviate enough from their equilibrium values to cause significant effects on the neuronal excitability.

This leads us to believe that it might be interesting to think about other forms of noise, that don't have the property $\mu/\sigma^2 \sim \epsilon$. If for instance we assume that the noise contributions don't follow Ornstein-Uhlenbeck processes, but that they look more like Wiener processes over a significant interval $-\delta < \epsilon < \delta$, so that $\mu/\sigma^2 \sim 0 \ll \epsilon$ over this interval. It is known that the Wiener process is self-similar, hence it is not unlikely to argue that such a process could cause the scale-invariant excitability.

Thus we asked whether channel noise contributions in neurons can display the properties of a Wiener process (continuous variables, macroscopic configuration) or a random walk

(discrete variables, microscopic configuration) rather than the typical Ornstein-Uhlenbeck relaxation processes associated with the noise that results from Markov schemes. At first this seems impossible, as modelling chemical reactions through Markov schemes has proven its merits numerous times and is the most commonly accepted technique. Nevertheless we note that the ion channels do not stay in the nerve membrane forever, nor were they there since the creation of the cell. They are synthesized from proteins inside the cell and then diffuse to the cell membrane, where they let ions pass through and after some time they are removed from the cell membrane. While both the evolution of ion channels in the nerve membrane and their synthesis from proteins inside the cell may be modelled with Markov Chains, we hypothesise that the intermediate step, their diffusion to the cell membrane, might cause a noise contribution that looks more like a Wiener process than an Ornstein-Uhlenbeck process.

It should be noted however that very little is known about what governs the insertion and removal of ion channels, and very complex processes and feedback mechanisms may be at work to prevent the ion channel numbers from dropping too low or rising too high. Thus, any complicated model that tries to model these feedback effects explicitly would be nothing more than a mere speculation and therefore we keep our assumptions as simple as possible. We assume that the rate of removal of ion channels from the nerve membrane is constant, so that the expected number of removals per unit of time μ_r is a fixed number. We also assume that the expected number of arrivals μ_a of ion channels in the nerve membrane is constant. We furthermore assume that there are feedback mechanisms inside the neuron that prevent the number of channels from rising too high or dropping too low. Since we do not know anything about the nature of these mechanisms, we code them in our algorithm doubling μ_r if the amount of ion channels is above a certain upper bound $N_{\max}$ and by doubling μ_a if the number of channels is below a lower bound $N_{\min}$. We sketch schematically the effect of this procedure on μ/σ^2 in figure 5.2. We also sketch μ/σ^2 for the Markov chain and for what could be a biophysical function that has the right properties to cause the scale-invariant excitability.

We translate the principles explained above into an algorithm, by assuming that the actual numbers of ion channels removed and inserted into the nerve-membrane in a small time-interval $[t, t + \mathrm{d}t]$ are Poisson-distributed

$$P(N_r|\mu_r, \mathrm{d}t) \sim \mathrm{Poisson}(N_r; \mu_r \mathrm{d}t) = \frac{(\mu_r \mathrm{d}t)^{N_r} e^{-\mu_r \mathrm{d}t}}{N_r!} \tag{5.31}$$

$$P(N_a|\mu_a, \mathrm{d}t) \sim \mathrm{Poisson}(N_a; \mu_a \mathrm{d}t) = \frac{(\mu_a \mathrm{d}t)^{N_a} e^{-\mu_a \mathrm{d}t}}{N_a!} \tag{5.32}$$

Thus, at every time-step, we draw two Poisson-distributed random numbers that represent the number of channels that are to be removed (N_r) and the number of channels that are

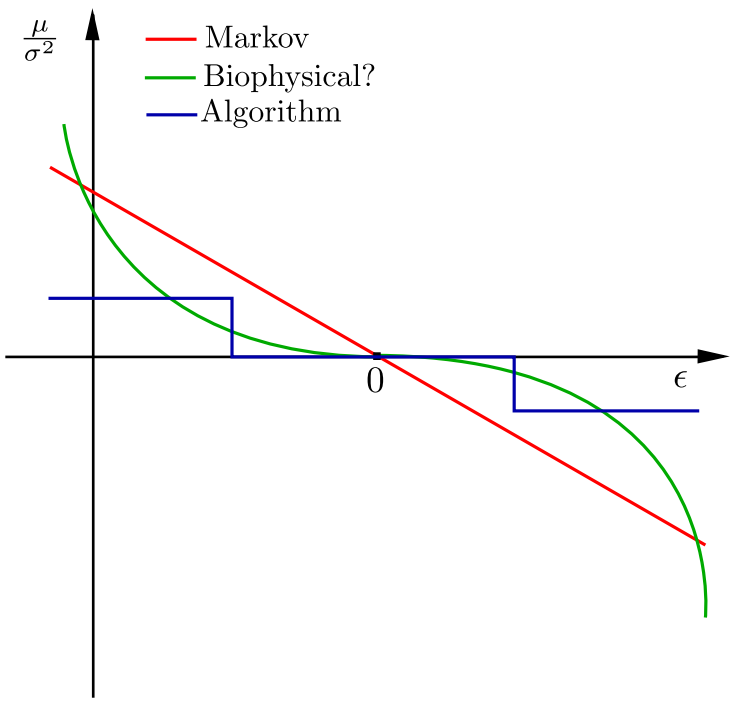

Figure 5.2: A cartoon of the drift in the noise as a function of the deviation from equilibrium.

to be added (N_a). Then, the states of the kinetic schemes from which the channels are removed and added, are chosen according to the number of channels in that state. This assumption is reasonable for the channels that are removed, but might be questionable for channels that are added. Therefore we also compare this algorithm with an algorithm that adds channels to and removes channels from the same state. For this to have an effect, a state needs to be chosen from the active part of the scheme, so that the effective conductance is indeed modified. As the dynamics of removel and insertion are much slower than the fast dynamics of the spike, the active state to which they are added does not matter. We choose m_0h_0.

5.3 Results

Given the discussion in the previous paragraphs, we arrive at three hypothesises to test:

1. The observed scale invariant excitability is caused only by traditional channel noise

that results from the long correlation times induced by the chain of inactive states (kinetic scheme in figure 4.2).

2. Traditional channel noise is not important, and the scale-invariant excitability is caused only by the newly proposed form of noise that might arise from the insertion and removal of ion channels

3. Scale invariant excitability is caused by both phenomena.

In the following we will show results for all three hypothesises. We start however by a few considerations about the probability to have a spike, as this will turn out to be important for understanding the differences between the models.

5.3.1 Probability to have a spike

We start by considering the probability P_s that a spike is fired in response to a fixed amplitude current pulse. In the deterministic case the situation was simple, as there was a clear jump in the spike amplitude at a certain value of a (figure 2.5). In the stochastic case however, the spike amplitude is a random variable. Thus it is necessary to check whether there is a clear boundary between spikes and failures. Figure 5.3 shows a histogram of the deviation from the equilibrium potential after a stimulation recorded from model neurons in the intermittent phase. This distribution clearly has two parts and our threshold crossing protocol (with a threshold at $-20\,\mathrm{mV}$, corresponding to a deviation of $50\,\mathrm{mV}$ above the equilibrium potential) indeed classifies events in the lower part of the distributions a failures and events in the higher part as spikes.

Furthermore, the probability P_s is a function of a, that is fundamentally different for the deterministic case (representing the situation where the channel noise is not important, figure 2.5) and for the stochastic case (representing the situation where channel noise is important, figure 5.4). In the deterministic case, there is a sharp threshold between spikes and failures at a given value of a, whereas in the stochastic case, spikes and failures happen randomly, with a probability that is only slightly dependent on a.

As a consequence, there can be significant differences in the distributions of the length of sequences of consecutive spikes and consecutive failures. In the deterministic case, there is the sub-threshold random walk behaviour, that leads us to expect a power law distribution of the sequence lengths of failures. In the stochastic case however, spikes and failures happen in a random fashion, with probabilities that are only slightly correlated by a. Thus we expect exponential distributions for both the sequences of spikes and failures.

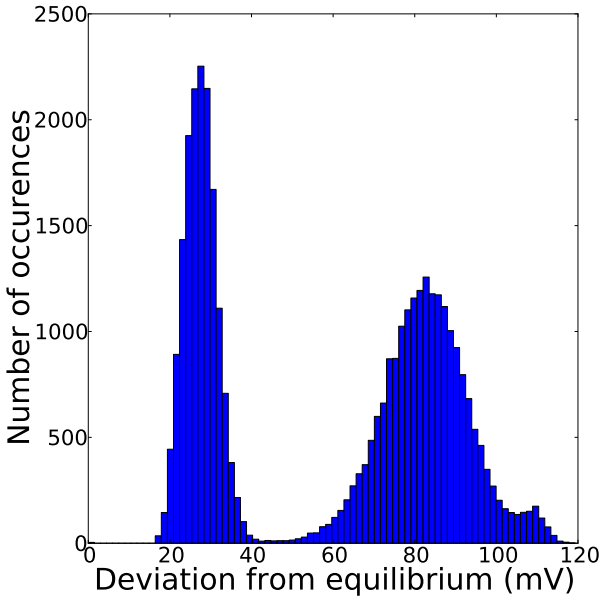

Figure 5.3: Histogram of the heights of the deviations from the equilibrium potential in response to a fixed amplitude current pulse.

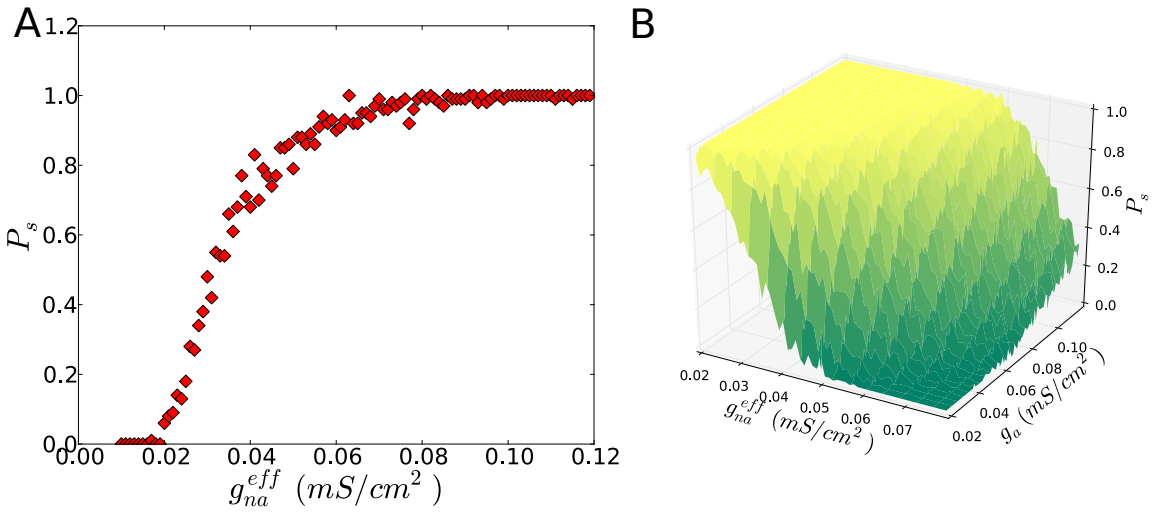

Figure 5.4: The probability to have a spike in the stochastic Connor-Stevens model at fixed values of a, and thus of g^{eff}, for a channel number $N_c = 1507$. In (**A**) only the maximal conductance of sodium is varied and in (**B**) both the sodium and potassium maximal conductance are varied. For each point in the phase-space we conducted 100 trials.

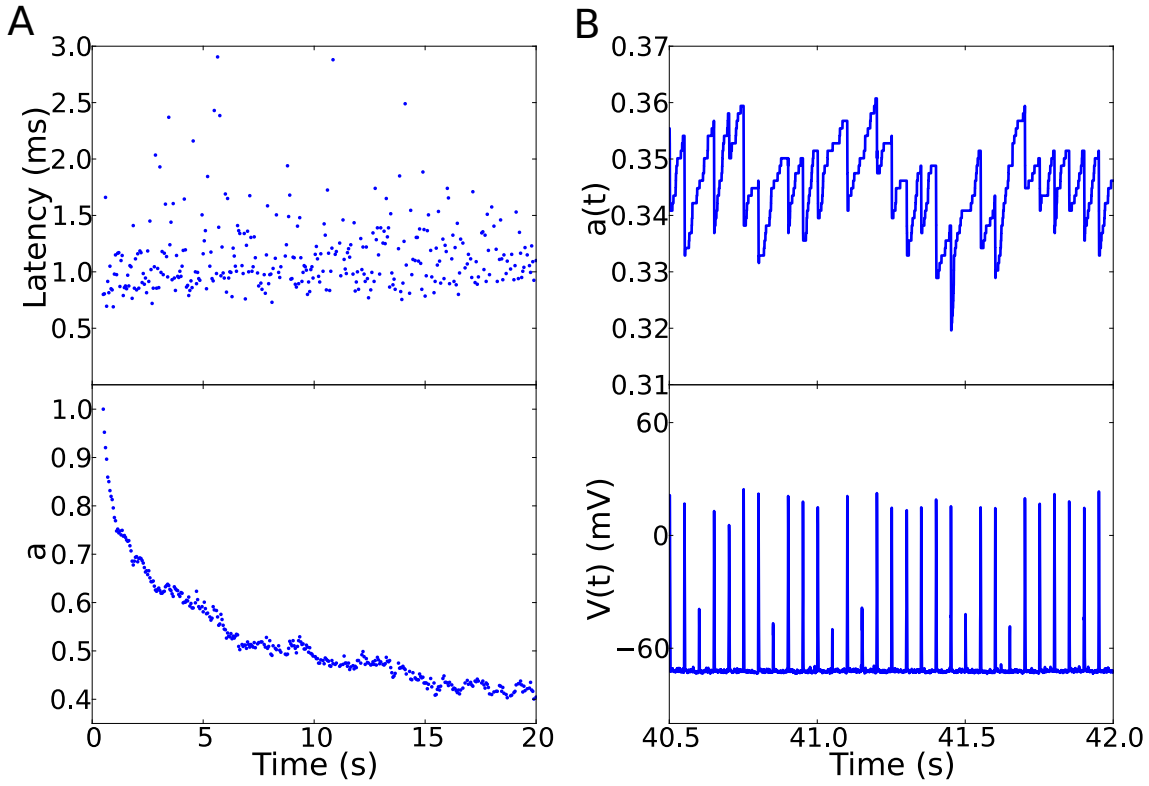

Figure 5.5: (**A**) Evolution of the latency and a during the transient phase and start of the intermittent phase. (**B**) Evolution of a and the membrane potential during the intermittent phase. Simulation performed with $N_c = 1507$

As shown in figure 5.5A, the approach to intermittency in the stochastic model is quite chaotic. It is difficult to define a clear transient phase from the latencies and it is also difficult to define a clear point where the intermittent phase starts, as failures can happen at many values of a. These two properties where not at all present in the experiments and lead us to consider the results from the stochastic models with great caution. As mentioned above and confirmed in figure 5.5B, there is still a clear separation between spikes and failures.

For all three hypotheses, we conducted simulations of 10 h for chain-lengths $N = 1, 5, 10, 50$ and 100, where the inactivation rate $\alpha(V)$ was kept the same and $\beta = 0.0001$, 0.001, 0.001, 0.01 and $0.01\,\mathrm{ms}^{-1}$ respectively. To check the dependence of the effect on the number of sodium channels, we conducted simulations for channel numbers $N_c = 377, 754, 1507, 3016$ and 6786 (note that the channels numbers of the A- and potassium currents where also scaled accordingly). The simulation rate was always kept at 25Hz. If

we allowed the number of channels to vary, we fixed $N_{\min} = 0.9N_{\text{eq}}$ and $N_{\max} = 1.1N_{\text{eq}}$ unless stated otherwise, where N_{eq} is determined from the maximal conductance and the cell's surface S by $N_{\text{eq}} = \overline{g}S/\gamma$, with γ denoting the single channel conductance. When we modelled the removal and insertion of channels, we took their respective rates proportional to the cell's surface $\mu_r = \mu_a = cS$, with $c = 3.183 \cdot 10^{-3}\text{ms}^{-1}\mu\text{m}^{-1}$.

5.3.2 Traditional channel noise

In the model with traditional channel noise, the effect of the long correlations is quite tiny. Figure 5.6A shows a plot of a binary array, where white pixels mean that a spike was elicited in the inter-stimulation interval and black pixels mean that no spike was elicited. The array was cut in slices of 760s that were put on top of each other. At first sight, there are no long term spike-rate changes and the array looks like what one would expect for a purely random statistic. Figures 5.6B and 5.6C show respectively the fluctuations around the mean for different bin lengths and the spike rate, binned in intervals of 10 minutes. These measures confirm that the long term correlation are tiny.

Nevertheless a close examination of the statistical measures reveals that some long correlations are indeed present. Figure 5.7 shows the periodogram spectral density, the detrended fluctuations, the Fano and Allen factors and the sequences of spikes and failures. It is to be seen that these measures follow mostly what one would expect from a random spike rate. The Fano and Allen factors are mostly flat, the detrended fluctuations rise with a coefficient of 1/2 and the sequences of consecutive spikes and of consecutive failures both have an exponential distribution. Nevertheless between bin lengths of $10^2 \sim 10^3$ seconds long correlations can be observed for a chain length of $N = 100$. The Fano and Allen factors show a rising trend (albeit only one order of magnitude) and in this range the detrended fluctuations rise with a coefficient greater than 1/2 (this is clearly visible in figure 5.7H, where for $N < 100$ the coefficient is 1/2 over the whole range of bin sizes). Note that the discrepancies in figures 5.7K and 5.7L are due to the different spike-rates. The larger lengths of sequences of spikes for $N = 1, 5, 50$ mean that the equilibrium spike rate was higher than for $N = 10, 100$. For the sequences of failures it is the other way around.

Thus we can conclude that it is not possible to model the full scale-invariant behaviour with only a chain of inactive states. While such a chain indeed induces long spike rate correlations, these are nevertheless quite tiny and are concentrated in a specific time range ($10^2 \sim 10^3$s). While we could try to include models of the sodium and A-currents that are of arbitrary complexity, it is quite hard to reverse engineer a kinetic scheme that exhibits

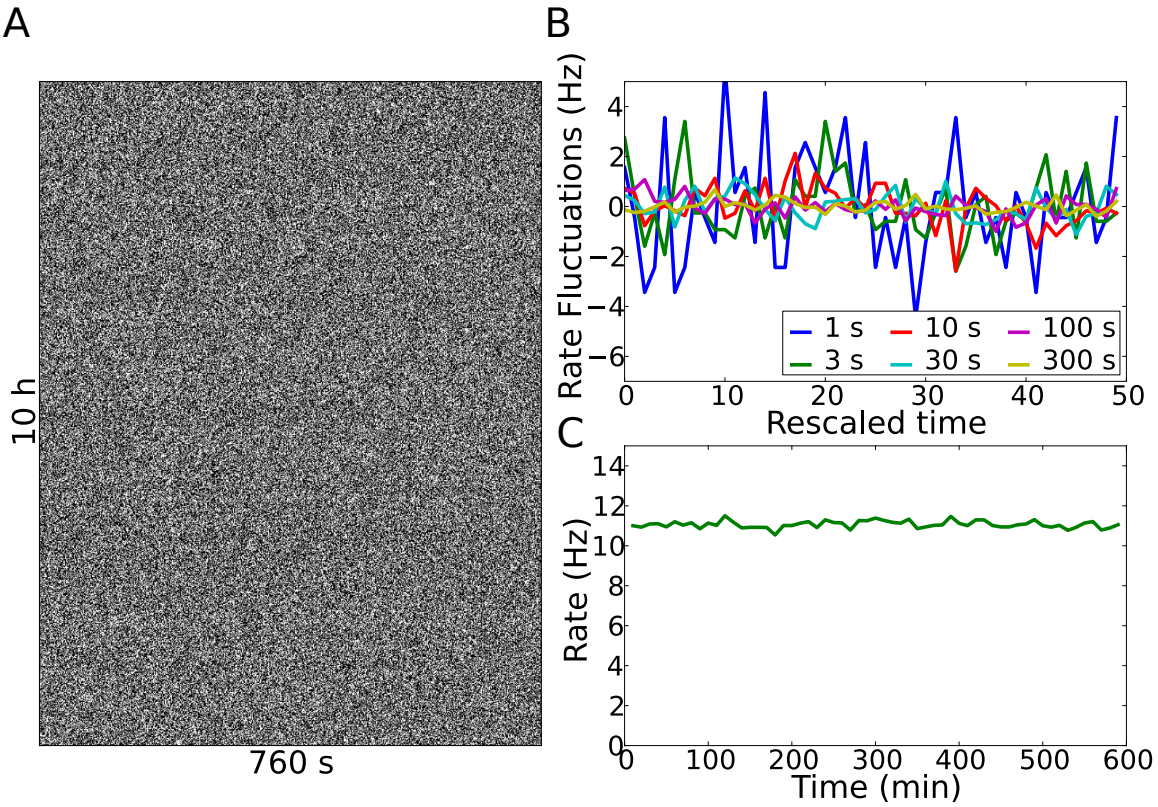

Figure 5.6: Results for a simulation of 10 h, with only traditional channel noise at a simulation rate of 25 Hz. Other paremeters: chain length $N = 100$, $\beta = 0.01\,\mathrm{ms}^{-10}$ and $N_c = 1507$. (**A**) Binary array of the spiking, cut in slices of 760s. White pixels denote spikes, black pixels failures. (**B**) Rate fluctuation around the mean. (**C**) Spike-rate binned in bins of 10 minutes.

scaling behaviour. Moreover, as already noted, we always arrived at the conclusion that the induced correlations were to small, even with low channel numbers. It can be seen from figure 5.5A that at the same time the latency of the spikes was much more chaotic than what is observed experimentally, making this hypothesis even more unlikely.

5.3.3 Removal and insertion without channel noise

Considering the second hypothesis, we see that long range spike rate correlations can exist. Figure 5.8A shows again a binary array of white and black pixels as before. Now it can be seen that there are indeed very large regions of overall reduced excitability followed by very large regions of increased excitability. Moreover, the rate-fluctuations around the

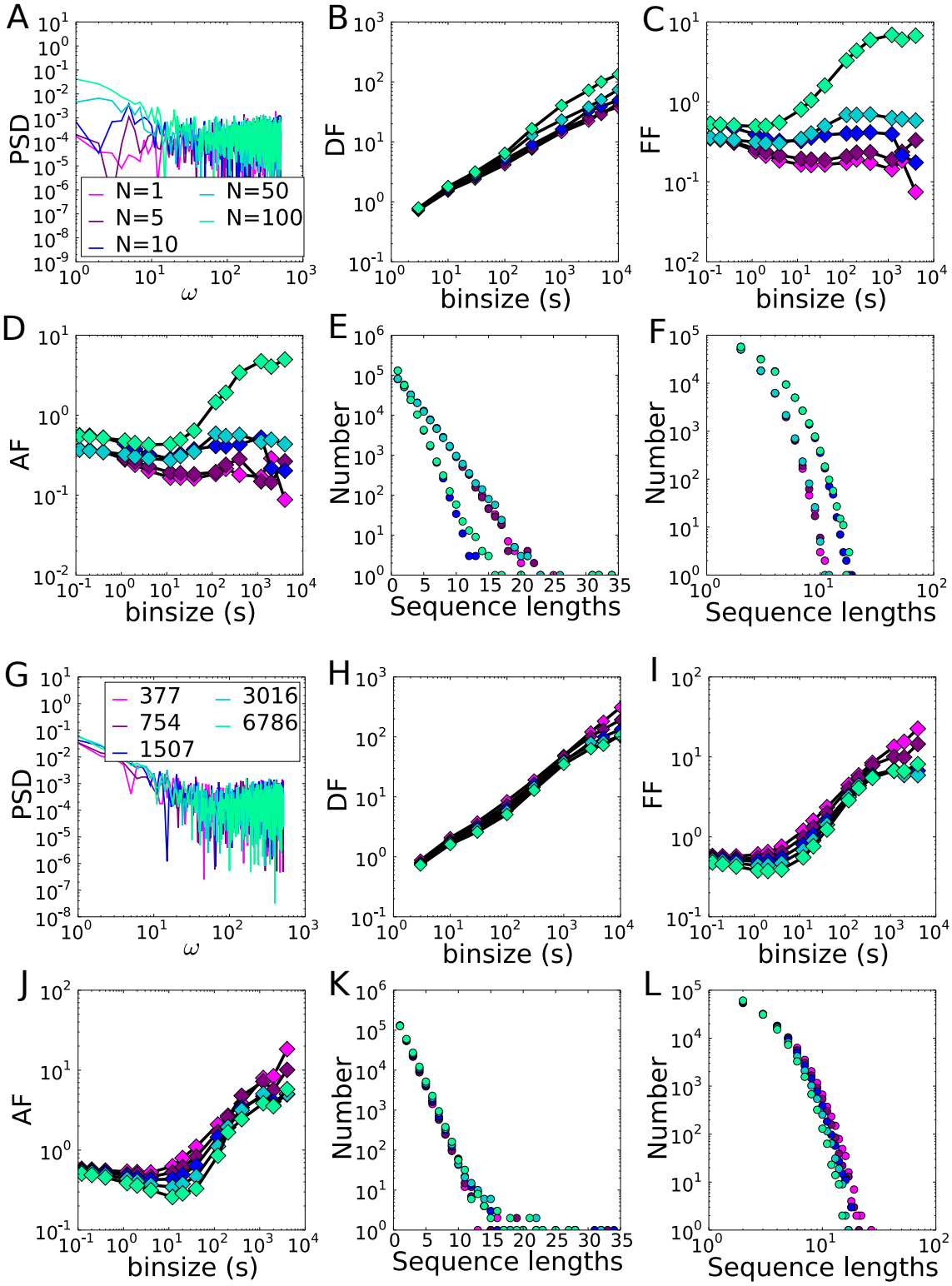

Figure 5.7: (**A**,**G**) Periodogram Spectral Density, (**B**,**H**) Detrended fluctuation analysis, (**C**,**I**), Fano Factor (**D**,**J**), Allen Factor (**E**,**K**), sequences of consecutive spikes and (**F**,**L**) sequences of consecutive failures for simulations times of 10h at frequency 25Hz for different channel numbers (**A**-**F**) and for different chain lengths N (**G**-**L**), with only traditional channel noise.

mean look similar over a wide range of time-scales (figure 5.8B). The spike-rate binned in intervals of 10 minutes does vary (figure 5.8C), but its fluctuations are not as big as the ones measured experimentally .

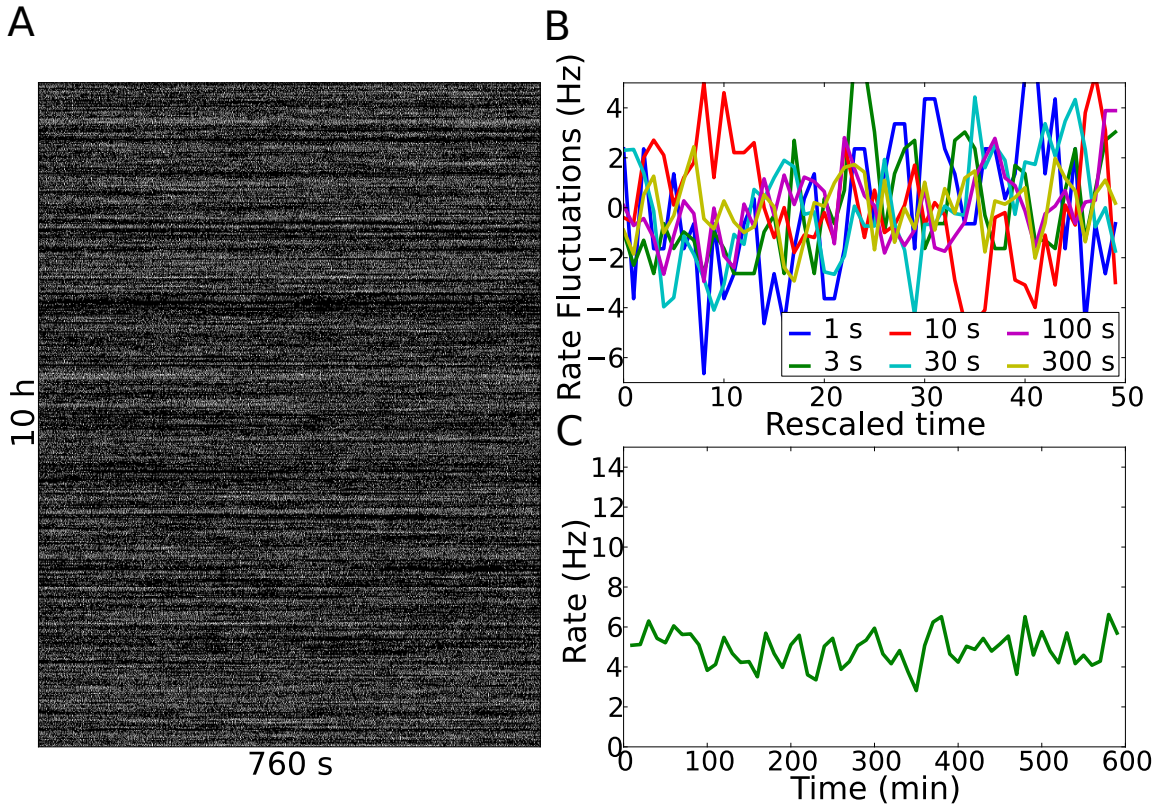

Figure 5.8: Results for a simulation of 10 h, with only the insertion and removal of channels. Stimulation delivered at a rate of 25 Hz. Other parameters: chain length $N = 100$, $\beta = 0.01\,\mathrm{ms}^{-1}$ and $N_c = 1507$. (**A**) Binary array of the spiking, cut in slices of 760s. White pixels denote spikes, black pixels failures. (**B**) Rate fluctuation around the mean. (**C**) Spike-rate binned in bins of 10 minutes.

Looking at the statistical measures (figure 5.9), it is to be seen that there is indeed scaling in the time series of the spike-rate. The periodogram spectral density exhibits $1/\omega$ behaviour, the detrended fluctuation rise with a coefficient close to unity and the Allen and Fano factors rise approximately linearly over a range of time-scales. Because of the sub-threshold random walk behaviour, the distribution of lengths of the sequences of consecutive failures indeed exhibits power law behaviour. The distribution of the lengths of sequences of consecutive spikes is however not exhibiting exponential behaviour, a consequence of the fact that the spikes don't happen randomly, but with a probability equal to

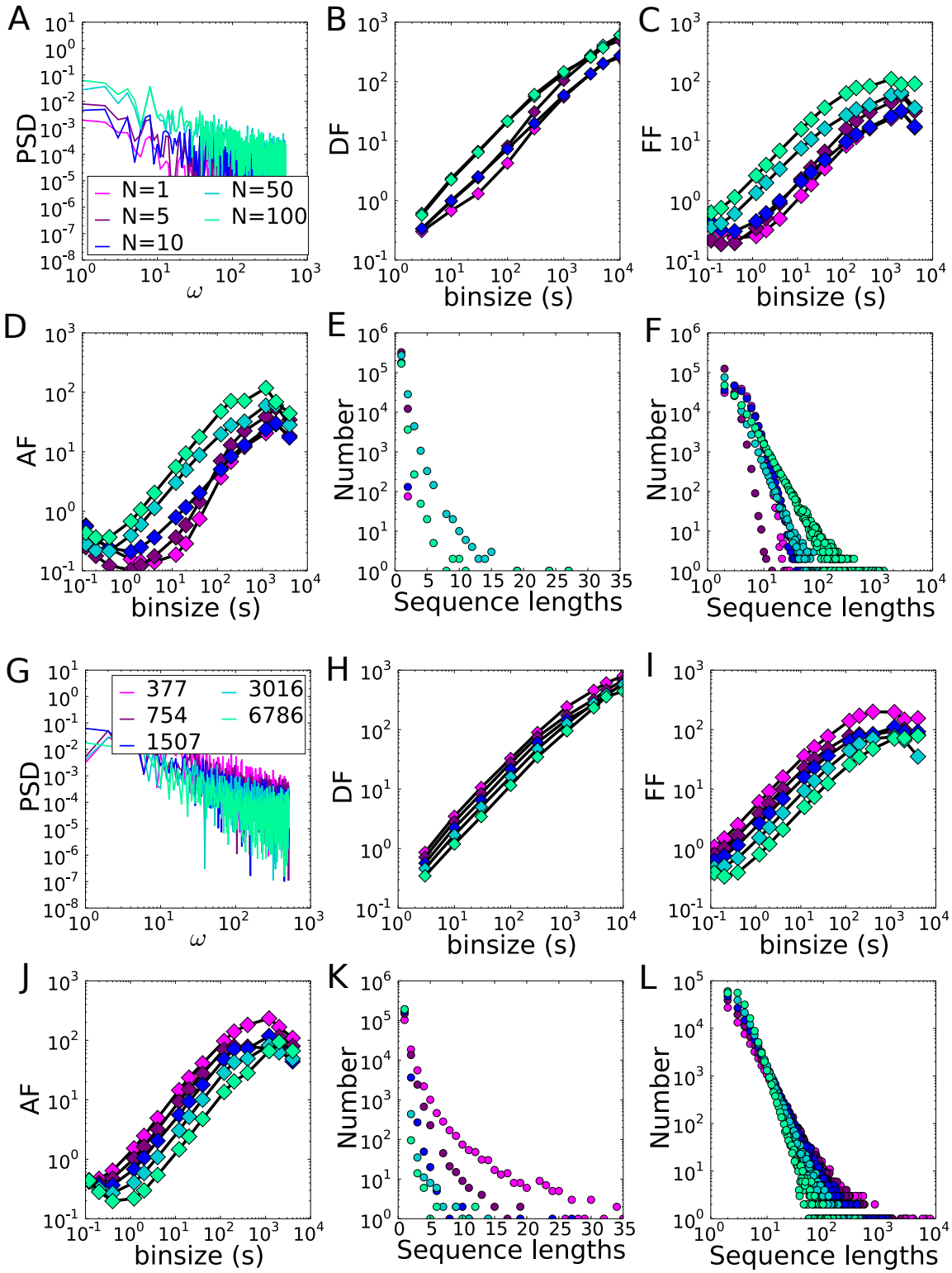

Figure 5.9: (**A**,**G**) Periodogram Spectral Density, (**B**,**H**) Detrended fluctuation analysis, (**C**,**I**), Fano Factor (**D**,**J**), Allen Factor (**E**,**K**), sequences of consecutive spikes and (**F**,**L**) sequences of consecutive failures for simulations times of 10h at frequency 25Hz for different chain lengths N (**A**-**F**) and for different channel numbers N_c (**G**-**L**), with the removal and insertion of channels as the only noise source.

one if a is above a_{thr}. It can furthermore be seen that the scaling becomes much better if the chain length N increases and if the number of channels N_c decreases.

Of course, it can be argued that our choice of $N_{\min} = 0.9N_{\text{eq}}$ and $N_{\max} = 1.1N_{\text{eq}}$ was arbitrary. Therefore we also ran a simulation with $N_{\min} = 0.8N_{\text{eq}}$ and $N_{\max} = 1.0N_{\text{eq}}$. As can be seen in figures 5.10G-5.10L, changing these limits does not have an influence on the overall qualitative behaviour. Only the mean spike rate changes, and accordingly, the distributions of consecutive spikes and failures.

We also compared the two hypothesis of insertion and removal, i.e. proportional to the number of channels in the state or simply in a single state. In figures 5.10A-5.10F we show a comparison between the two cases. As can be seen, these two hypothesis result into scale-invariant excitability over a good range of time scales. Only at the longest time-scales the spike-rate becomes slightly more regular when channels are added to or subtracted from on single state.

5.3.4 Removal and insertion with channel noise

So far we have shown that channel noise alone cannot account for the observed effects, and removing and inserting channels randomly, when the neurons evolves deterministically otherwise, produces a great deal of the experimentally observed behaviour. In real neurons however, both phenomena should be present at the same time. Thus we explore what happens if we include both effects into the model neuron. Figure 5.11A shows the familiar binary array. As can be seen, long correlations are clearly present, albeit less pronounced than in the deterministic case. This is confirmed further by the rate fluctuations (figure 5.11B).

The statistical measures in figure 5.12 show that there is indeed scaling in the time series of the spike-rate. The periodogram spectral density decreases as $1/\omega$, whereas the detrended fluctuation rise with a slope greater than $1/2$. The Fano and Allen factors also rise with the bin size over a few orders of magnitude. Again, the scaling improves as the chain length N increases. The scaling is present for all tested channels numbers N_c. Notice however that the distributions of the lengths of sequences of consecutive spikes and failures are again exponentials. This is because there is no sharp spike-threshold in a, and thus spikes happen at random, with a probability only slightly correlated by a.

Finally we check what happens if we apply the algorithm for inserting and removing channels also to the A-current, the other current relevant at spike-initiation. This can be interesting, because the excitability as a function of $g_{\text{Na}}^{\text{eff}} = \overline{g}_{\text{Na}} a$ and $g_{\text{A}}^{\text{eff}}$ might change only slightly in one direction of the relevant phase-space (for instance in the direction of

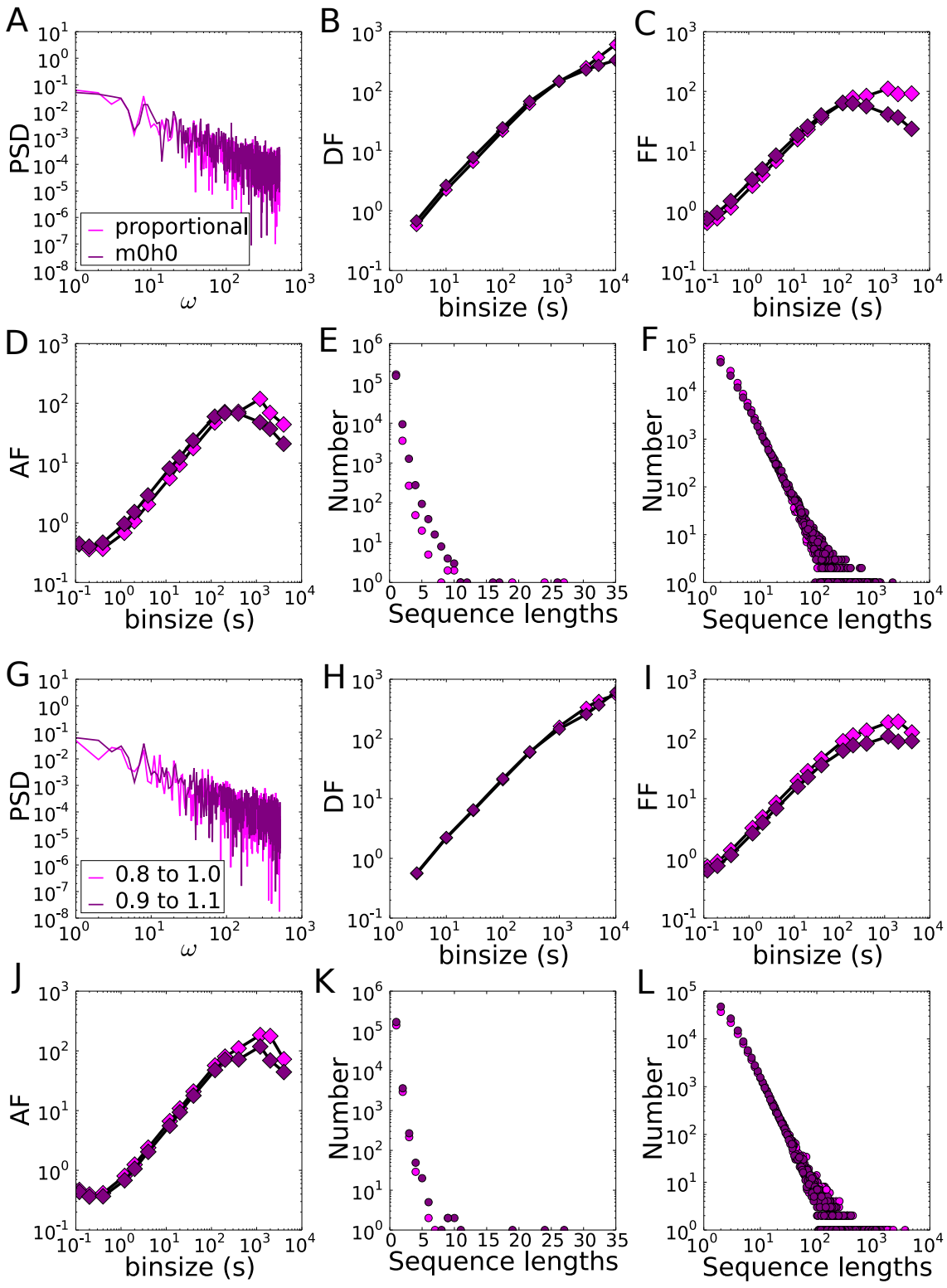

Figure 5.10: (**A**,**G**) Periodogram Spectral Density, (**B**,**H**) Detrended fluctuation analysis, (**C**,**I**), Fano Factor (**D**,**J**), Allen Factor (**E**,**K**), sequences of consecutive spikes and (**F**,**L**) sequences of consecutive failures for simulations times of 10h at frequency 25Hz a chain length $N = 100$ and a channel number $N_c = 1507$, with the insertion and removal of channels as only noise source. Figures (**A**-**F**) compare proportional insertion and removal with insertion in and removal from a single site ($m_0 h_0$) and figures (**G**-**L**) compare different limits $N_{\min}$ and $N_{\max}$.

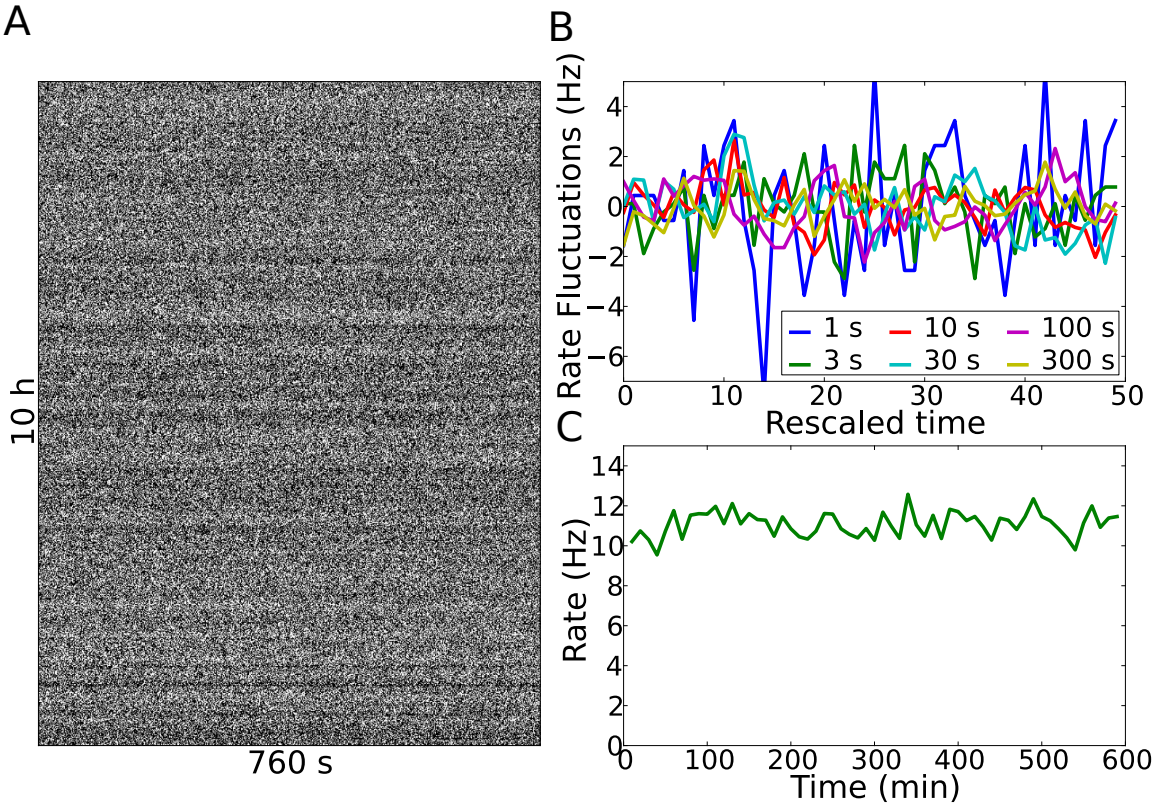

Figure 5.11: Results for a simulation of 10h, with channels noise and the insertion and removal of channels. Stimulation delivered at a rate of 25Hz. Other parameters: chain length $N = 100$, $\beta = 0.01\text{ms}^{-10}$ and $N_c = 1507$. (**A**) Binary array of the spiking, cut in slices of 760s. White pixels denote spikes, black pixels failures. (**B**) Rate fluctuation around the mean. (**C**) Spike-rate binned in of 10 minutes.

$g_{\text{Na}}^{\text{eff}}$), but might drop very sharply in other directions. This is however not the case for the Connor-Stevens model (see figure 5.4) and applying this algorithm on both currents does not lead to a qualitative change in the behaviour (see figure 5.13).

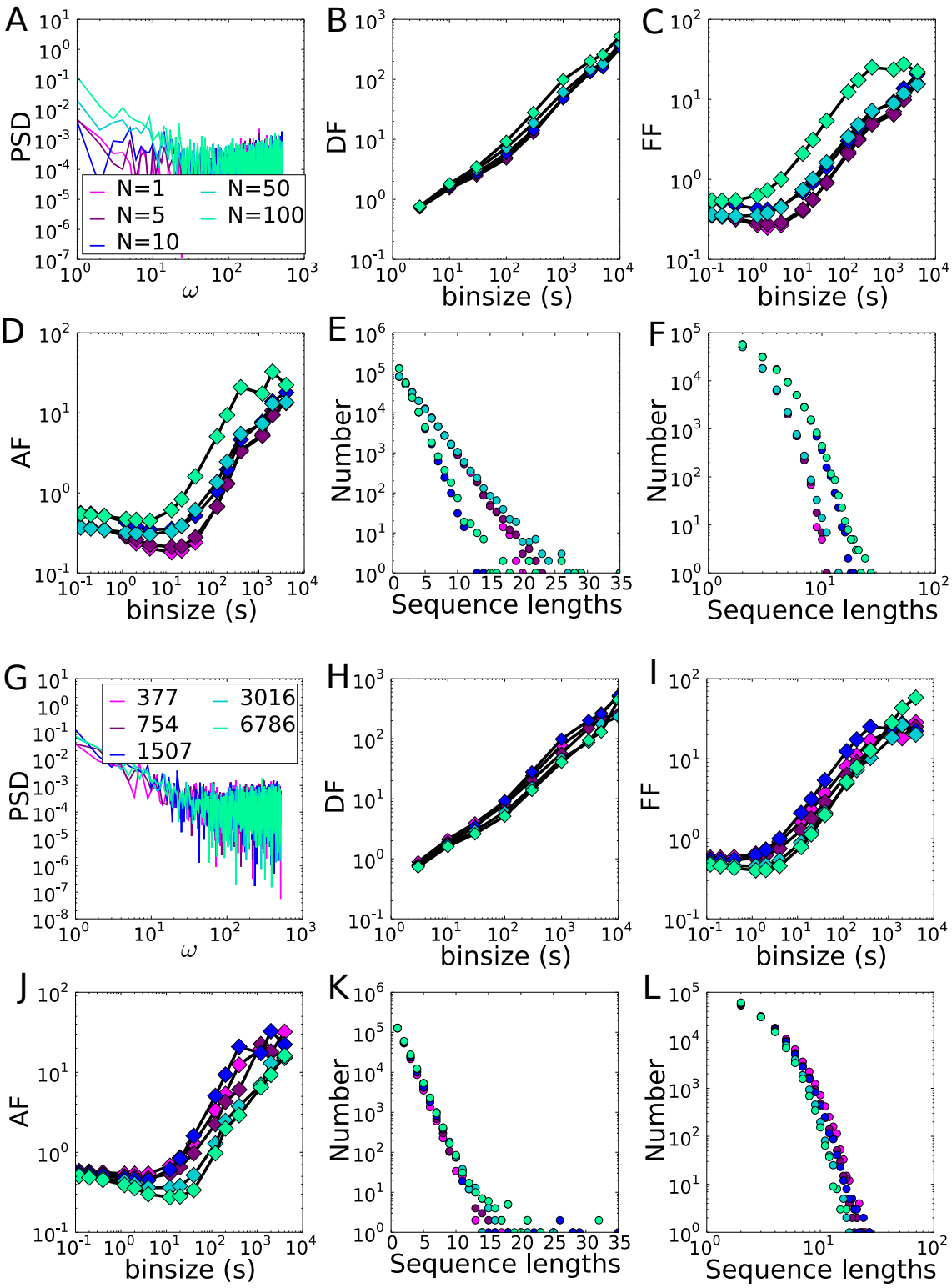

Figure 5.12: (**A**,**G**) Periodogram Spectral Density, (**B**,**H**) Detrended fluctuation analysis, (**C**,**I**), Fano Factor (**D**,**J**), Allen Factor (**E**,**K**), sequences of consecutive spikes and (**F**,**L**) sequences of consecutive failures for simulations times of 10h at frequency 25Hz for different chain lengths N (**A**-**F**) and for different channel numbers (**G**-**L**). Both channel noise and insertion and removal were included.

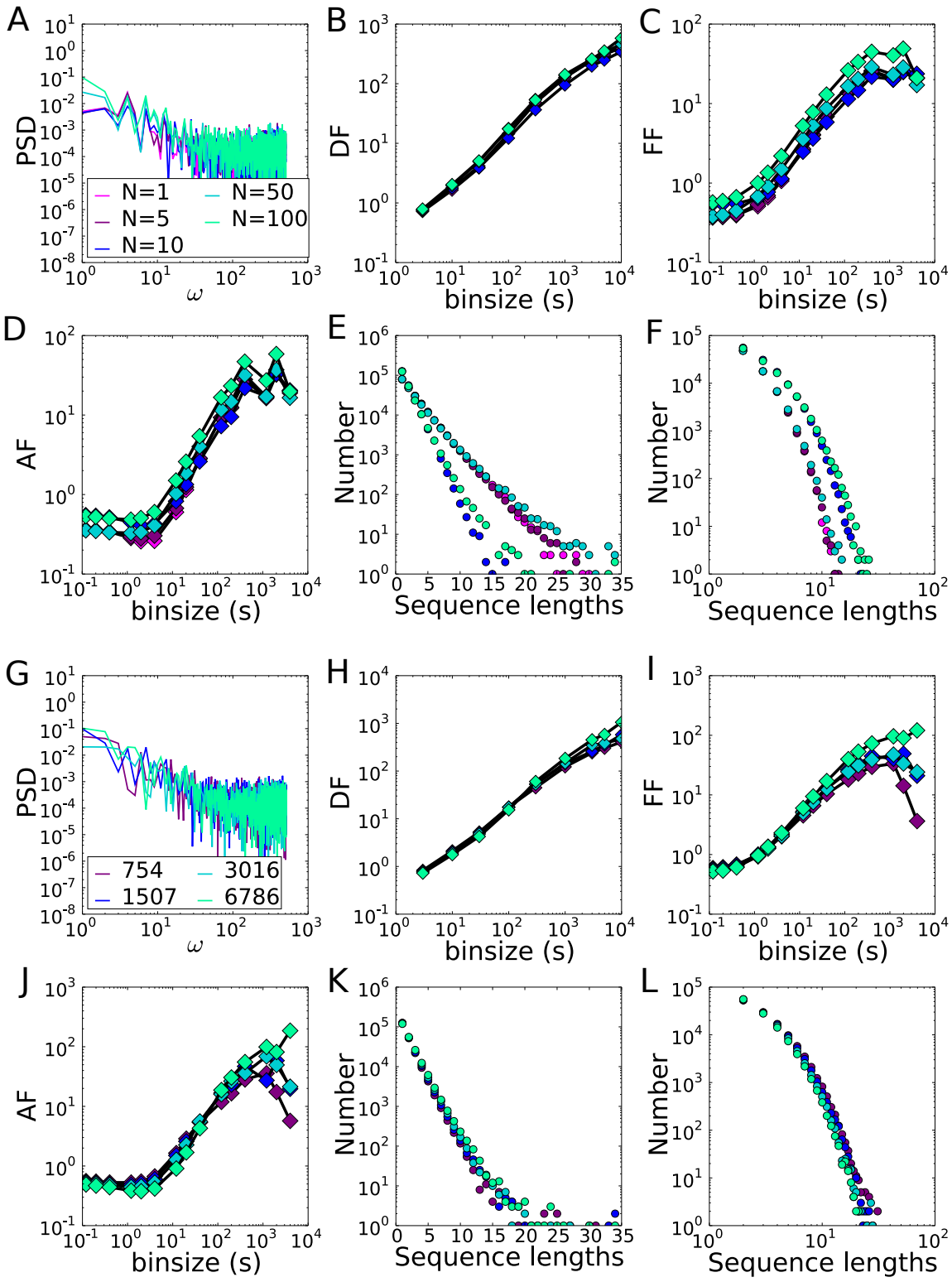

Figure 5.13: (**A**,**G**) Periodogram Spectral Density, (**B**,**H**) Detrended fluctuation analysis, (**C**,**I**), Fano Factor (**D**,**J**), Allen Factor (**E**,**K**), sequences of consecutive spikes and (**F**,**L**) sequences of consecutive failures for simulations times of 10h at frequency 25Hz for different chain lengths N (**A**-**F**) and for different channel numbers (**G**-**L**). Channel noise was included and also the insertion and removal of both the sodium channels and the potassium channels of the A-current.

Chapter 6

Conclusion

In this thesis work we modelled the experimental results in two stages: first, we expanded a deterministic model with a sodium current with slow inactivation. We showed that this model is tunable to fit the experimental data and can be applied with minor changes to fit different types of qualitative behaviour. If the length of the chain N is sufficient ($N \sim 50 - 100$), the reciprocals $1/\tau$ of the durations of the transient phases as a function of the stimulation rate exhibit the observed curved shape. Once N is chosen, the kinetic rate β and the amplitude of the inactivation rate $\alpha(V)$ can be chosen so that the steady-state spike-rates have the right values and that the durations of the transient phases are within the right order of magnitude for each stimulation rate.

Secondly, we have looked at possible ways to create a model that exhibits the observed scale invariance in the spike rate over a good range of time-scales. We have shown that to introduce these scale-invariant features, it is not sufficient to include traditional channel noise in the model neuron. For very few channels, so that fluctuations are large, long correlations are indeed present, but their influence is not big enough to introduce major spike rate changes over long time scales. Moreover, the long correlations are only present in a specific range of time scales (10^2 to 10^3 s). Also, this neuron model behaves much more chaotically than the experimental observations suggest, as failures happen often and randomly, so that it becomes very hard to separate transient from intermittent phases. As a consequence, the distributions of the lengths of the sequences of consecutive spikes and of consecutive failures are both exponential. While for the spikes this agrees with the experiments, this is not the case for the failures.

This led us to introduce a new form of stochasticity with very different statistical properties than those of the Markov noise. We started from very simple principles, that we implemented on a purely phenomenological basis, and hypothesized that this noise could

result from the insertion and removal of ion channels from the cell membrane. Adding this noise, and evolving the voltage and fractions of open channels deterministically otherwise, we found that this model could indeed reproduce the scale-invariant excitability, while introducing no important changes in the overall qualitative behaviour of transient and intermittent phases. Moreover, because of the sub-threshold random-walk behaviour, this model results in a power-law distribution of lengths of sequences of consecutive failures. Nevertheless, the distribution of the lengths of sequences of consecutive spikes does not follow the experimentally observed exponential distribution, because in this model spikes do not occur randomly.

Combining the two approaches, we found again that the distributions of the lengths of the sequences of consecutive spikes and of consecutive failures were both exponential, because spikes again happen randomly. Nevertheless, the long fluctuations present in the spike rate were considerably bigger than with only traditional channel noise, and the scaling lasted for a bigger range of time-scales.

We also note that we have only used the Connor-Stevens model as a basis for this work. Nevertheless there are multiple ways to introduce the same behaviour, as was shown during the course of this work in [16]. It might be interesting to look at other models, since as we discussed, spikes that happen randomly lead to exponential distributions of sequence lengths and sub-threshold random walks lead to power law distributions of lengths of sequences of failures. Thus a model with a multidimensional phase space of effective conductances relevant for spike-generation that has a very sharp firing threshold in one direction and where the excitability changes only slightly in other directions, could be used in principle to obtain both distributions at the same time.

We believe that, on its own, this research provides a basis to explore the effect that these long-lasting excitability changes have on the behaviour of more complex neuronal systems, since we provided a model that, even if it does not represent the true physical picture, at least reproduces the experimentally observed results and can therefore be used to explore the consequences of this effect in neural networks. For this purpose alone our model is already very interesting, as the general hypothesis in neuroscience is that memory in neural networks is only coded in the strength of synaptic connections. The work of [6] showed that neurons may in fact also have memory: the probability that a neuron may spike at a given moment can be correlated with the probability it spiked minutes, or even hours before. Thus it would be highly relevant to investigate whether networks composed of scale-invariant neuron models lead to fundamental differences in the way information is processed.

We also think that this work may spark further experimental research, as it poses a

fundamental question about how the overall excitability of neurons is regulated by changes in the number of ion channels in the cell membrane. To date, very little is known about processes that govern these changes, and many parameters, such as gene expression and environmental changes might play a role. A big obstacle for this work was the sparsity of available information on this subject, which led us to implement a model that was as simple as possible. If more information will become available at some point in the future, more detailed models could be constructed that exhibit scale-invariant excitability, and more refined questions could be posed about its causes.

Appendix A

System-size expansion

In this paragraph we compute the diffusion matrix for a linear diffusive chain that consists of $K+2$ states $(X_{-1}, X_0, \ldots, X_K)$, wherein there is a large number N of random walkers. Remember that X_i denotes the amount of random walkers in state i. The fraction of random walkers in that state will be denoted by $x_i = X_i/N$. Since $X_{-1} = N - \sum_{n=0}^{K} X_n$, we only need to consider the evolution of $\mathbf{X} = (X_0, \ldots, X_k)$. With no extra effort, we can assume general transition rates between the states. Let us denote the rate to go from state p to state q by $w(q,p)$. According to the general theory of system size expansions [23], we need to rewrite the transition probability $W(\mathbf{X}|\mathbf{X}')$ from the master equation (5.1) in a form $W(\mathbf{X}', \mathbf{r})$, with $\mathbf{r} = \mathbf{X} - \mathbf{X}'$. The diffusion matrix will then be given by equation (5.12), where $\mathbf{x} = \mathbf{X}/N$ and $\Omega(\mathbf{x}, \mathbf{r}) = W(\mathbf{X}, \mathbf{r})$.
To find this transition probability $W(\mathbf{X}|\mathbf{X}')$, we assume that, in the limit of a small time step, at most one walker can change its position. Hence we have that either $X_n = X'_n$ for all n or that $(X_{n-1}, X_n) = (X'_{n-1} \pm 1, X'_n \mp 1)$ for one specific n. The probability for a transition from $n-1$ to n in a small time interval $[t, t+\mathrm{d}t]$ can be written as $w(n, n-1)X_n \mathrm{d}t$ and the probability for the opposite transition as $w(n-1, n)X_{n-1}\mathrm{d}t$. With this knowledge, the master equation becomes

$$\begin{aligned}\dot{P}(\mathbf{X}, t) = \sum_{n=0}^{K} \{ & w(n, n-1)\,(X_{n-1}+1)\,P(X_{n-1}+1, X_n-1, t) \\ & + w(n-1, n)\,(X_n+1)\,P(X_{n-1}-1, X_n, t) \\ & - [w(n-1, n)\,X_n + w(n, n-1)\,X_{n-1}]P(\mathbf{X}, t)\}. \end{aligned} \tag{A.1}$$

This can be written in the canonical form (5.1) by introducing Dirac-delta's

$$\begin{aligned}\dot{P}(\mathbf{X},t) = &\int \mathrm{d}\mathbf{X}'\,[P(\mathbf{X}',t)\\ &\cdot\sum_{n=0}^{K}\{w(n,n-1)X'_{n-1}\delta(X'_n-[X_n-1])\delta(X'_{n-1}-[X_{n-1}+1])\prod_{k\neq n,n-1}\delta(X'_k-X_k)\\ &+w(n-1,n)X'_n\delta(X'_n-[X_n+1])\delta(X'_{n-1}-[X_{n-1}-1])\prod_{k\neq n,n-1}\delta(X'_k-X_k)\}\\ &-P(\mathbf{X},t)\{\text{conjugate part}\}.\end{aligned}$$

vankampen

Hence $W(\mathbf{X}|\mathbf{X}')$ is recognized as

$$\begin{aligned}&\sum_{n=0}^{K}\{w(n,n-1)X'_{n-1}\delta(X'_n-[X_n-1])\delta(X'_{n-1}-[X_{n-1}+1])\prod_{k\neq n,n-1}\delta(X'_k-X_k)\\ &+w(n-1,n)X'_n\delta(X'_n-[X_n+1])\delta(X'_{n-1}-[X_{n-1}-1])\prod_{k\neq n,n-1}\delta(X'_k-X_k)\}.\end{aligned}$$

From the definitions $\mathbf{x}=\mathbf{X}/N$ and $\Omega(\mathbf{x},\mathbf{r})=W(\mathbf{X},\mathbf{r})$ it follows that

$$\begin{aligned}\Omega(\mathbf{x},\mathbf{r}) =&N\sum_{n=0}^{K}\{w(n,n-1)x_{n-1}\delta(r_n-1)\delta(r_{n-1}+1)\prod_{k\neq n,n-1}\delta(r_k)\\ &+w(n-1,n)x_n\delta(r_n+1)\delta(r_{n-1}-1)\prod_{k\neq n,n-1}\delta(r_k)\}\end{aligned}\quad .$$

Upon substitution in (5.12), the elements of the diffusion matrix are found:

$$(\mathbb{D}(\mathbf{x}))_{00}=\frac{1}{N}[w(0,-1)x_{-1}+w(-1,0)x_0+w(1,0)x_0+w(0,1)x_1] \tag{A.2}$$

$$(\mathbb{D}(\mathbf{x}))_{KK}=\frac{1}{N}[w(K,K-1)x_{K-1}+w(K-1,K)x_K] \tag{A.3}$$

$$(\mathbb{D}(\mathbf{x}))_{ll}=\frac{1}{N}[w(l,l-1)x_{l-1}+w(l-1,l)x_l+w(l+1,l)x_l+w(l,l+1)x_{l+1}] \tag{A.4}$$

$$(\mathbb{D}(\mathbf{x}))_{kl}=-\frac{1}{N}[w(k,l)x_l+w(l,k)x_k]\ \text{for}\ |k-l|=1 \tag{A.5}$$

and zero otherwise.

Bibliography

[1] L. F. Abbott. Theoretical neuroscience rising. *Neuron*, 60(3):489–95, November 2008.

[2] Lav R. Varshney, Beth L. Chen, Eric Paniagua, David H. Hall, and Dmitri B. Chklovskii. Structural properties of the *Caenorhabditis elegans* neuronal network. *PLoS Comput Biol*, 7(2):e1001066, 02 2011.

[3] Peter Dayan and L. F. Abbott. *Theoretical Neuroscience: Computational and Mathematical Modeling of Neural Systems*. The MIT Press, 2005.

[4] Nicolas Brunel and Mark C. W. Van Rossum. Lapicque's 1907 paper: from frogs to integrate-and-fire. *Biological Cybernetics*, 97(5-6):337–339, 2007.

[5] A. L. Hodgkin and A. F. Huxley. A quantitative description of membrane current and its application to conduction and excitation in nerve. *Journal of Physiology*, pages 500–544, 1990.

[6] A. Gal, D. Eytan, A. Wallach, M. Sandler, J. Schiller, and S. Marom. Dynamics of excitability over extended timescales in cultured cortical neurons. *J Neurosci*, 30(48):16332–42, 2010.

[7] C. C. Chow and J. A. White. Spontaneous action potentials due to channel fluctuations. *Biophysical journal*, 71(6):3013–21, December 1996.

[8] J. A. Connor and C. F. Stevens. Prediction of Repetitive Firing Behaviour from Voltage Clamp Data on an Isolated Neurone Soma. *Journal of Physiology*, pages 31–53, 1971.

[9] C. A. Vandenberg and F. Bezanilla. A sodium channel gating model based on single channel, macroscopic ionic, and gating currents in the squid giant axon. *Biophysical journal*, 60(6):1511–33, December 1991.

[10] I. M. Raman and B. P. Bean. Inactivation and recovery of sodium currents in cerebellar Purkinje neurons: evidence for two mechanisms. *Biophysical journal*, 80(2):729–37, February 2001.

[11] Bard Ermentrout. Type I membranes, phase resetting curves, and synchrony. *Neural computation*, 1996.

[12] C.-K. Peng, S. Havlin, H. E. Stanley, and A. L. Goldberger. Quantification of scaling exponents and crossover phenomena in nostationary hearbeat time series. *Chaos*, 1994.

[13] Steven B. Lowen and Malvin C. Teich. The periodogram and allan variance reveal fractal exponents greater than unity in auditory-nerve spike trains. 1996.

[14] Amir Toib, Vladimir Lyakhov, and Shimon Marom. Interaction between duration of activity and time course of recovery from slow inactivation in mammalian brain Na^+-channels. *The Journal of Neuroscience*, 18(5):1893–1903, 1998.

[15] Maura Arsiero, Hans-Rudolf Luscher, Brian Nils Lundstrom, and Michele Giugliano. The impact of input fluctuations on the frequency-current relationships of layer 5 pyramidal neurons in the rat medial prefrontal cortex. *The Journal of Neuroscience*, 27(12):3274–3284, 2007.

[16] Daniel Soudry and Ron Meir. Conductance-based neuron models and the slow dynamics of excitability. *Frontiers in Computational Neuroscience*, 6(00004), 2012.

[17] Gail Gilboa, Ronen Chen, and Naama Brenner. History-dependent multiple-time-scale dynamics in a single-neuron model. *The Journal of Neuroscience*, 25(28):6479–6489, 2005.

[18] Daniel T Gillespie. Exact Stochastic Simulation of Coupled Chemical Reactions. *The Journal of Physical Chemistry*, 81(25), 1977.

[19] R.F. Fox and Y. Lu. Emergent collective behavior in large numbers of globally coupled independently stochastic ion channels. *Physical review. E, Statistical physics, plasmas, fluids, and related interdisciplinary topics*, 49(4):3421–3431, April 1994.

[20] Joshua Goldwyn, Nikita Imennov, Michael Famulare, and Eric Shea-Brown. Stochastic differential equation models for ion channel noise in Hodgkin-Huxley neurons. *Physical Review E*, 83(4):1–16, April 2011.

[21] J.H. Goldwyn and E. Shea-Brown. The what and where of adding channel noise to the Hodgkin-Huxley equations. *Arxiv preprint arXiv:1104.4823*, pages 1–14, 2011.

[22] Daniele Linaro, Marco Storace, and Michele Giugliano. Accurate and fast simulation of channel noise in conductance-based model neurons by diffusion approximation. *PLoS computational biology*, 7(3):e1001102, March 2011.

[23] NG Van Kampen. *Stochastic processes in physics and chemistry*. North Holland, 2007.

[24] Jos Thijssen. *Computational Physics*. Cambridge University Press, 2 edition, 2007.

[25] F Conti and E Wanke. Channel noise in nerve membranes and lipid bilayers. *Quarterly reviews of biophysics*, 8(4):451–506, November 1975.

[26] Bruce J West. *Fractal physiology and the fractional calculus: a perspective.*, volume 1. January 1994.